First principles study of $Ga_{(20-x)}Al_x^+$ nanoalloys: structure, thermodynamics and phase diagram

by

Udbhav Ojha

A thesis submitted to
the Victoria University of Wellington
in fulfilment of the requirements
for the degree of
Doctor of Philosophy
in Physics

Victoria University of Wellington

October 2015

Abstract

Nanoalloys (a finite framework of two or more metal atoms) represent a rapidly growing field owing to the possibilities of tuning its properties as desired for various applications. Their properties are size, shape, composition, chemical ordering, and temperature dependent, thereby offering a large playground for varied research motivations. This thesis documents the investigations on how the addition of aluminium affects the cationic gallium clusters, both in terms of geometric & electronic structure and thermodynamics, which have been observed to show *greater-than-bulk melting* behaviour for small sizes. A specific cluster size of 20 atoms is selected, $Ga_{(20-x)}Al_x^+$, with the overall intention of creating a phase diagram which is the most reliable way to predict the phase changes in the system. All the first principles (density functional theory) based Born-Oppenheimer molecular dynamics calculations have been performed in the microcanonical ensemble. Melting behaviour is first studied in the pure Al_{20}^+ clusters and then in three representative clusters of $Ga_{(20-x)}Al_x^+$ series: $Ga_{19}Al^+$, $Ga_{11}Al_9^+$ and $Ga_3Al_{17}^+$ clusters. We observe that all the three nanoalloy compositions show *greater-than-bulk melting* behaviour behaviour as well and in $Ga_{19}Al^+$, specifically, Al prefers the *internal* sites, contrary to the previous arguments. We go on to complete the *solid-liquid-like* melting phase diagram using the calculated information and further propose a model of these *greater-than-bulk melting* clusters to be components of the corresponding bulk phases, whether metals or alloys, with additional size-dependent contributions added to it.

Parts from this thesis have also been published as journal articles mentioned below:

1. U. Ojha, K. G. Steenbergen and N. Gaston, How a single aluminum atom makes a difference to gallium: First-principles simulations of bimetallic cluster melting, *J. Chem. Phys.*, 2013, **139**, 094309.

2. U. Ojha, K. G. Steenbergen and N. Gaston, Al_{20}^{+} does melt, albeit above the bulk melting temperature of aluminium, *Phys. Chem. Chem. Phys.*, 2015, **17**, 3741-3748.

3. U. Ojha and N. Gaston, Characterizing the greater-than-bulk melting behaviour of Ga-Al nanoalloys, *Accepted* for publication by *The Journal of Physical Chemistry C*, arXiv:1503.03629v2

Acknowledgements

Looking back, it has been three years since I landed in Wellington and met you for the first time - Dr. Nicola Gaston. Thank you so much for being such a wonderful supervisor. Your kindness, patience and ever so cheerful attitude has helped me a lot in this journey.

To my mum and dad back home, this PhD wouldn't have been possible without your constant support. Thank you so much for believing in me and I just hope I can be as good as you both are.

To Shaun, Matthias, Krista and my sys admins Kevin and Ben - thank you so much for your patience and helping me get the work done. I have learnt a lot from you all.

To Graeme, Rosemary, Vivek and my cricket teammates, Wong, Dani, Stephanie, Julia, Luis, Anne, Saurabh, Mousumi and Kia Maia friends and office colleagues - thank you so much for all the beautiful moments I had with you all during this time. Its your presence that made me enjoy my PhD all the more.

To Disha, words can't describe how much I owe you! It has been a wonderful journey walking alongside you and hope to keep walking. Having you in my life is one of the best gifts I have and thank you so much for everything.

Finally to the two people who have been the pillars I look up to. To my sister, Anamika, your guidance, love and support has helped a lot in shaping me as an individual. Thank you so much for being such a lovely sis and kicking sense into me from time to time. And, to my *late grandfather*, baba I know you would be having a masala tea with God right now and looking at my PhD results. Thank you so much for all the wonderful memories I shared with you.

Contents

Chapter 1

Introduction

> "There's plenty of room at the bottom."
>
> Richard P. Feynman

Arguably, 'Nanotechnology' was born with this statement of Richard Feynman[1]. Not only did he conceive what the field had to offer, he had also envisioned the technological applications which could arise from harnessing the abilities of atoms. A nice example would be to write the entire 24 volumes of Britannica on the head of a pin.

On the scale of numbers of atoms, our day-to-day encounter with materials generally calls for a 'macroscopic' description. If seen as the two extremes, the lowermost being a single atom, and the bulk limit being, perhaps, Avogadro's number (6.022×10^{23}), all the sizes in between are 'clusters' mainly because they are finite entities. However, clusters are generally considered to typically comprise $\sim$10 to 10^6 atoms[2, 3, 4]. The small sizes of clusters have a significant effect on their geometric and electronic structure, binding energy and thermodynamics leading to novel physical and chemical properties which are completely different from their corresponding bulk phases[5]. For example, gold nanoparticles can exhibit either red, purple or orange instead of their signature golden yellow colour with changes in its size[6, 7]. Understanding the complex interplay between the changes in the underlying electronic structure of a cluster, being fundamental to all the observed properties, and size is essential for their fabrication and functional optimisation.

Combining two or more metal atoms together in the size regime of clusters, to form nanoalloys, can further change the physical and chemical properties which are not only different from that exhibited by their corresponding bulk alloy phases but also from their pure monometallic cluster counterparts having the same size[8]. The

properties of nanoalloys depends, in addition to the size, structure, composition and temperature, on the chemical ordering of the participating atoms within the cluster, thus offering ample room for fine tuning as desired in applications such as catalysis, electronics and optics[8, 9, 10, 11, 12]. This encourages a need for further development of our understanding of how the emergent properties of nanoalloys are influenced by different variables (size, structure (both, geometric and electronic), temperature and time).

The scientific research documented in this thesis focuses on the computational modelling of the 20-atom gallium-aluminium nanoalloy ($Ga_{(20-x)}Al_x^+$) and the creation of a *solid-liquid-like melting* phase diagram for this system. Chapter 2 describes briefly the underlying theory behind the simulation, the data analysis algorithms used and the details of our simulation. In chapter 3, electron localisation function (ELF) study on small gallium clusters is done to show that they are inconclusive in predicting the bonding in these systems. Chapter 4 first recaps the results previously obtained for Ga_{20}^+ cluster[13], which have been found to show the *greater-than-bulk melting* behaviour and then describes the results obtained for Al_{20}^+ cluster which show a similar melting behaviour, thus making the 20-atom Ga-Al system a *greater-than-bulk melting* nanoalloy. Selecting three representative clusters in the $Ga_{(20-x)}Al_x^+$ cluster series, $Ga_{19}Al^+$, $Ga_{11}Al_9^+$ and $Ga_3Al_{17}^+$ respectively, the effect of increasing Al content on the structure and thermodynamics exhibited by the cluster is analysed in Chapter 5. A solid-liquid-like melting phase diagram for 20 atom gallium aluminium nanoalloy system is created in Chapter 6 before concluding in Chapter 7.

1.1 Atomic clusters

> "But I must confess I am jealous of the term atom; for though it is very easy to talk of atoms, it is very difficult to form a clear idea of their nature, especially when compounded bodies are under consideration."
>
> Michael Faraday
> Experimental researches in electrochemistry (1839-1855), Vol.1, 195

Faraday's words clearly describe the problems one faces when compounded bodies of atoms (in our case 'clusters') are in question. Even the addition of one atom can significantly change the behaviour of clusters[14]. Atomic clusters, being exper-

imentally realisable finite frameworks of atoms, are stable aggregates and different from molecules in the sense that size selected clusters are artificialy synthesised[15]. Modern techniques such as sputtering, chemical vapour deposition (CVD), laser induced vaporisation, supersonic molecular beam and many others have helped in the preparation of clusters, having sizes ranging from a few angstroms to nanometers, either in the gas-phase as "free-clusters", passivated by surfactant molecules acting as ligands or supported on a silica/MgO/TiO_2 substrate. They can assume a variety of shapes and can exhibit completely different properties in comparison to their bulk counterparts. Moreover, properties such as stability, HOMO-LUMO gap, magnetism and optical spectrum can be size sensitive as well. For example, Knight et al.[16] observed substantially enhanced stabilities for certain sizes (8, 20, 40, 58 etc.) in the abundance (mass) spectrum of sodium clusters which was later explained as the occurrence of electronic shell closing in these specific sizes of sodium clusters using the jellium model. The clusters can also display a variety of bonding such as metallic, ionic, covalent or van der waals[17]. An attribute associated with the clusters, being so small, is the high surface to volume ratio, thus implying a larger number of atoms occupying the surface, thereby making them an ideal candidate for catalysis. All these different characters have contributed in stimulating the general interest and to the extensive study of atomic clusters over the past few decades[5, 3, 18, 19].

1.1.1 *Solid-liquid-like* phase transition

Being a finite framework in all the three dimensions leads to unusual properties exhibited by the atomic clusters including the characteristics at finite temperature. Before discussing the phase transition phenomenon in atomic clusters, a brief description of what melting *means* in bulk systems is presented. To understand the melting phenomena, three key terms must be explained.

Entropy

Entropy is a measure of the number of possible ways, a particular energy (E) can be distributed in a system of atoms. At equilibrium, atoms of the system have the same average energy. However, if observed at different instants of time, it is unlikely that all the atoms have the same exact energy owing to the constant energy transfer occurring due to their interaction. A *microstate* is an instantaneous catalogue that describes the energy of each participating atom in the system. Ludwig Bolzmann derived a a relationship for entropy as a function of the number of possible

microstates (Ω) of a system

$$S = k_B \; ln\Omega, \tag{1.1}$$

where k_B is the Boltzmann's constant. For any spontaneous process to occur, the total entropy change for the system and its surroundings must be positive as also stated by the second law of thermodynamics. Furthermore, since for a real system comprising a number of molecules of the order of Avogadro number, calculating the entropy from the number of possible microstates can be really challenging, it is generally calculated in terms of measurable macroscopic quantities such as the heat capacity of the system.

Temperature

For a system with constant volume (V) and number of particles (N), temperature is defined as the derivative of the entropy (S) with respect to energy (E) of the system as

$$\frac{1}{T} = \left.\frac{\partial S}{\partial E}\right|_{N,V}. \tag{1.2}$$

Entropy is a macro state parameter and statistically, for a spontaneous process the microstates of any system will evolve to maximise its entropy. This is called *equilibrium*. The above definition (Eq. 1.2) allows us to understand how the temperature and entropy are related at equilibrium.

Next, a brief description of the thermodynamics of solid-liquid melting transition in the bulk phase and clusters is presented.

Melting of bulk systems

Melting is the transition from a *solid* phase* to a *liquid* phase occurring at a particular temperature called the "melting temperature". When a homogeneous ordered solid is heated, the atoms, at low temperatures, exhibit harmonic oscillations about their mean position with small amplitudes. As the temperature increases, the amplitude of these vibrations also increases and a stage comes when the atoms display anharmonic vibrations, thereby leading to a disruption of 'bonds'. The atoms start to diffuse within the system and the solid and liquid phases coexist. At this stage, a further supply of energy does not lead to an increase in the temperature of the system but changes its phase completely to liquid. Ehrenfest's classification[20, 21]

*Here, a phase refers to an equilibrium thermodynamic state of a substance over a range of thermodynamic variables such as temperature, pressure, volume etc.

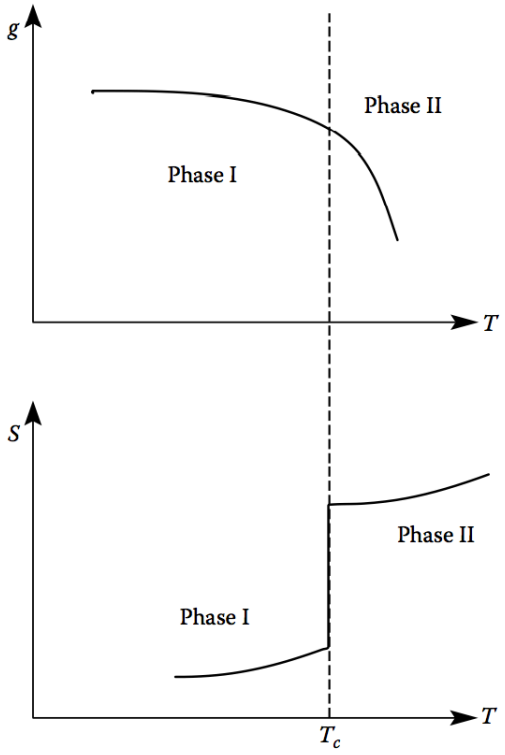

Figure 1.1: A diagram showing the changes in the Gibb's free energy per particle ($g = G/N$) and entropy (S) as a function of temperature (T) for an N particle system. Here, T_c is the critical temperature where the first order phase transition occurs. (Reproduced with permission from Ref.[17])

characterises melting as a 'first order phase transition' as

$$S = -\left.\frac{\partial G}{\partial T}\right|_P . \tag{1.3}$$

Here G is the Gibb's free energy, T is the temperature and S is the entropy. A schematic diagram showing the changes in the Gibb's free energy per particle, g, and entropy as a system goes from a solid state to a liquid state is shown in Fig. 1.1. Another description of the first order phase transition in a macroscopic system, the modern classification, incorporates the latent heat. As sketched in Fig. 1.2, the transition is characterised by a sudden jump in the caloric curve at the melting temperature[22]. The term *heat capacity* represents the ratio of the amount of heat absorbed by (or removed from) an object to the change in its temperature. At the melting temperature T_m, the heat capacity plot exhibits a peak.

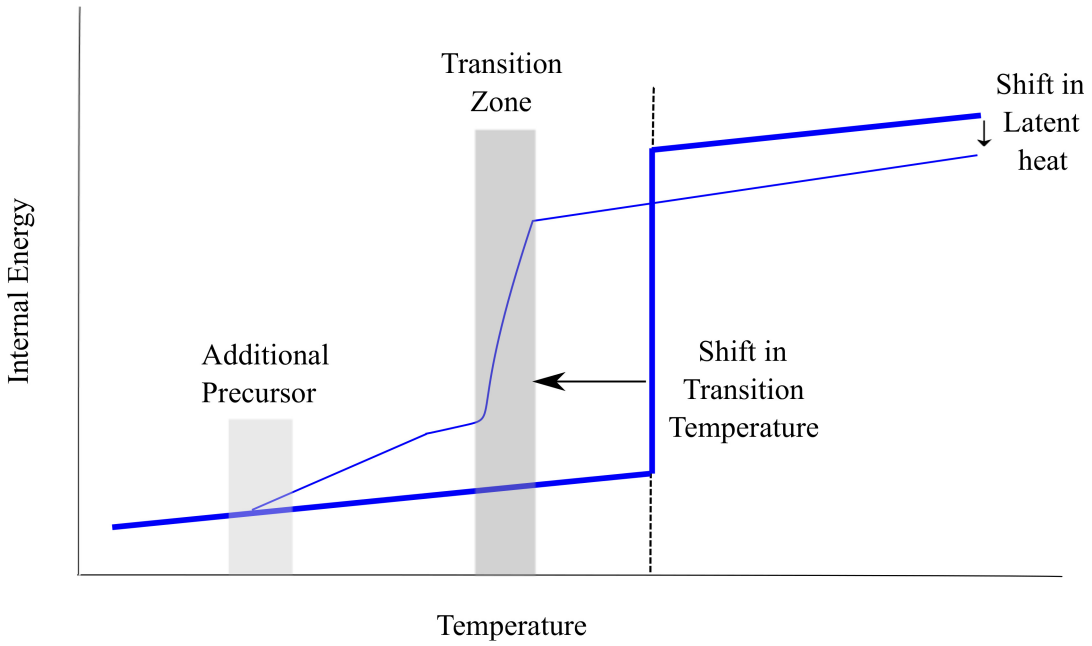

Figure 1.2: A comparison of the solid liquid phase transition as observed in bulk phase (thick blue line) and in clusters (thin blue line). (Reproduced with permission from Ref.[23])

Melting in clusters

Compared to the ordered extended systems, the finite temperature characteristics displayed by the atomic clusters are significantly different[24, 25, 26, 27, 23]. Unlike the bulk phases, the finite size systems do not show a sharp transition from one phase to another which has resulted in a distinction being made in the literature, and their states being referred to as *solidlike* and *liquidlike* at different temperature ranges and the phenomenon itself being also referred to as *phase transformation*[†] . The clusters have a high surface to volume ratio and each atom can have different 'bond strengths' with which it is bonded to its surrounding atoms; so the dynamical response to heating is different for each atom unlike the bulk phase and hence, the melting process is gradual[17].

Furthermore, the shapes and sizes of the atomic clusters also affect the nature of the phase transition thus reflecting a sense of *individuality* associated with them. Even an additional atom can bring about significant changes to the finite temperature behaviour reflected by changes in the melting temperature and the overall shape of the heat capacity curve, which is a derivative of the caloric curve, the melting temperature being the temperature corresponding to the peak in the heat capacity

[†]In this thesis, both the terms, *phase transition* and *phase transformation* have been used interchangeably.

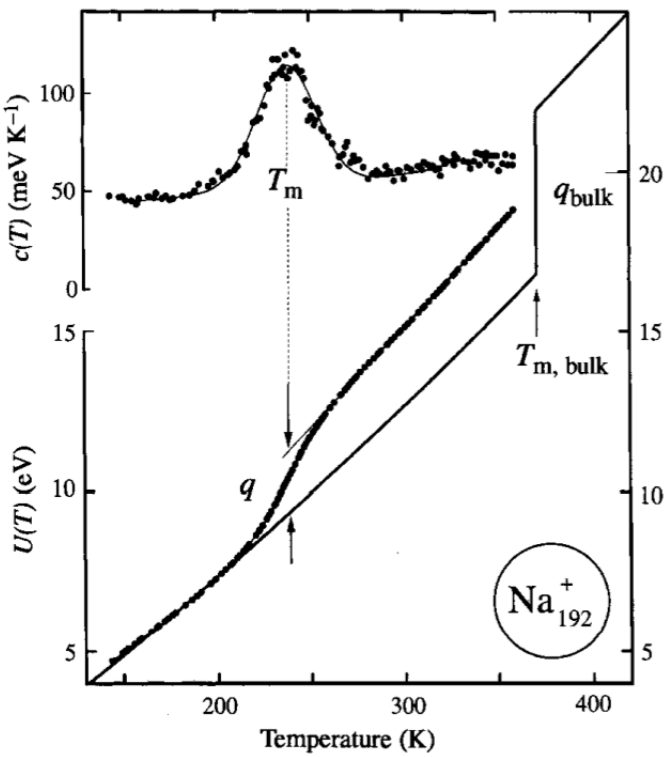

Figure 1.3: Heat capacity and the caloric curve for Na^+_{192} cluster where the solid dots show the value obtained from experiments. The temperature at which the specific heat is maximum is characterised as the melting temperature (T_m). The latent heat of fusion (q) is obtained from the height of the smoothed out step present in the caloric curve. The thick solid line is the caloric curve obtained for the bulk sodium and has been scaled for 192 atoms. (Reproduced with permission from Ref.[29])

curve. An example is shown in Fig 1.3. Also, below the melting temperature, the behaviour could be affected by the presence of different competing isomers for a given cluster size[28]. The heat capacity plot sometimes exhibits a peak or shoulder either below the melting temperature ($T < T_m$ i.e. *premelting*) or above the melting temperature ($T > T_m$ i.e. *postmelting*)

It is possible to identify different regions during the phase transition in a cluster as also shown in Fig. 1.2 (thin blue line). Below the 'additional precursor' [‡] and above the 'transition zone', a cluster is in a *solidlike* and *liquidlike* state respectively. However, between these two regions, both the phases coexist. Pre-melting and surface melting phenomena have been observed in few investigations [30, 31].

Experiments on atomic clusters to investigate the effects of temperature on various chemical and physical properties is done using nanocalorimetry. High-resolution microscopy and diffraction techniques help to study the structure and chemical or-

[‡]The 'additional precursor' region could signify either isomeric transitions or premelting.

dering in a cluster deposited on a substrate. Differential scanning calorimetry (DSC) is used to probe the phase changes such as melting. Information about the phase diagram can be obtained if the distribution in cluster size and composition is narrow and TEM measurements can also be used to observe phase transformations in individual nanoparticles[32]. Techniques such as mass spectroscopy provide a control on selecting a particular size, composition and also focussing on an individual (trapped) particle in the gas phase atomic cluster[33].

Haberland and co-workers[34, 35, 29] studied the melting temperatures, latent heat and change in entropy of sodium clusters with size between 55-355 atoms. The experimental method consists of first producing the ionic sodium clusters in a gas aggregation cell and is then thermalised in a heat bath which has helium gas at 70 Pa. After leaving the heat bath, the clusters are transferred to a region having high vacuum and are mass selected. As the temperature of the cluster increases, some atoms from the cluster are ejected. This is similar to the case when the cluster absorbs a photon of known energy and hence, the increase in the internal energy of the cluster due to an increase in the temperature equals the change in internal energy of the cluster due to a photon absorption. Thus, the caloric curve is extracted from the measurement of the mass spectra as a function of the heat bath temperature. Jarrold et al.[25] followed a different strategy where they estimated the internal energies of atomic clusters produced in the gas phase based on its propensity to dissociate leading to the determination of the caloric curve.

Some of the observations reported in experiments and theoretical studies, during the melting of atomic clusters are summarised below:

(a) Depression of melting point with size ($1/R$ scaling), was predicted in 1909 by Pawlow[36] by considering the importance of surface energies (which itself scales as $N^{2/3}$, where N is the number of atoms in the cluster) in the size range where surface to volume ratio cannot be neglected. Buffat and Borel demonstrated it experimentally for gold clusters[37]. However, for very small cluster sizes (N = 55-355) in sodium, Haberland et al. found the melting point to vary irregularly with size. Electronic and geometric effects (shell closings etc.) may work in tandem or for certain systems, one effect may dominate over the other in this small size range. In sodium clusters it is the geometric shell closing (the sodium cluster assumes icosahedral geometry) responsible for the substantially high melting point of $Na_{55}{}^{+}$[34, 35, 29].

(b) The shape of the heat capacity curve is sensitive to the size and ground-state geometry of the cluster[38].

(c) Clusters of gallium[25] and tin[39] have been observed, both experimentally and in theoretical simulations, to melt above their respective bulk melting temperatures. The *greater-than-bulk melting* behaviour shows that melting temperatures does not *necessarily* decrease with size as is observed in small sodium, gold and aluminium clusters[25, 37]. Some of the results from the experimental and theoretical simulations on gallium clusters have been presented later in the chapter.

1.2 Nanoalloys

Mixed atomic clusters comprising two or more metal atoms are referred to as the nanoalloys. Apart from all the variables (example size, shape and temperature) upon which the chemical and physical properties exhibited by a monometallic cluster depends, the properties (both, chemical and physical) of nanoalloys also depend upon the composition and chemical ordering of the participating atoms. This sensitivity offers the possibility of tuning their properties as per the desired application (catalysis, magnetism, plasmonics, optics or life sciences) and thus, has contributed immensely to the rapid growth in the study of nanoalloys[8, 9, 10, 11, 12].

Limiting the discussion to only bimetallic clusters, the 'structural phase' (as shown in Fig. 1.4) depends upon how the participating atoms interact with each other. In this respect, behaviour such as segregation or mixing is observed. Representing the participating elements in the bimetallic cluster as α and β, if the bond strength of $\alpha - \beta$ is stronger than that between $\alpha - \alpha$ and $\beta - \beta$, mixing is favoured which can be either random or ordered, else segregation occurs. Furthermore, segregation or mixing also depends on the following factors:

(a) Surface energy: the surface sites tend to get occupied by the metal having the lower surface energy.

(b) Atomic size: size mismatch between the atoms results in the atom with smaller size to occupy the internal sites and the larger atom occupies the surface sites resulting in the release of the strain.

(c) Charge transfer, strength of binding to ligands and in some cases specific electronic effects can also affect the observed behaviour of the nanoalloy phase.

Segregated bimetallic clusters generally observe configurations such as core-shell, onion-like or Janus-like (layered) as also shown in Fig. 1.4. Understandably, the question of structure assumed by a nanoalloy is one of the extensively reported

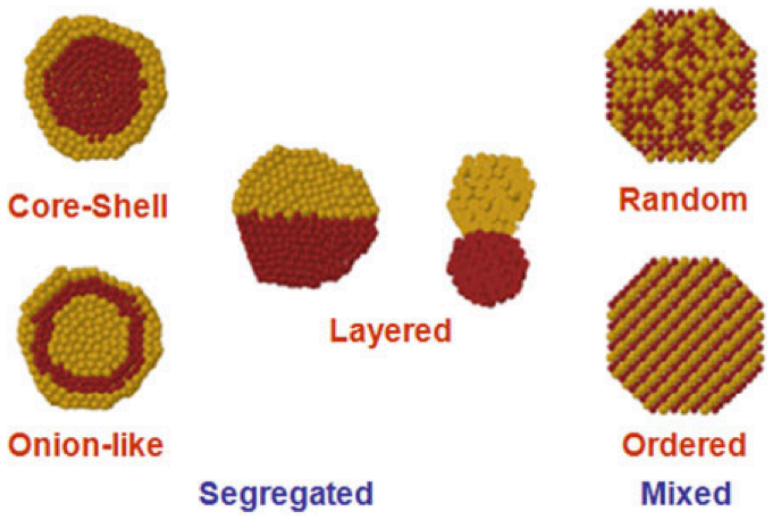

Figure 1.4: Different arrangements observed in nanoalloys. (Reproduced with permission from Ref.[8])

topics in the literature. Studies on the ground state configurations has obtained more attention[40, 41, 42, 43, 44, 45, 46, 47] with limited investigations of effects at finite temperature[48].

1.2.1 Homotops

Deducing the global minimum structure of a nanoalloy is extremely important to understanding the observed physical and chemical properties. However, the presence of two different types of atoms brings additional challenges since the properties of nanoalloys also depend upon the sites occupied by the atoms i.e. chemical ordering. In this sense, one can go a step further from monometallic clusters, where *every atom was important*, to this case where *every atomic site in the structure is also important.* A new class of isomers, referred to as homotops[49, 50], is defined to describe the alloy clusters, where a bimetallic cluster, composed of two different atoms α and β, $(\alpha_m\beta_n)$, with fixed number of atoms $(N = m + n)$ and composition $(m/n$ ratio), can assume a large number of structures, as shown by Eq. 1.4. Although the number of atoms in the cluster and the overall geometry stays fixed, the sheer fact that presence of either type of atom at a particular site can change the properties drastically imparts an extra degree of complexity to bimetallic clusters. The number of homotops in a given cluster is given by

$$N_H = \frac{N!}{N_m!N_n!} \ , \tag{1.4}$$

where N_H is maximised when $N_m = N_n$ i.e. a 50 : 50 mixture of elements α and β. Thus, as the cluster size increases, the number of homotops increases combinatorially, thereby making the search for the lowest energy structure of nanoalloy an extremely difficult task.

1.2.2 Thermodynamics of bimetallic clusters

To study the thermodynamics of nanoalloys computationally, two approaches are used: (a) classical thermodynamics, or (b) computer simulations based on Monte Carlo (MC) or molecular dynamics (MD) techniques. In the classical thermodynamics approach, finite-size corrections are added to the macroscopic models which have been developed for bulk phases. The Gibbs free energy for a spherical nanoalloy with elements α and β is given by

$$G(N) = x_\alpha[N\mu_\alpha + \sigma_\alpha N^{2/3}] + x_\beta[N\mu_\beta + \sigma_\beta N^{2/3}] + RT[x_\alpha lnx_\alpha + x_\beta lnx_\beta], \quad (1.5)$$

where x, μ and σ denote the mole fraction, chemical potential and surface energy respectively. Such models assume no segregation occurring between the two types of atoms and the interactions between them are the same as they are in the corresponding bulk alloy phase. Additional terms incorporating interfacial and strain energies have also been proposed[51].

Information at the atomic level is provided by computer simulation techniques such as MC or MD which use either analytical semi-empirical interaction potentials to model the interaction between the atoms or from the first principles (generally using the density functional theory). Melting transitions are captured nicely using the atomistic simulations. Two types of thermally induced transitions can occur in a nanoalloy: (a) order-disorder transition or (b) *solid-liquid-like* phase transition.

Order-disorder transition

The order-disorder transition is described in mixed nanoalloys where with increase in temperature, a nanoalloy undergoes transition from a well mixed ordered phase to a random disordered phase (refer to Fig. 1.4). Applications in high density information storage devices requires a control on the chemical order present in the nanoalloy, essentially to be kept in an ordered state, which affects the magnetism and magnetic moments of the overall cluster. Cobalt and iron based nanoalloys such as Co-Pt, Co-Rh, Fe-Pt and Fe-Pd have been observed to possess higher magnetocrystalline anisotropy in comparison to the Co-Cr based alloys currently used in the magnetic devices[52]. The order-disorder phase transition is of type first-order. Investigations

on such phase transitions have been performed on Fe-Pt[53, 54, 55] and Co-Pt[56, 57] nanoalloys, for which it was found to be dependent on the cluster size.

Solid-liquid-like phase transition

In spite of the rapid growth in the field of nanoalloys, limited experimental investigations have been done on the *solid-liquid-like* phase transition occurring in these systems. Jesser et al. [58] used transmission electron microscopy (TEM) to study the compositional dependence of the melting transitions in Bi-Pb nanoalloys and constructed a phase diagram. Jarrold and co-workers have investigated the effect of a single impurity on the melting temperature of clusters; anionic aluminium clusters with a copper atom[59] and cationic gallium clusters with an aluminum atom[60]. They found that the impurity had a significant effect on the melting temperature of clusters with variations depending upon the cluster size.

Mottet and co-workers[61] used the semi-empirical many body potentials in MD to investigate the effect of impurity such as nickel or copper on the melting of silver clusters. The impurity atom (smaller in size) occupying the internal site of the icosahedron geometry enhanced the thermal stability, owing to the strain relaxation, of the silver cluster and thus increased its melting temperature by as much as 50 K. Chandrachud et al.[62] observed a depression in melting point of Al_{13} and Ga_{13} clusters when doped with a single carbon impurity and Zorriasatein et al.[38] observed that adding a titanium atom impurity to silicon clusters, (size N = 15 - 20 atoms) prevents the fragmentation of the clusters up to 2200 K. In Pd-Pt nanoalloys, segregation of palladium atom to the cluster surface was observed in contrast to the bulk alloy phase which forms a solid solution at all compositions[63, 64, 65]. Extensive MC simulation[66] using many-body potentials has also been used to study the thermodynamic behaviour of silver clusters (size, N = 55 - 309 atoms) combined with either nickel, platinum or gold in a 3 : 1 ratio where the core and shell atoms melting at different temperatures was observed. Aguado and Lopez used the first principles based MD method to study the mixed alkali clusters[67]. A recent extensive review by Calvo highlights the developments in this field[23].

1.3 Gallium and aluminium

This section first introduces gallium and aluminium and provides an overview of the research question addressed in the body of this thesis.

1.3.1 Gallium

Various technological applications make gallium an important element in today's world. It is used in semiconductors, blue light emitting diodes (LED), multi-junction photovoltaic cells and high speed transistors[68]. Although it has been more than 135 years since gallium was discovered, yet it continues to puzzle scientists with its unique and anomalous properties. For example, unlike mercury which is the only other metal with a comparable melting temperature, gallium is a wetting metal. It expands up to 3% on freezing and fractures conchoidally rather than breaking along the defined planes.

Bulk phase

At ambient temperature and pressure, the stable structure of bulk gallium is α-Ga whose unit cell has eight atoms giving an impression of a base centered orthorhombic structure. Each atom in the unit cell has one nearest neighbour atom at a distance of 2.44 Å and the other six atoms are at 2.71 Å and 2.79 Å and leads to it being designated a 'molecular metal' [69]. Shown in Fig. 1.5(a) is a part of the bulk α-Ga structure showing two buckled planes which are connected as shown by the black line connecting the two atoms. The band structure of α-Ga in Fig. 1.5(b) shows the presence of a pseudogap which is related to the existence of a covalent bond between the two buckled plane atoms (coloured black) [70]. The charge density reflects a metallic nature within the buckled plane. Fig. 1.5(c) shows the unique unit cell of gallium with dimers arranged in buckled planes [71]. Gallium is extremely polymorphic and exhibits different solid-state phases at different temperature and pressure conditions [69].

The uniqueness of gallium is also reflected in its thermodynamic behaviour. The α-Ga phase has a melting temperature of 303 K i.e. it melts in one's hands. This is surprising since the cohesive energy of gallium is similar to that of silver (melting point 1234 K). The origin of such a low melting temperature of gallium still remains an unanswered question.

Melting in gallium clusters

Extensive calorimetric measurements performed by Jarrold and co-workers[72, 14, 73] on a series (17-55 atoms) of charged gallium clusters showed that melting occurs in these systems at temperatures significantly above the bulk melting temperature of gallium. This *greater-than-bulk melting* behaviour exhibited by the gallium clusters disproves the generality of the melting-point-depression with size paradigm of

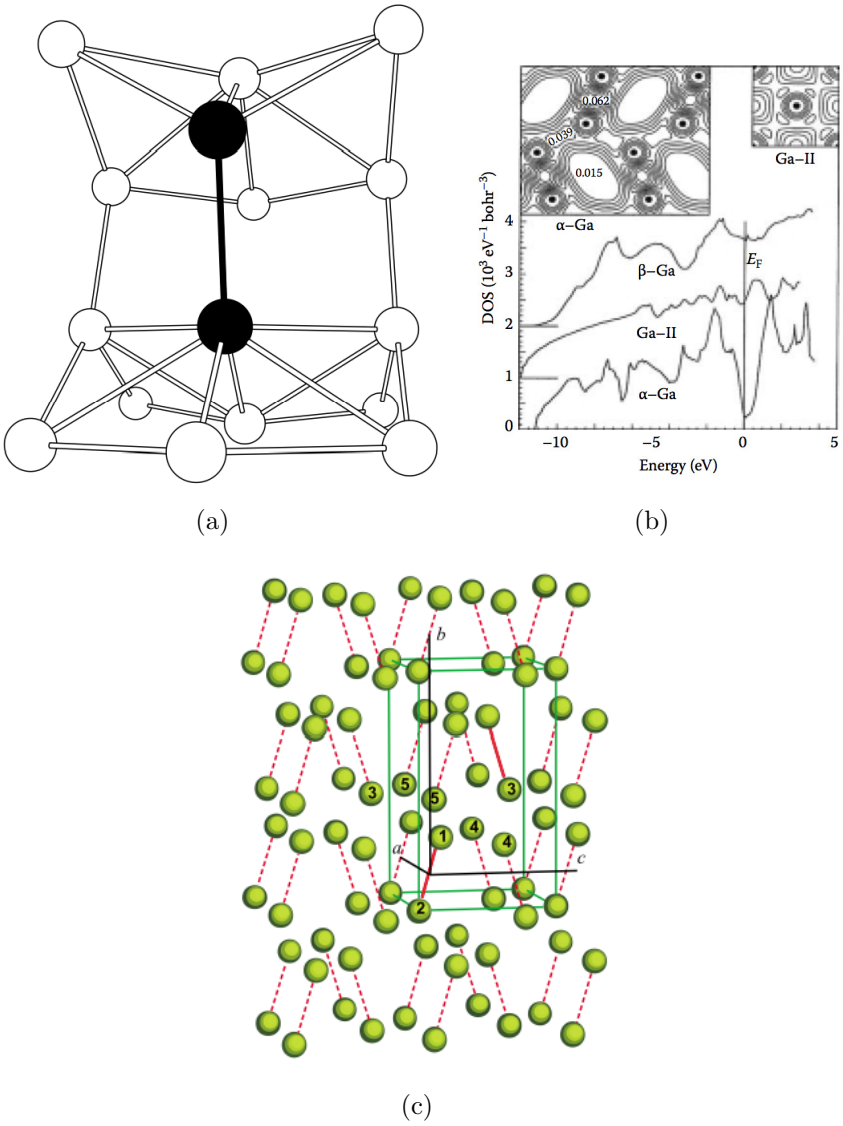

(a) (b)

(c)

Figure 1.5: (a) A part of α-Ga bulk structure showing a part of two buckled planes between which there is a covalent bond (represented as black). Note that this is not a unit cell representation. (b) A comparison between the electronic density of states of α-Ga, β-Ga and Ga II. The deep pseudogap observed in α-Ga is attributed to the presence of strong Ga_2 covalent bonding as shown in inset.(Reproduced with permission from Ref.[17]). (c) Gallium atoms arranged within the buckled planes of dimers. (Reproduced with permission from Ref.[71])

Pawlow[36]. Furthermore, a difference of one atom in the cluster size, as observed in Ga_{30}^+ and Ga_{31}^+, was observed to lead to drastic changes in the shape of the heat capacity curve. A recent study[74] from the same group found $N = 95$ atoms to be the first size in the range 60-183 atoms to melt below the bulk melting temperature of gallium.

Kanhere and co-workers[75, 76] used the electron localisation function (ELF)

analysis to infer the presence of covalent bonds, between the atoms of the charged gallium clusters, being responsible for their *greater-than-bulk melting* behaviour. However, this inference seems to rely on an over interpretation of the ELF and has been contested by several authors[13, 77]. A 'bond' is not a quantum mechanical observable and thus such interpretations on the nature of bonding need to address the orbitals involved in the process as well.

1.3.2 Aluminium

Aluminium is the most abundant metal in the earth's crust and is used extensively for various applications in industries. It is light, non-toxic and has a high electrical and thermal conductivity. It has a face-centred-cubic (*fcc*) lattice structure at low and normal pressure. A qualitative account of many characteristic properties of aluminium can be obtained from the free electron gas model [78, 79]. However, for a fundamental understanding of the metallic structure, accurate knowledge of electronic structure and chemical bonding is necessary. Although the electronic structure of the chemical bonds in aluminium has been extensively investigated, a consensus has yet to be reached on the details of their orientation within the *fcc* lattice, as demonstrated by the experimental and theoretical analysis of the electron density[80]. Bridge bonding between nearest neighbours [80], second nearest neighbours having octahedrally-centred bonds [81, 80], nearest neighbours having tetrahedrally-centred bonds [82, 80] or a mixture of all these modes [80] has been proposed. Bulk aluminium melts at 933 K [83]. Both classical and first principles based simulations have been extensively used over the past few decades to capture the melting transitions in bulk *fcc* aluminium crystal [84, 85].

Melting in aluminium clusters

In aluminium clusters, although the experimental heat capacity curves have been reported for cationic cluster sizes $N \geq 16$, the presence of peaks in the canonical heat capacity curves appear for aluminium clusters having 28 or more atoms[86]. The clusters melt below the bulk melting temperature of aluminium (933 K). In most cases, a single peak in the heat capacity curve is obtained. However, for Al_{51}^+, Al_{52}^+, Al_{115}^+, Al_{116}^+ and Al_{117}^+, a premelting peak[31, 87, 88] is also observed in the heat capacity plot and a postmelting peak[86, 87] is observed for Al_{61}^+ and Al_{83}^+ clusters. The premelting peak has been attributed to a structural transition occurring in the cluster before it undergoes melting.

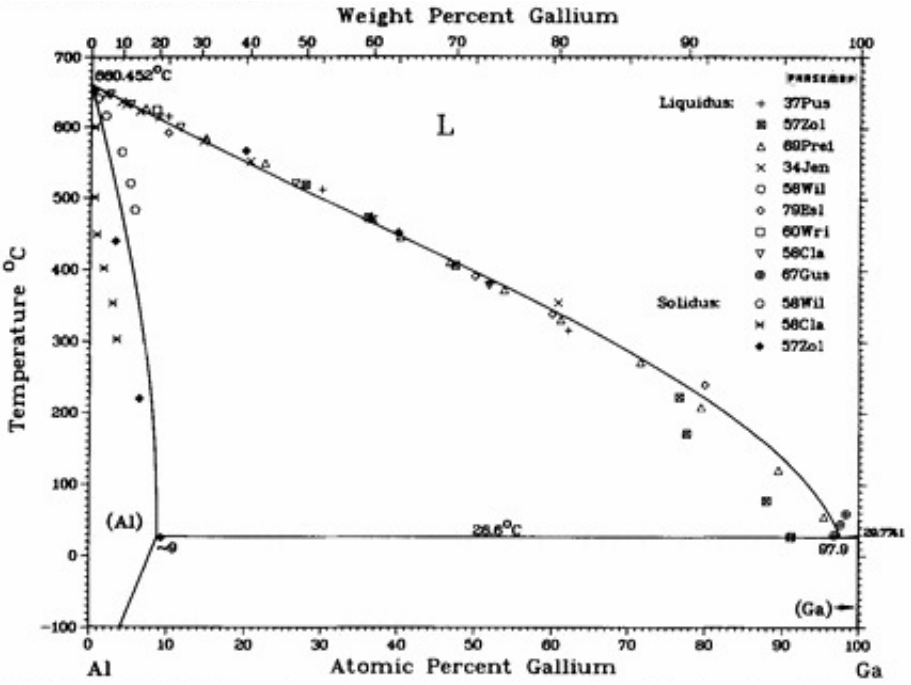

Figure 1.6: Phase diagram of gallium aluminium alloys. (Reproduced with permission from Ref. [95].)

1.4 Phase diagrams

Phase diagrams allow us to study the change in phases of the alloy as a function of composition and temperature. Nanoalloy phase diagrams, in addition, also depend upon the size of the system. Furthermore, phase diagrams of nanoalloys can also be constructed specifically to show the order-disorder transition or the *solid-liquid-like melting* transition. Phase diagrams for various nanoalloy systems such as Pt-Rh [89], Pt-Au [90], Cu-Ni [91, 92], Au-Cu [93] and Ag-Pd [94] have been constructed either by experiments or using the computational techniques described previously.

1.5 Gallium-Aluminium Nanoalloys

Bulk Ga-Al alloy is a simple eutectic system having a eutectic temperature of 26.6 ± 0.1 °C. In the equilibrium Al-Ga phase diagram [95] shown in Fig. 1.6 three phases appear: (a) the liquid alloy phase, (b) the face-centred cubic (*fcc*) Al and, (c) the complex cubic Ga. The solubility of Al in Ga is very low and the maximum solubility of Ga in Al is approximately 9 at.%.

Gallium-aluminium alloys have already been considered as a potential water splitter i.e. hydrogen generator[96]. Aluminium has always been known to fizz out hydrogen almost instantaneously on reacting with water. However, the reaction

halts at the surface of aluminium owing to the formation of an aluminium oxide layer thus preventing further reaction to occur. Gallium being liquid at room temperature (m.p. 29.7 °C) allows the aluminium oxide formed to stay localised in the gallium aluminium alloy. Aluminium clusters have been reported to be stable at 1000 K [97] and also argued to significantly increase the rate of hydrogen production when reacting with water [97, 98, 99] due to the increased surface to volume ratio.

This thesis investigates how the addition of aluminium affects the geometric & electronic structure and thermodynamics of cationic gallium clusters. Presence of experimental and modelled data for twenty atom gallium and aluminium monometallic clusters makes this size an ideal choice. For a twenty atom cluster size, gallium shows *greater-than-bulk melting* behaviour but aluminium does not. So, what happens when a bimetallic cluster $Ga_xAl_y^+$ is heated? Does it show *greater-than-bulk melting* behaviour for this nanoalloy mixture as well and how does the composition of individual atomic entities in this cluster impact the melting temperature of the nanoalloy? Employing first principles based calculations, answers to these questions have been provided in this work. Another aim of this study is to create a *solid-liquid-like* melting phase diagram for a twenty atom gallium-aluminium bimetallic cluster system and to understand the reasons behind the *greater-than-bulk melting* behaviour. The next chapter describes the theoretical background and the adopted methodology for performing the calculations and tools to analyse the generated data.

Chapter 2

Methodology

This chapter gives an overview of the methods employed in this research to study the thermodynamic properties of the gallium-aluminium clusters. A cluster is considered as a collection of ions surrounded by electrons. Density functional theory (DFT) is used to treat the interacting electrons (many-body system) followed by Born-Oppenheimer molecular dynamics (BOMD) for combining the electronic and nuclear degrees of freedom and thus, to study the evolution of the system over time. These methods have been described in the next few sections. The literature on DFT is large and some excellent reviews and collection of research papers cover it extensively[100, 101, 102, 103, 104, 105, 106, 107, 108].

2.1 Background

The full many-body Hamiltonian for a cluster system comprising N_a ions and N_e interacting electrons is given by

$$\hat{H} = \frac{-\hbar^2}{2}\sum_{I}^{N_a}\frac{1}{M_I}\nabla_I^2 + \frac{-\hbar^2}{2m_e}\sum_{i}^{N_e}\nabla_i^2 - \frac{1}{4\pi\epsilon_0}\sum_{I}^{N_a}\sum_{i}^{N_e}\frac{Z_I e^2}{|R_I - r_i|} + \frac{1}{4\pi\epsilon_0}\sum_{i}^{N_e-1}\sum_{j>i}^{N_e}\frac{e^2}{|r_i - r_j|} + \frac{1}{4\pi\epsilon_0}\sum_{I}^{N_a-1}\sum_{J>I}^{N_a}\frac{Z_I Z_J e^2}{|R_I - R_J|} \ . \quad (2.1)$$

Here the lower case and the upper case indices represent the electrons and the ions; M, m_e denote the mass of the ion and the electron and R, r give the ionic and electronic coordinates respectively. The first two terms in Eq. 2.1 represent the kinetic energy of ions and electrons respectively; the third term is the attractive potential energy between the nuclei and electrons ($\hat{V}_{eN}$ or $\hat{V}_{ext}$); the fourth and fifth terms are the repulsive Coulomb potentials associated with the electrons ($\hat{V}_{ee}$) and the nuclei

($\hat{V}_{NN}$) respectively. Using the Born-Oppenheimer (BO) approximation*[109], the true wave function ψ for the whole system can be approximated as

$$\psi(r_i\ , R_I) = \psi_{el}(r_i\ ; R_I)\ \psi_N(R_I), \tag{2.2}$$

where the electronic contribution is expressed by

$$\hat{H}_{el}\ \psi_{el}(r_i\ ; R_I) = E_{el}\ \psi_{el}(r_i\ ; R_I)\ , \tag{2.3a}$$

$$\hat{H}_{el} = \hat{T} + \hat{V}_{ee} + \hat{V}_{eN}\ , \tag{2.3b}$$

$$\hat{T} = \frac{-\hbar^2}{2m_e} \sum_i^{N_e} \nabla_i^2\ , \tag{2.3c}$$

and the nuclear part is solved as

$$(V_{NN} + E_{el})\ \psi_N(R_I) = E\ \psi_N(R_I), \tag{2.4}$$

respectively. Although BO approximation simplifies the problem of solving the Schrödinger equation for the full system of ions and electrons

$$\hat{H}\ \psi(r_i\ , R_I) = E\ \psi(r_i\ , R_I), \tag{2.5}$$

the many body term V_{ee} still stays intractable. This problem was reduced by Hohenberg, Kohn and Sham to an effective one-electron problem by replacing the interacting electron system by a non-interacting one having the same electronic charge density.

2.2 Density Functional Theory

Hohenberg and Kohn proved two theorems[110] and thereby laid down the foundations of density functional theory (DFT) in 1964. Very generally, the two theorems are:

1. The external potential, V_{ext}, is uniquely determined by the ground state electronic charge density $\rho_0(r)$†.

2. The ground-state energy, a functional of the electronic charge density, attains

*The nuclei being heavier than electrons ($M_I >> m_e$) move much slower than them. Thus, it is assumed that the electrons *instantaneously follow* the motion of the nuclei, thereby allowing for a separate treatment of the electronic and nuclear degrees of freedom.

†The single particle electronic charge density is defined as
$\rho(r) = N_e \int \cdots \int |\psi(r, r_2, r_3, , r_{N_e})|^2 d^3r_2 d^3r_3 \cdots d^3r_{N_e}$

its minimum value with respect to variations in the electronic charge density when the system is in its ground state i.e. the correct ground state electron density minimises the ground state energy functional for the many-body system.

Based on the two Hohenberg-Kohn theorems, Kohn and Sham (KS) presented a formulation[111] of DFT which led to its practical implementation. For a system with N_e electrons, the total electronic energy can be written as

$$E[\rho] = F[\rho] + \int V_{ion}(r)\rho(r), \tag{2.6a}$$

$$with, \quad F[\rho] = T[\rho] + E_c[\rho] + E_{xc}[\rho]. \tag{2.6b}$$

Here, V_{ion} is the external potential due to N_a ions, $T[\rho]$ is the kinetic energy of the interacting electrons having charge density $\rho(r)$, E_c is the electronic Coulomb energy and E_{xc} contains all the additional effects i.e., the exchange and correlation parts.

Kohn-Sham formulation replaces the exact kinetic energy functional of interacting electrons, $T[\rho]$, by that of a non-interacting electronic system having the same electron density ρ i.e. $T_s[\rho]$ and the exchange-correlation energy functional is redefined to include the quantum corrections as

$$E_{xc}[\rho] = E_{xc}^{exact}[\rho] + T[\rho] - T_s[\rho]. \tag{2.7}$$

The Kohn-Sham total energy functional[‡] is given by

$$E[\{\psi_i\}, \{R_I\}] = T_s[\{\psi_i\}] + E_c[\rho] + E_{ext}[\rho, \{R_I\}] + E_{xc}[\rho] + E_{ion}, \tag{2.8}$$

where ψ_i are the single particle wave functions, R_I are the ionic coordinates and $\rho(r)$ is the electronic charge density given by

$$\rho(r) = \sum_{i}^{occ} n_i |\psi_i(r)|^2. \tag{2.9}$$

Here, n_i denotes the occupancy of the ith eigenstate with the sum performed over all the occupied states. In Eq. 2.8, the first three terms representing the exact kinetic energy for the system of non-interacting electrons, the classical Coulomb energy and

[‡]Here each electron is being viewed to move in an effective field due to all the other electrons.

the electron-ion interaction (external) energy contribution are calculated as

$$T_s = \sum_i n_i \int \psi_i^* \left[-\frac{\nabla^2}{2} \right] \psi_i \, dr, \tag{2.10a}$$

$$E_c = \frac{1}{2} \int \int \frac{\rho(r)\rho(r')}{|r - r'|} \, dr \, dr', \tag{2.10b}$$

$$E_{ext} = \int V_{ion}(r)\rho(r)dr, \tag{2.10c}$$

respectively. The exchange-correlation energy contribution is represented by the fourth term E_{xc} whose exact form is known only for a few idealised systems. Hence, approximations are necessary to evaluate the value of E_{xc}. Local density approximation (LDA)[111, 112] is one of the most widely used forms to evaluate E_{xc}, where a parametrized form for an inhomogeneous electron gas is constructed from that of a homogeneous electron gas. Given by

$$E_{xc}^{LDA} = \int \rho(r)\epsilon(\rho)dr, \tag{2.11}$$

where $\epsilon(\rho)$ is exchange-correlation energy per particle for a uniform electron gas of density ρ, LDA has been by and large successful[103], in describing ground state properties of various systems having ionic, covalent or metallic interactions. However, being a purely local approximation makes LDA appropriate for systems where the electron density varies slowly such as simple metals. For inhomogeneous systems where the electron distribution is unlike that of uniform electron gas, such as transition metals, molecules, ionic crystals and surfaces, the LDA approximation is not accurate. LDA over binds these systems with the resulting lattice constants and bond lengths being too small.

Going beyond LDA, *generalized gradient approximations* (GGA) have improved the exchange-correlation energies estimations. It is expressed as

$$E_{xc}^{GGA} = E_{xc}^{LDA} + \int \rho(r) f_{xc}[\rho(r), \nabla\rho(r)]dr. \tag{2.12}$$

The choice of f_{xc} is not unique and various forms[113, 114, 115] have been proposed in recent years, rendering DFT to be an approximate formulation. There is already a veritable plethora of exchange-correlation functionals[116, 117, 118, 119] in use today and it remains an area of active research.

The last term E_{ion} in Eq. 2.8 represents the Coulomb energy due to ionic contributions which is a constant for a fixed ionic position is expressed as

$$E_{ion} = \sum_{I} \sum_{J \neq I} \frac{Z_I Z_J}{|R_I - R_J|}. \tag{2.13}$$

Here Z_I denotes the nuclear charge on the Ith nucleus. At its minimum value, the Kohn-Sham energy functional corresponds to the ground state energy of the system. Following the variational procedure, we get a set of equations (known as *Kohn-Sham* equations) from which the electronic state functions ψ_i which minimises the Kohn-Sham energy functional is obtained

$$\left[-\frac{\nabla^2}{2} + V_{eff}(r) \right] \psi_i(r) = \epsilon_i \ \psi_i(r). \tag{2.14}$$

The effective potential V_{eff} is given by

$$V_{eff} = V_c(r) + V_{ion}(r) + V_{xc}(r), \tag{2.15}$$

where

$$V_c(r) = \int \frac{\rho(r')}{|r - r'|} dr', \tag{2.16a}$$

$$V_{xc}(r) = \frac{\delta E_{xc}[\rho(r)]}{\delta \rho(r)}. \tag{2.16b}$$

The above set of equations must be solved self-consistently to obtain the physical quantities E and $\rho(r)$. Further simplifications[120] to the density functional approach have been added to make the calculations, involving isolated molecules, clusters or crystals, computationally affordable on modern computer architecture.

- The use of Bloch theorem[121] to approximate V_{ext} as a periodic potential when considering a periodic arrangement of ions in a regular crystal lattice. For isolated molecules and clusters, a supercell approach is used. All this is done using the plane wave basis set to represent electronic orbital wave functions.

- Another approximation (pseudopotentials) based upon the observation that the core electrons largely remain unaffected by the chemical environment surrounding an atom is used to reduce the calculations from a complete description of all the electronic wavefunctions to considering only the valence electrons[122, 123]. Thus, it is assumed that the contribution of the core electrons to the total binding energy remains largely unchanged when isolated atoms form molecule or crystals.

The atomic wavefunctions are eigenstates of the atomic Hamiltonian and hence are orthogonal to each other. The core states are localised in the vicinity of the atomic nucleus and thus the valence states must oscillate rapidly in the region occupied by the core electrons so as to maintain the orthogonality. The rapid oscillation leads to a large kinetic energy for the valence electrons in the core region, and cancels roughly the increase in the potential energy due to Coulombic repulsion between the electrons.

The use of an effective *pseudopotential* replaces the effect of the core electrons. Furthermore, pseudo-wavefunctions are introduced which vary smoothly in the region occupied by the core electrons[124, 125, 126, 127, 128].

Corso et al.[129] found GGA approximations of the form proposed by Becke and Perdew (BP)[130, 131] and Perdew and Wang (PW)[113] to give total energies of atoms and cohesive energies of solids such as Si, GaAs and Al in closer agreement than LDA. Furthermore, they found that the pseudopotential approach is as good as the all-electron approach and among the two GGA exchange-correlation functionals, the PW functional resulted in values marginally and systematically closer to the experiments.

2.3 Born-Oppenhemier molecular dynamics (BOMD)

Molecular dynamics (MD)[132] is a simulation technique of mimicking the physical movements of atoms and molecules at finite temperatures. DFT, being a method for calculating the ground state properties, cannot by itself be used to study the behaviour of the system at finite temperatures. However, the BO approximation provides a way to couple the accurate electronic structure calculations with the dynamical equations of motion to obtain the ionic trajectories at finite temperatures.

As a first step, for a given ionic configuration, the electronic Schrödinger equation is solved. The traditional BOMD uses the obtained ground state electron density, in the next step, to update the position of the ionic cores using the time dependent Schrödinger equation, where the nuclear kinetic energy term corresponds to the temperature at which ion dynamics is to be observed

$$\big[T_N + E\big]\psi_N(R,t) = \iota\hbar\frac{\partial}{\partial t}\psi_N(R,t). \tag{2.17}$$

Our approach is to use the implementation in the Vienna *ab-initio* simulation

package[133, 134, 135, 136] where the ionic positions are updated based on Newton's laws of motion in the second stage. The force acting on a particular atom i is calculated as the negative gradient of the 'interaction' potential as

$$\begin{aligned} \frac{\partial P_I}{\partial t} &= F_I, \\ &= -\nabla_I E(R), \end{aligned} \tag{2.18}$$

where E is same as in Eq. 2.4 which contains the ground state electron density contribution in the form of an effective electronic field and the ion-ion potential energy. Using the Hellmann-Feynmann theorem[137, 138], the gradient of the effective electronic field can be equated to the expectation value of the gradient of the electronic Hamiltonian corresponding to the ground state electron density as

$$-\nabla_I \varepsilon_e^{eff}(R) = \langle \psi_0 | \nabla_I H_e(R) | \psi_0 \rangle, \tag{2.19}$$

thus allowing us to calculate the forces on the ions in a 'stationary' electronic picture.

Using Newton's laws of motion, the acceleration and thereby the position of an atom after the subsequent time step dt is determined using either the Verlet method[139] where the velocities are not calculated (on the fly) to compute the trajectory t

$$x_i(t+dt) = 2x_i(t) - x_i(t-dt) + \frac{F_i^x}{m_i} dt^2, \tag{2.20}$$

or the velocity Verlet algorithm[140, 141], which is used in VASP, where the velocities are explicitly calculated to obtain the atomic positions for each iteration

$$x_i(t+dt) = x_i(t) + v_i^x(t)dt + \frac{F_i^x(t)}{2m_i} dt^2, \tag{2.21a}$$

$$v_i(t+dt) = v_i^x(t) + \frac{F_i^x(t+dt) + F_i^x(t)}{2m_i} dt. \tag{2.21b}$$

In Classical MD[142, 132, 143], an empirical interaction potential, say V, is determined through which the ions are allowed to interact for a period of time imitating a "real" motion. The force, say the x-component, acting on a particular atom i is calculated as the negative gradient of this interaction potential

$$F_i = -\frac{\partial V}{\partial x_i}, \tag{2.22}$$

and the calculation of the ionic trajectory follows similar steps as described above. It must be noted that the computational cost of DFT-based MD is much higher, so

restricts the size of the system dramatically when compared to classical MD.

Steenbergen[144] performed classical MD simulations on small gallium clusters using the GaN Tersoff potentials[145] on Large-scale Atomic/Molecular Massively Parallel Simulator (LAMMPS)[146, 147]. Erratic and irregular canonical heat capacity plots were obtained for all the cluster sizes simulated. Inconsistencies in the caloric curves were also observed. This highlights the limitations of the application of classical MD in small Ga cluster systems. The electron-electron interactions should be considered explicitly to capture the underlying thermodynamics with sufficient accuracy, hence the need to apply first principles based MD techniques to study such systems.

2.3.1 Parallel tempering

For a system which has numerous potential energy minima associated[148, 149], a faster scheme is necessary to not only explore the maximum potential energy surface in the limited simulation time but also to reach faster convergence with first principles based MD. Parallel tempering is a method designed for this case. Parallel tempering, also known as replica exchange, involves parallel runs (copies) of the system at different temperatures. After a constant number of time-steps, two configurations (temperatures) are selected and based on the calculation of an acceptance probability, swapping is either accepted or rejected. The main idea is to make configurations at high temperatures available to low temperature runs and vice versa resulting in a very robust ensemble which is able to sample both low and high energy configurations.

In the MD calculations reported in this thesis, the parallel tempering scheme proposed by Calvo and co-workers[148] for the microcanonical ensemble is followed. The acceptance probability, which defines the rate at which a configuration r_1 can be swapped with another configuration r_2 at two different energy trajectories E_1 and E_2 in a microcanonical ensemble is given by

$$acc(r_1 \rightarrow r_2) = min\left(1, \frac{\rho_{E,L}(r_2)T(r_2 \rightarrow r_1)}{\rho_{E,L}(r_1)T(r_1 \rightarrow r_2)}\right), \tag{2.23}$$

where $T(r_2 \rightarrow r_1)$ is the trial probability and $\rho_{E,L}(r)$ is the microcanonical weight or the equilibrium distribution given by

$$\rho_{E,L}(r) = \zeta^{-1}\frac{1}{\sqrt{det\ I}}\Theta[E - U_L(r)][E - U_L(r)]^{3N/2-4}. \tag{2.24}$$

Here I is the inertia matrix, ζ is the normalisation factor, Θ is the Heaviside step

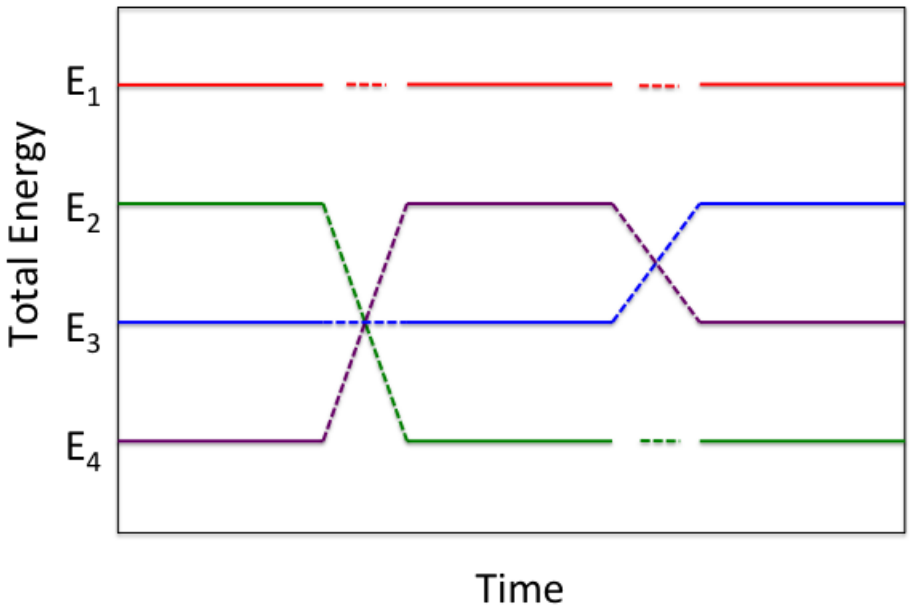

Figure 2.1: An illustration of the parallel tempering molecular dynamics in the microcanonical ensemble. Each colour represents a different configuration.

function with $U_L(r)$ being the angular momentum (L) contribution to the potential energy. Eq. 2.23 ensures that the configurational "random walk" samples the configurational space according to the equilibrium distribution as described in Eq. 2.24. In the microcanonical ensemble, the quantity $T(r_2 \rightarrow r_1)$ is replaced by the microcanonical weight as described in Eq. 2.24 and assumes the final form as

$$acc(r_1 \rightarrow r_2) = min\left(1, \left(\frac{[E_1 - U(r_2)][E_2 - U(r_1)]}{[E_1 - U(r_1)][E_2 - U(r_2)]}\right)^{\frac{3N}{2} - 4}\right). \tag{2.25}$$

Here, $U(r_i)$ denotes the effective rotational-vibrational potential energy for configuration r_i. The obtained acceptance probability is compared to a random number[§] between 0 and 1, and if found greater then the swapping is accepted or else rejected. Fig. 2.1 shows a general schematic overview of the parallel tempering process. After a particular number of MD steps, say n, all the trajectories are stopped and two are randomly selected. The acceptance or rejection of the swapping process is based on the calculated acceptance probability as described in Eq. 2.25. The two configurations are swapped is swapping is accepted and all the trajectories are resumed for the next n steps.

[§]The random number must satisfy two properties: uniformity and independence.

2.4 Simulation details

The DFT calculations have been performed using the large core (i.e. considering only $3s^2 3p^1$ and $4s^2 4p^1$ as valence electrons in Al and Ga respectively) projector augmented wave (PAW) pseudopotentials[150, 151] and the generalised gradient approximation (GGA) in the Perdew Wang form (PW91)[152, 153] is used to approximate the exchange-correlation part of the total Hamiltonian as implemented in Vienna *ab initio* simulation package (VASP)[133, 134, 135, 136]. The choice of the pseudopotentials and the exchange correlation functional has been made after a detailed study on the gallium dimer (Ga_2), Ga_6 and Ga_{20} clusters as described in [144]. Furthermore, the settings for performing the DFT and molecular dynamics calculations has also been rigorously tested by Steenbergen[144]. For geometry optimisation of clusters, an energy cutoff of 350 eV was used which was reset to the default value (240.437 eV for Al and 134.733 eV for Ga), as provided by VASP, during the molecular dynamics runs. Born-Oppenheimer molecular dynamics (BOMD) calculations, as implemented in VASP, is performed for a small time in the canonical ensemble to better gauge the initial velocities for different temperatures in the subsequent microcanonical ensembles. Simulation parameters and MD time specific to each cluster have been mentioned in the following chapters. Parallel tempering is implemented as wrapper code to the BOMD where after every 100 time steps, two trajectories are randomly selected and based on the calculated acceptance probability (as described in the previous section) the structures are either swapped or the swapping is ignored. From hereby onwards, the word 'temperature', characterising the average kinetic energy per particle of the system, in the microcanonical ensemble refers to the average temperature considering all the particles in the system.

2.5 Statistical indicators of melting and structural dynamics

Melting in clusters refers to the phenomenon of phase transition from a *solidlike* state to a *liquidlike* state. Unlike bulk phases where the phase transition is indicated by a discontinuity (or singularity) in the thermodynamic variable at a particular temperature, in clusters the change is spread across a range of temperatures due to finite size effects. This section describes the statistical methods and indices used in this research to study the phase transition and the structural/dynamical changes with temperature in different gallium aluminium nanoalloy clusters.

2.5.1 Multiple histogram method

To evaluate the specific heat curves, the use of discrete analysis would give a single value of the specific heat for every microcanonical simulation. As outlined in Ref. [154], variance of the kinetic energy is used as a measure of the heat capacity and temperature in the microcanonical ensemble. The microcanonical specific heat is given by

$$c_v(E_1) = \left(\frac{3N-6}{2} - 1\right)\left[N\left(\frac{3N-6}{2} - 1\right) - N\left(\frac{3N-6}{2} - 2\right)\frac{Y_i}{Z_i^2}\right]^{-1}, \quad (2.26)$$

where N is the total number of atoms, i is the index which runs over each of the microcanonical trajectories and Y, Z is given by

$$Y_i = \left\langle K_i \right\rangle_t^2 \left\langle K_i^{-2} \right\rangle_t, \quad (2.27)$$

$$Z_i = \left\langle K_i \right\rangle_t \left\langle K_i^{-1} \right\rangle_t. \quad (2.28)$$

respectively. Here, K_i is the kinetic energy. The microcanonical temperature is given by

$$T(E_i) = \frac{1}{k_B}\left[\left(\frac{3N-6}{2} - 1\right)\left\langle K_i^{-1} \right\rangle_t\right]^{-1}. \quad (2.29)$$

Obtaining one specific heat value per energy simulation yielded specific heat curves with large error bars and lacked sufficient detail to discern the overall nature of the melting transition. This proved to be a significant limitation in our first principles MD investigation.

The multiple histogram (MH) method[155, 156, 27] provides a way to stitch together the thermodynamical behaviour from discrete temperature MD trajectories and thus obtain continuous thermodynamic quantities in the microcanonical and canonical ensembles respectively. As described by Calvo and Labastie[157], the normalised probability distribution for potential energies U at total energy E in a microcanonical run is

$$P(U;E) = \frac{\Omega_K(E-U)\ \Omega_C(U)}{\Omega(E)}, \quad (2.30)$$

where Ω_K and Ω_C are the kinetic energy and configurational (potential energy) density of states (DOS) respectively. Analytically, the kinetic energy density of states is given by

$$\Omega_K(K) = BK^{\frac{\nu}{2}-1}. \quad (2.31)$$

Here, only the vibrational degrees of freedom (ν) is considered which equals $3N-6$, N being the total number of atoms, and B being a constant. To determine the configurational density of states, consider a microcanonical run at total energy E_i. The probability of finding a configurational energy U_j between $\left[U_j - \Delta U/2,\ U_j + \Delta U/2\right]$ is equal to $p(U_j, E_i)\Delta U$ (or simply $p_{ij}\Delta U$), which numerically is given by

$$p_{ij} = \frac{n_{ij}}{\sum\limits_{j} n_{ij}}. \tag{2.32}$$

Here n_{ij} denotes the total number of configurational energies U_j between $\left[U_j - \Delta U/2,\ U_j + \Delta U/2\right]$ during the MD run. In the microcanonical ensemble, n_{ij} is expressed as

$$n_{ij} = \alpha_i (E_i - U_j)^{(3N-8)/2} \Omega_j, \tag{2.33}$$

where Ω_j is the binned configurational DOS and α_i is an additive constant. For every microcanonical run E_i, the n_{ij} obtained forms an approximately bell shaped histogram across the range of potential energies j. Evenly spaced selection of E_i's gives us good overlap between the different histograms, which is then used to determine the configurational DOS (Ω_C) and the total DOS (Ω_E) across the energy range given by

$$\Omega(E) = \int_0^E \Omega_K(K)\Omega_C(E-K)dK. \tag{2.34}$$

Coupling the calculated configurational and total DOS with the equations of the MH specific heat[158] gives us the continuous microcanonical and canonical specific heat curves from the discrete E_i microcanonical runs.

Convergence

To ascertain the convergence of the microcanonical runs at all the temperatures, the sliding window analysis technique[13] is used. The width of the window is kept constant, equal to the difference of the length of the microcanonical run and the equilibration time. The specific heat curves both in the microcanonical and the canonical ensemble are plotted for ten consecutive time windows which are incremented in 1 ps intervals. The convergence criteria over the ten consecutive time windows i.e. 10 ps, is: (a) the temperature corresponding to the peak in the canonical specific heat plot changes by less than 10 K, and (b) the energy corresponding to the microcanonical specific heat plot changes by less than 0.01 eV/atom. Also, the general character and overall shape of each specific heat curve has to remain consistent over all the time windows as well.

2.5.2 Root mean square (RMS) bond-length fluctuation

Distance fluctuation criterion is one of the empirical rules useful in predicting the onset of melting transition. The Berry parameter[159], loosely referred to as the Lindemann index, characterises the phase transitions in irregular finite systems by calculating the root-mean-square relative bond-length fluctuations. Calculated as

$$\delta_{rms} = \frac{2}{N \cdot (N-1)} \sum_{i>j} \frac{(< r_{ij}^2 >_t - < r_{ij} >_t^2)^{1/2}}{< r_{ij} >_t}, \tag{2.35}$$

where $<>_t$ denotes the time average of the quantity within brackets and the other symbols have their usual meaning, the index manages to replicate the bulk-like-behaviour by converging to an almost constant value, $\sim$0.3 for gallium clusters[13, 160], after the melting temperature. In bulk systems, the solid-liquid phase transition is reflected by sudden increases of 10-15% in the bond-length variance, δ_{rms} [161, 162].

2.5.3 Pair distribution function (PDF) and average coordination number

Denoted as $g(r)$, the averaged PDFs are the real space representations of correlations in atomic position[142]. Being independent of orientation, it is a useful tool when comparing different structures and also the changes in the structure at different temperatures. It is calculated as

$$g(r) = \frac{2}{N \cdot (N-1)} \sum_{i=1}^{N} \sum_{j>i} < \delta(|r_{ij}| - r) >, \tag{2.36}$$

where N denotes the number of atoms and r_{ij} represents the distance between the atoms i and j. An averaged pair distribution function plot shows the structure of the cluster with respect to all the constituting atoms, an example of a PDF is shown in Fig. 2.2 for a crystal lattice as shown in its inset. The average coordination number uses the nearest neighbour distance as cutoff to assess changes in the cluster structure over time and temperature. An average coordination number for a particular atom at a given temperature gives the average number of neighbouring atoms the concerned atom is surrounded by during the MD trajectory. Here, the cutoff distance for an atom to be considered a neighbour is the first minima in $g(r)$.

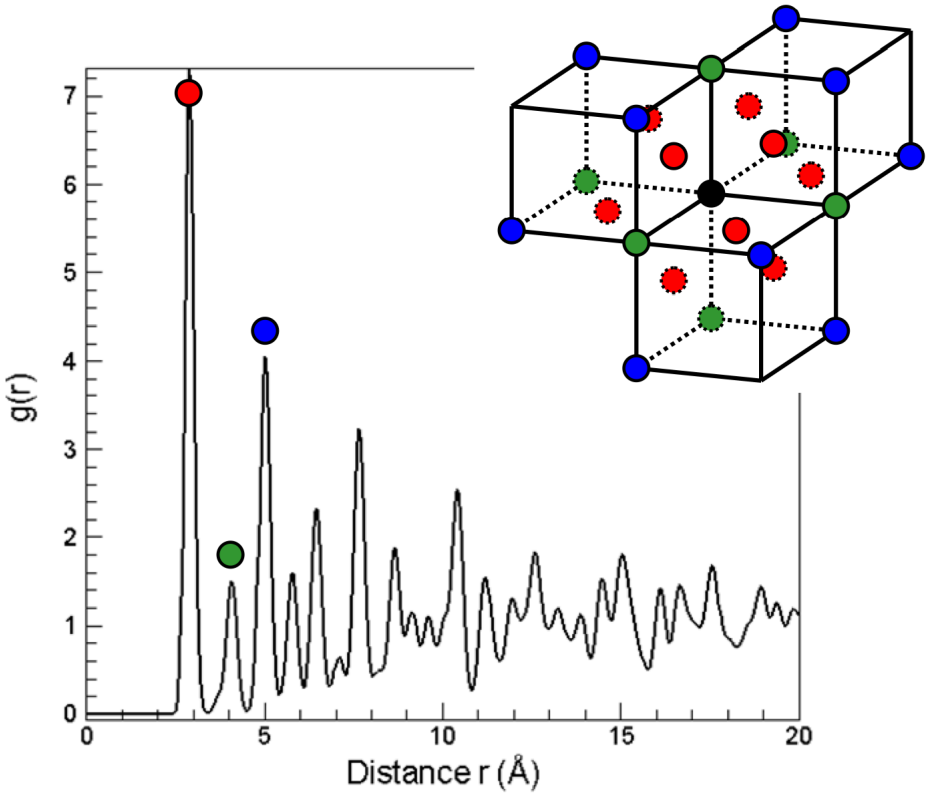

Figure 2.2: A plot of the pair distribution function calculated for a phase as shown in inset. The terminology is suggested in [163] and the picture has been obtained from Ref.[164].

2.5.4 Mean squared displacement (MSD) and diffusion coefficient

Unlike the Lindemann index which resembles a *'macroscopic'* analysis, the MSD can be obtained for each atom of the cluster thereby allowing an assessment of the individual i.e., *'microscopic'*, atomic contribution to the overall behaviour of the system. It is expressed as

$$\langle r_i(t) \rangle \;=\; \frac{1}{M} \sum_{m=1}^{M} [R_i(t_m + t) - R_i(t_m)]^2, \tag{2.37}$$

where R denotes the position of the *i-th* atom at the time within (), M is the number of time origins with other symbols as described previously. Using different starting points, i.e. time origins, to perform the MSD analysis allows the statistics to be independent of the time when calculation starts. Comparing to just one starting point can lead to spurious and unreliable results.

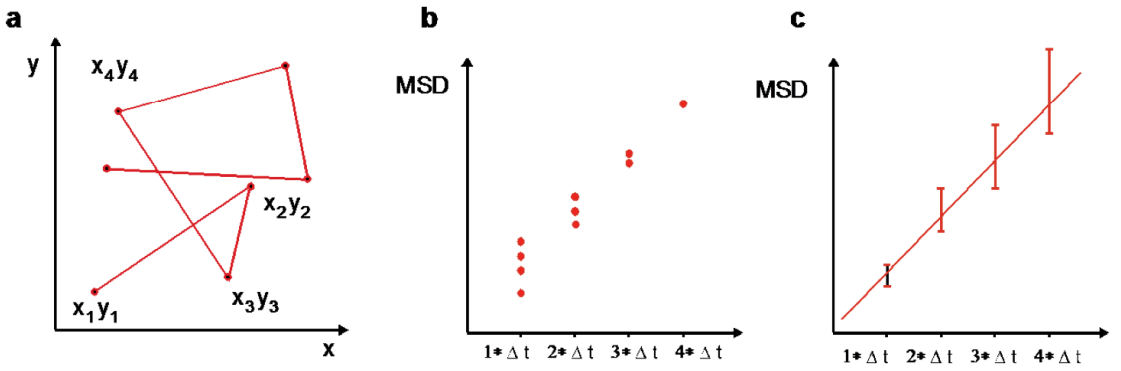

Figure 2.3: (a) Random walk in two dimensions at four consecutive time steps. (b) Plot showing squared displacements according to the time intervals. Note that the data becomes less for longer time intervals. (c) Average of all the data points at every time interval. The lesser the number of data points, the more the error. The picture has been obtained from Ref.[166].

The mean squared displacement allows us to calculate the diffusion coefficient, D, for each atom in the nanoalloy cluster. It is calculated as

$$D \equiv \frac{1}{2d} \lim_{t\to\infty} \frac{\langle r_i(t) \rangle}{t}, \tag{2.38}$$

where the numerator is the mean squared displacement of the atom i as described in Eq. 2.37, t is time and d is the dimensionality of the system (in our case 3). The slope of the MSD plot is calculated using a linear least squares regression fit, which is equal to $(2dD)$, from which the diffusion coefficient is obtained. Note that the mean squared displacement is proportional to the observation time only at sufficiently long times. Furthermore, for finite systems such as clusters, the diffusion coefficient is meaningful only over a small time range where the slope is constant[165]. An example of mean squared displacement for a two-dimensional random walk at four consecutive time intervals is shown in Fig. 2.3. As the time increases, the number of MSD data decreases thereby leading to an increase in the error. In the MSD data reported in this thesis, the time during which MSD is calculated for each atom of the cluster has been decreased appropriately, so that at all the time intervals the number of data points are the same. Moreover, the atoms of the cluster mimic a 'confined random walk' as shown in Fig. 2.4. Thus, after the initial few picoseconds, the MSD curve is expected to plateau as is shown in the next few chapters.

It should also be noted that all the methods described above to analyse the cluster structure and dynamics can get affected by the parallel tempering(PT) swaps. The intention of using the RMS bond-length fluctuation is to show the drastic change in

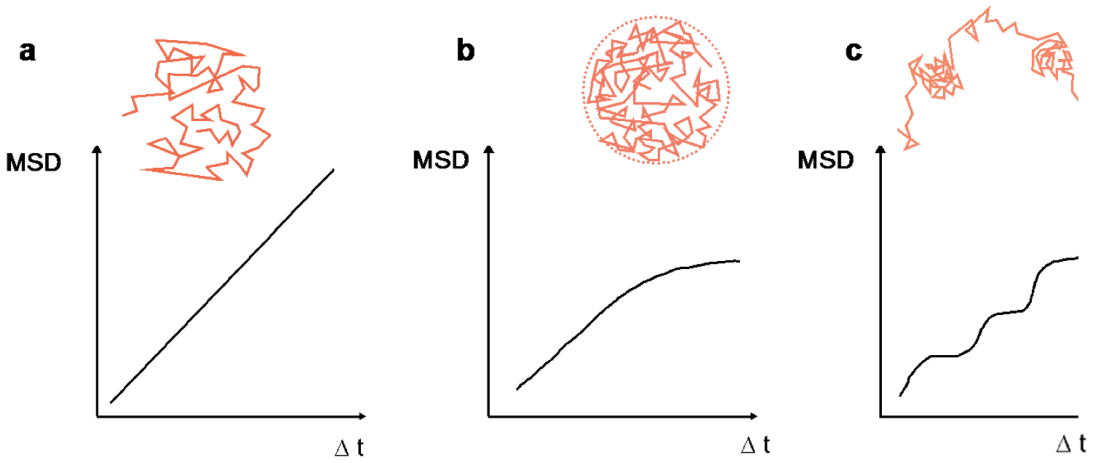

Figure 2.4: Different types of random walk and their corresponding plot: (a) isotropic, (b) confined and, (c) partially confined (hopping). The picture has been obtained from Ref.[166].

its value from the lowest energy run to the highest energy run simulated. Extensive testing revealed the values of δ_{rms} at the lowest and highest energy to be consistent with the PT-independent simulations. However, between these two regions the actual value of δ_{rms} must be treated with caution. The effect of PT was also minimal in the MSD calculations at the lowest and the highest energy. But in the phase transition region, it can also get affected by PT and hence instead of its actual value only the general trend is used in analysing the behaviour of the atoms.

2.5.5 Velocity auto-correlation function (VACF) and power spectrum

The indices described so far process the data obtained from the cartesian coordinates of the participating atoms and thus can get affected by parallel tempering. Velocity autocorrelation function (VACF) and the corresponding power spectrum[142] uses the velocity of the atoms to observe changes in the cluster with increasing temperatures, and thus remains unaffected by parallel tempering. It is calculated as

$$C(t) = \frac{\sum_{i=1}^{N}\sum_{j=1}^{M} \vec{v_i}(t_{0j}) \cdot \vec{v_i}(t_{0j}+t)}{\sum_{i=1}^{N}\sum_{j=1}^{M} \vec{v_i}(t_{0j}) \cdot \vec{v_i}(t_{0j})}, \tag{2.39}$$

where $C(t)$ represents the VACF at time t at the specified temperature and $\vec{v_i}$ represents the velocity of the atom i. To gauge the phase transition, it attempts to measure the correlations in atomic motion with time at different temperatures. For a cluster to be in a *solidlike* phase, the strongly correlated atomic motion is reflected

by the oscillatory behaviour of $C(t)$ with time. As the temperature increases, the atoms start to diffuse and the correlations in atomic motion tend to disappear with $C(t)$ becoming relatively flat around the 0 value of $C(t)$.

A Fourier transform of the velocity autocorrelation function is called the power spectrum or vibrational spectrum

$$I(\omega) = 2\int_0^\infty C(t) \cdot cos(\omega t)dt. \tag{2.40}$$

Here ω is the cyclic frequency. The power spectrum effectively translates the correlations in atomic motion over frequency and thus can help discern information about the individual atomic processes by analysing atom specific $I^i(\omega)$. To observe phase transition from power spectrum, Yen et al.[167] proposed that the phase transition temperature is one where the power spectra of the internal and surface atoms overlap. Furthermore, at this phase transition temperature the low frequency ω for all the atoms must become indistinguishable.

2.6 Partial atomic charges: Quantum theory of atoms-in-molecules (QTAIM)

To understand and characterise the ground state electron density of the clusters, the distribution of partial charges between the atoms of the cluster have been observed. The topology of the electronic charge density of the molecular system is used to define atomic boundaries within the molecule in the quantum theory of atoms in molecules (QTAIM) as formulated by Richard Bader[168]. An atom is considered an open system whose occupied volume (in the real space) is governed by the topological condition of zero-flux of the total electronic charge density

$$\nabla\rho(r) \cdot n(r) = 0. \tag{2.41}$$

An integration performed on the electron density associated within each atomic volume gives the charge density (*'Bader charges'*) associated with the corresponding ion of the molecule. Using this method, the calculated partial charges associated with each ion in the cluster is independent of the basis set used to calculate the total electronic charge density. A freely available software[169] is used to analyse the spatial charge distribution within the gallium aluminium nanoalloy clusters.

2.7 Electron localisation function

Electron localisation function (ELF) was originally proposed by Becke and Edgecombe [170] and further developed by Silvi and Savin[171] for using it with DFT and proposing the topological classifications. The pair electron density $P^{\sigma\sigma'}(\vec{r_1}, \vec{r_2})$ gives the probability of finding an electron with spin σ at $\vec{r_1}$ and another electron with spin σ' at $\vec{r_2}$ respectively. Because opposite spin electrons can occupy the same region of space as also stated by Pauli's principle, it becomes difficult to obtain and apply the opposite spin pair electron density in the context of electron localisation. Realising this, Becke and Edgecombe went a step further to use the same spin conditional pair electron density $P^{\sigma\sigma'}_{cond}(\vec{r_1}, \vec{r_2})$ i.e. the probability of finding an electron of same spin at $\vec{r_2}$ when for surety there is one at $\vec{r_1}$ as given by

$$P^{\sigma\sigma}_{cond}(\vec{r_1}, \vec{r_2}) = \frac{P^{\sigma\sigma}(\vec{r_1}, \vec{r_2})}{\rho_\sigma(\vec{r})}. \tag{2.42}$$

to formulate their theory. Note that the single electron density is a three dimensional quantity, so a pair electron density would be six dimensional. However, if the calculations are done with respect to $\vec{r}$ $(= (\vec{r_1} + \vec{r_2})/2)$ and s $(= |\vec{r_1} - \vec{r_2}|)$, the same spin conditional pair electron density becomes a four dimensional quantity viz. x, y, z coordinates of $\vec{r}$ and the scaler s.

Further to the theory, observation of conditional probability as s $\rightarrow$ 0 i.e. in the vicinity of electron at $\vec{r_1}$ (reference electron) requires a Taylor series expansion of $P^{\sigma\sigma}(\vec{r}, s)$:

$$P^{\sigma\sigma}(\vec{r}, s) = \frac{1}{3} \underbrace{(\tau_\sigma - \frac{1}{4}\frac{(\nabla\rho_\sigma)^2}{\rho_\sigma})}\, s^2 + \cdots, \tag{2.43}$$

where τ_σ is the kinetic energy density. Note that if the term in the bracket of Eq. 2.43 referred as D_σ is small, it means the probability of finding another electron of same spin near the reference electron is small i.e. the reference electron is localized. Scaling D_σ to the kinetic energy density of homogeneous electron gas D^0_σ $(= \frac{3}{5}(6\pi^2)^{2/3}\rho^{5/3})$, the ELF index is locked between 0 and 1 as shown in Eq. 2.44; the higher the value of ELF, the stronger the localization in that region

$$ELF = \frac{1}{1 + (\frac{D_\sigma}{D^0_\sigma})^2}. \tag{2.44}$$

Savin et al.[172] generalised the term D_σ for a spin independent pair electron density which is simply a measure of the excess kinetic energy density of the system

under study to the von Weizsacker kinetic energy density

$$D = \frac{1}{2}\sum_i (\nabla\phi_i)^2 - \frac{1}{8}\frac{(\nabla\rho)^2}{\rho}. \tag{2.45}$$

2.7.1 Topology analysis of ELF

In order to remove the arbitrariness of scaling in ELF, Savin et al.[172] proposed a topology based analysis. Transformation of the numerical scale into a colour scale (or isosurfaces) gives a qualitative feel to the whole analysis. The analysis focusses on characterizing electron pair regions with special emphasis on regions where ELF shows a maxima.

The position of maxima in ELF is known as an *attractor*. The *domain* or *basin* of an attractor represents all points in space from which the attractor is reached (by considering the path of steepest ascent). Consider the figure 2.5. Replicating the concept of isosurface in 1-D, a line is drawn where the ELF value is α. The points which fall on this line will represent a volume in 3-D i.e. volume enclosed by the isosurface. They are known as *f-domains*. Thus, there are three f-domains for the value α in the figure below. Notice, that if the α is decreased, a stage will come when there is only one f-domain, the difference being in the former case, each f-domain encloses one attractor but the latter enclose three.

If *f-domains* contain more than one attractor, they can be reduced (i.e., *reducible f-domains*) else they are referred as *irreducible f-domains*. Focussing next on the basins formed by the irreducible f-domains, if the basin contains a nucleus (proton excluded) it is called core basin (C) else a valence basin (V). Valence basin will always be connected to one core basin at least. A basin which represents a lone electron pair will be connected to one core basin and its attractor is referred as monosynaptic. A basin which represents a covalent bond will be connected to two core basins and its attractor is referred as disynaptic. Higher synaptic orders also exist. Hydrogen (containing no core electron) is an exception: its ELF appears to have a basin with large volume.

Bifurcation is another concept applied to ELF topologies. At very low ELF isosurface values, there is only one f-domain which can be further reduced. On increasing the ELF isosurface value, the basins start to separate (i.e. bifurcate) and more f-domains appear. The points of bifurcation signifies minima in the ELF function. Lower bifurcation values correspond to higher localization of the corresponding basins.

In the next chapter, a comparison of ELF topology of small gallium clusters using VASP and Gaussian[173] is provided. Different ELF topology from both the

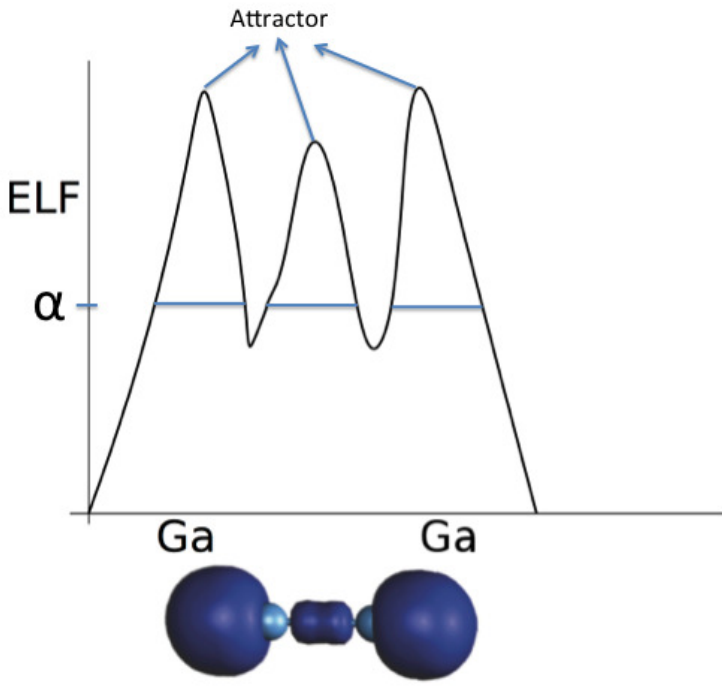

Figure 2.5: An example of the electron localization domain for a gallium dimer showing the presence of an attractor in between the two ionic cores.

softwares for the clusters reflects that any conclusion on the existent bonding in these systems should be attempted cautiously.

Chapter 3

Electron localisation function

Orthorhomic under normal conditions with four covalently bonded dimers in the unit cell: this describes the bulk phase of gallium (α-Ga) under standard conditions. It is the presence of these dimers which leads to a 'molecular-metal' picture [69]. In fact, the intermolecular energy obtained as the difference of bulk and dimer cohesive energies correlate nicely with the low melting temperature (303 K) of gallium [174].

To understand the *greater-than-bulk melting* behaviour of small gallium clusters, Kanhere and co-workers [175, 75, 17] used the electron localization function (ELF) topologies to address the underlying bonding in these systems. They observed that the ELF isosurfaces connected the gallium atoms in the cluster and hence concluded the existence of a covalent bond. Moreover, they attributed these covalent bonds to be responsible for the *greater-than-bulk melting* behaviour.

There are two aspects to this conclusion: (a) the connections of basins in the

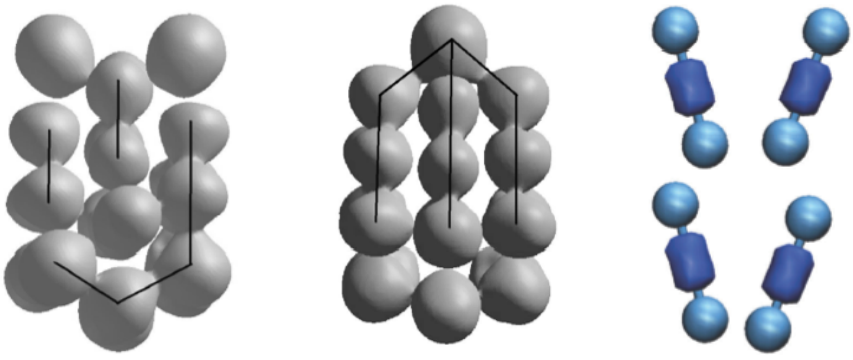

(a) Ga_{30} (b) Ga_{31} (c) α-Ga unit cell

Figure 3.1: (a) and (b) show the electron localization function (ELF) isosurfaces are at isosurface value ($\chi = 0.68$) and the black lines show the connected basins. (Reproduced with permission from [175].) (c) ELF topology for α-Ga bulk unit cell at isosurface value ($\chi = 0.65$). (Reproduced with permission from [160].)

ELF picture is a signature of the covalent bond, and (b) it is the covalent bond which is really responsible for the gallium clusters to show the *greater-than-bulk melting* behaviour. Steenbergen et al. [160] argue that the presence of a covalent bond between two atoms can be identified by the presence of attractors between them in the ELF topology as shown in Fig. 3.1(c). However, in the case of clusters they did not identify any attractor between the atoms disconnected from that of the ionic cores as the isosurface values were increased leading to doubts regarding the presence of covalency in these clusters. This illustrates the difficulty in interpretation of the electron localisation function.

This chapter compares the topologies of the electron localisation function obtained from two different softwares VASP [133, 134, 135, 136] and Gaussian [173] and tries to establish that ELF analysis is not *sufficient* to comment on the character of bonds in these systems. First the gallium dimer (Ga_2) is studied, followed by the pure gallium clusters in the size range 3 to 8 atoms.

3.1 Computational details

The details of the geometry optimisation calculations is the same as that described in the previous chapter. Density functional theory calculations in Gaussian 09 software used the PW91 exchange-correlation functional [152, 153, 176, 177, 178] with Dunning-type cc-pVTZ basis set [179]. ELF isosurfaces were obtained from the TOPMOD package [180]. The atomic visualisation and ELF topologies reported in this or the subsequent chapters have been obtained either using VESTA [181] or VMD [182] software.

3.2 Gallium dimer (Ga_2)

The electronic ground state for a gallium dimer (Ga_2) is $^3\Pi_u$ with the experimentally measured bond length value of 2.75 Å[183]. The bond length and binding energy calculated from Gaussian for the triplet $^3\Pi_u$ state is 2.73 Å and -0.803 eV/atom respectively. The ELF isosurface for the same is shown in Fig. 3.2(a). The highest and second highest occupied molecular orbitals (HOMO) and the lowest unoccupied molecular orbital is shown in (b) and (c) subfigures of Fig. 3.2 respectively. For the singlet $^1\Sigma_g^+$ state, the calculated bond length and binding energy values are 3.044 Å and -0.552 eV/atom respectively and the ELF isosurface is shown in Fig. 3.2(d). The bond length values are in close agreement with those calculated by Ralf and Gaston at BP86/TZ2P level of theory [184].

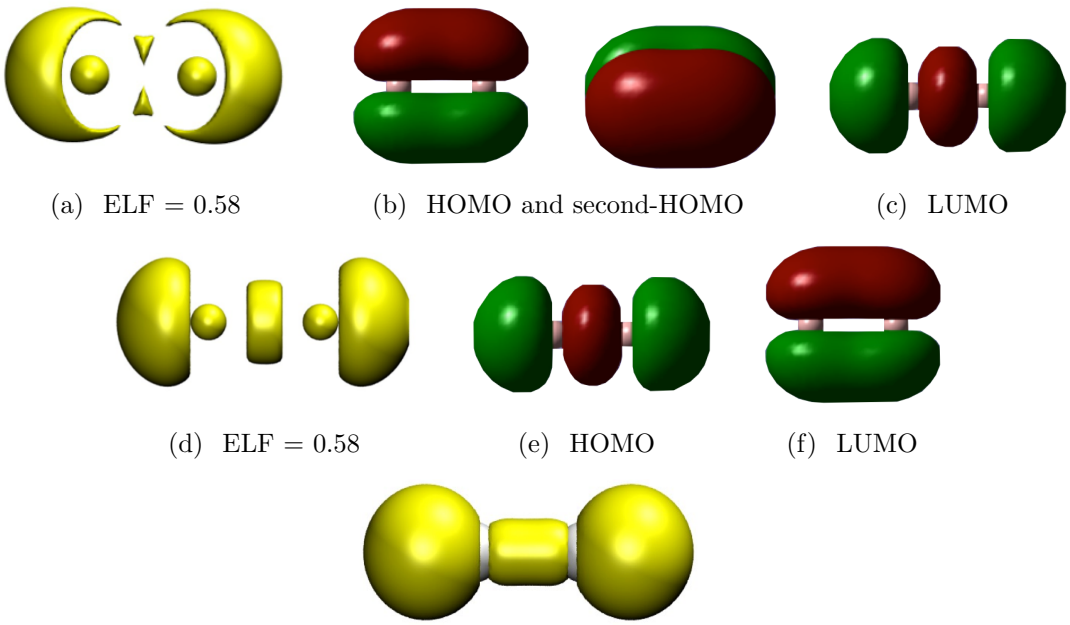

(a) ELF = 0.58 (b) HOMO and second-HOMO (c) LUMO

(d) ELF = 0.58 (e) HOMO (f) LUMO

(g) VASP (ELF = 0.58)

Figure 3.2: The triplet state ($^3\Pi_u$) (a, b, c) and the singlet state ($^1\Sigma_g^+$) (d, e, f) of Ga_2 as calculated from Gaussian. The obtained ELF isosurface for triplet Ga_2 from VASP is shown in (g).

The ELF isosurface pictures of the triplet and singlet states bring out significant differences in the topological shapes and the positions of the attractors. In the singlet $^1\Sigma_g^+$ state, the attractor between the core ion basin is a spherical ring as also reflected by the HOMO. However, in the case of the triplet $^3\Pi_u$ state of gallium dimer, the attractor between the core ion basin is bifurcated.

Calculations performed in VASP using a cell length of 15 Å, and all the other parameters as previously described, optimises the bond length of the gallium dimer in the triplet state to 2.725 Å and the binding energy obtained is -0.835 eV/atom. The ELF isosurface obtained for the triplet state is shown in Fig. 3.2(g). Thus, although the bond lengths of $^3\Pi_u$ state in the gallium dimer is almost the same, there is a clear difference in the ELF isosurface topology. VASP calculations use pseudopotentials to approximate the effect of core electrons and consider only the valence electrons ($4s^2 4p^1$) in the calculation of ELF. In Gaussian, an all-electron calculation is performed to obtain the ELF isosurface which makes it more reliable.

3.3 Small gallium clusters (Ga_n; n = 3-8)

For small gallium clusters, the initial geometries have been taken from [174] and the optimised geometries of Ga_4, Ga_6 and Ga_8 are in good agreement with the

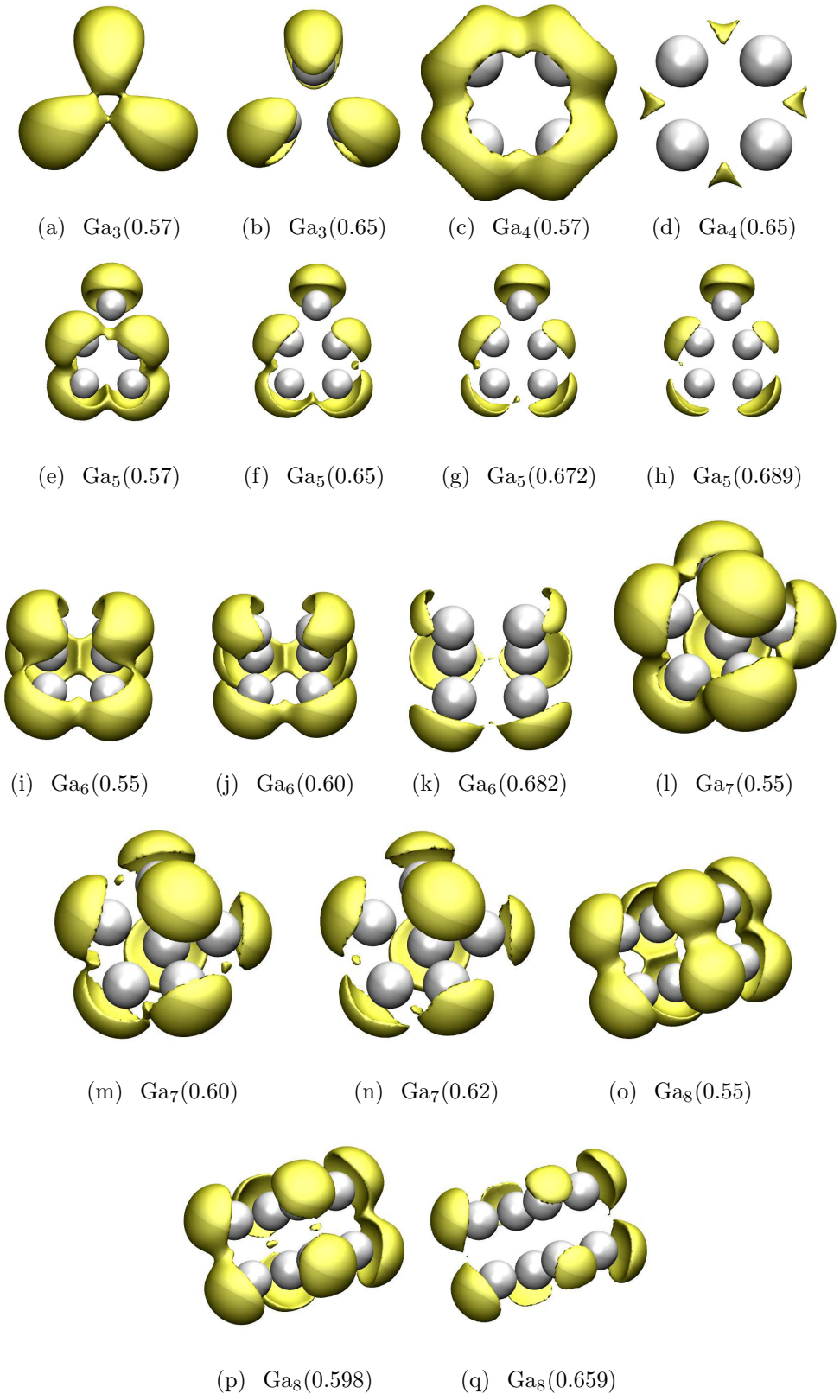

(a) $Ga_3(0.57)$ (b) $Ga_3(0.65)$ (c) $Ga_4(0.57)$ (d) $Ga_4(0.65)$

(e) $Ga_5(0.57)$ (f) $Ga_5(0.65)$ (g) $Ga_5(0.672)$ (h) $Ga_5(0.689)$

(i) $Ga_6(0.55)$ (j) $Ga_6(0.60)$ (k) $Ga_6(0.682)$ (l) $Ga_7(0.55)$

(m) $Ga_7(0.60)$ (n) $Ga_7(0.62)$ (o) $Ga_8(0.55)$

(p) $Ga_8(0.598)$ (q) $Ga_8(0.659)$

Figure 3.3: Electron localization function (ELF) isosurfaces for various gallium clusters at isosurface's value stated under brackets.

previous calculations [184, 174, 185]. Fig. 3.3 shows the ELF isosurfaces obtained from Gaussian for the gallium clusters having sizes between 3 to 8 atoms, with the ELF isosurface value within brackets. In Ga_3, the basins bifurcate and no attractor is observed on the radial axis joining the atoms as the isosurface value is increased. In Ga_4, at low isosurface value, the basins are connected. However, as the isosurface value is increased, the bifurcations bring out a different picture of attractors as also shown in Fig. 3.3(d). From Ga_5 to Ga_8, the basin bifurcation shows the presence of attractors between some of the participating atoms which are off-axis i.e. not present on the line joining the two atoms. Fig. 3.3(e)-(q) shows the changes in the ELF topology with changes in the isosurface value. The shape of the attractor observed after the bifurcation of the ELF is similar to either of the attractors between the Ga atoms obtained after the bifurcation of the triplet gallium dimer state $^3\Pi_u$. Since, the gallium dimer is covalently bonded with a similar ELF topology, these small gallium clusters should also be considered to have some covalent contribution from the ELF isosurface pictures obtained from Gaussian. However, the ELF isosurface pictures obtained from VASP for larger cluster sizes for which melting simulation have been performed do not show any attractor between the two participating Ga atoms [160].

Fig. 3.4 shows the ELF isosurfaces along with bifurcations for Ga_2, Ga_4, Ga_6 and Ga_8 clusters obtained from Gaussian. Pairing of gallium atoms is observed by the presence of an off-axis attractor when the separation between the atoms is less than 2.5 Å. This corresponds to some covalent character in the bonding of the paired atoms. However, there is no way one can assess 'how much' covalent character is present. These bonding patterns are clearly related to α-Ga, but without better knowledge of the electronic states of the individual components (for example presence of gallium dimer in Ga_4 and Ga_8) it is hard to make definitive conclusions.

We have demonstrated in this chapter that there can be significant differences in the topology of a 'bond'. Particularly for gallium clusters, this description should not be used to conclude the existence of a covalent bond as demonstrated by Kanhere and co-workers [175, 75, 17] as we have shown that the topologies obtained with different softwares are different.

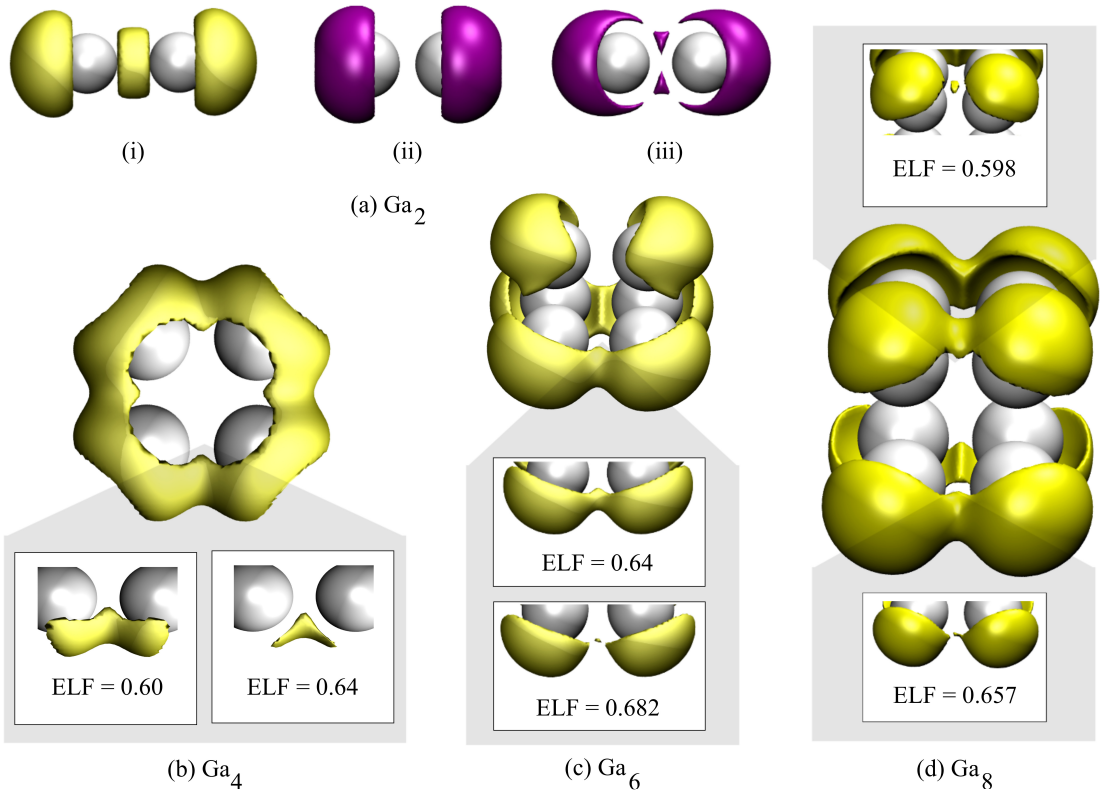

Figure 3.4: Electron localization function (ELF) isosurfaces for Ga_2, Ga_4, Ga_6 and Ga_8 at isosurface value 0.58. The inset images shows the bifurcations of the shaded (arrow) basin at specific ELF isosurface values. For Ga2, (i) shows the ELF images for the singlet and (ii), (iii) for the triplet gallium dimer with optimized bond distance of 2.45 A and 2.73 A respectively.

Chapter 4

Size effects in pure phases: Ga_{20}^+ and Al_{20}^+

Greater-than-bulk melting behaviour of Ga_{20}^+ clusters has been observed both experimentally and in theoretical calculations[186, 13]. Aluminium belongs to the same group as gallium in the periodic table (group 13) and has a similar ionisation potential. However, it has a vacant d-shell and is 5.4% smaller in atomic radius when compared to gallium. Moreover, experiments conducted on Al_{20}^+ clusters do not show a peak in the specific heat capacity plot[86]. Plausible explanations for this observation are that either the Al_{20}^+ cluster does not melt in the temperature window observed during experiments, or it melts over a range of temperatures. This chapter first briefly highlights the results of calculations performed by Steenbergen et al.[13] on Ga_{20}^+ cluster and then describes the results from the density functional theory (DFT) calculations performed on Al_{20}^+ cluster which is also seen to exhibit the *greater-than-bulk melting behaviour*. Moreover, like the Ga_{20}^+ cluster, there is a significant difference in the mobilities of the internal and surface atoms of the Al_{20}^+ cluster below the melting temperature. Atoms-in-molecules analysis brings out a picture of the monometallic clusters where there is strong charge segregation between the internal and the surface atoms; the internal atoms become negatively charged and the surface atoms become either, positively charged or stay neutral. This difference in the environments of the internal and surface atoms compared to the corresponding bulk phases suggests a physical picture of the origins of the *greater-than-bulk melting* behaviour.

4.1 Ga_{20}^{+} cluster

Steenbergen et al.[13] performed extensive DFT-based simulations on the melting of Ga_{20} and Ga_{20}^{+} cluster. They studied the role played by the inclusion and exclusion of *d*-electrons on the observed melting temperature by considering either the large core (i.e. $4s^2 4p^1$ as valence electrons) or small core (i.e. $3d^{10} 4s^2 4p^1$ as valence electrons) pseudopotentials. Molecular dynamics (MD) simulations in the microcanonical ensemble incorporating parallel tempering were carried for 92 ps (step size 2 fs) at 19 different temperatures. A summary of their results is as follows:

(a) Two distinct structures, stacked plane (SP) and capped sphere (CS), were observed for the 20 atom gallium cluster as shown in Fig. 4.1.

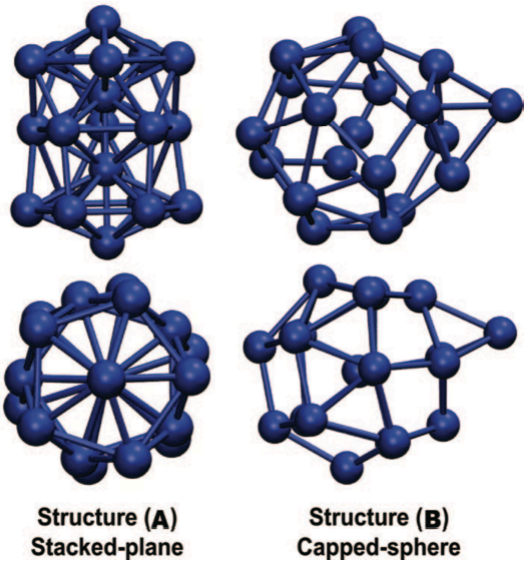

Figure 4.1: Stacked plane (A) and capped sphere (B) were the two distinct structures observed during the initial testing of 20 atom gallium clusters.

(b) The computed melting temperature was found to be independent of whether *d*-electrons were considered as core or valence electrons.

(c) The melting point of the neutral cluster was found to be greater than that of the charged cluster.

(d) Analysis of the electronic structure using Bader charges, ELF and spherical harmonics (SH) projected electronic density of states did not reveal any difference between the neutral and cationic cluster apart from the difference in the total number of electrons. Bader analysis showed segregation of charge

between the internal and surface sites, with internal sites getting strongly negatively charged and surface sites being neutral or getting strongly positively charged. Moreover, no signs of covalent bonding between the gallium atoms through ELF isosurfaces was claimed.

4.2 Computational details

Similar methodology was followed as used for Ga_{20}^{+} to simulate the melting transition in Al_{20}^{+} cluster. The global minimum structure of Ga_{20} cluster[187, 13] was used as the starting structure for Al_{20}^{+} cluster. This structure, named as stacked plane (SP) or 1-5-1-5-1-6-1 configuration, can be described as an assembly of alternate hexagonal and pentagonal planes separated by a single atom, the geometry optimised Al_{20}^{+} structure is shown in Fig. 4.2(a). For molecular dynamics, 29 different temperatures between 250 K to 1650 K at 50 K intervals were chosen to capture the melting transition in the microcanonical ensemble. The interest to observe the dynamics at higher temperatures was the reason behind the selection of the temperature range, which in experiments is up to 1060 K. Each microcanonical trajectory ran for 47.3 ps (step size 1 fs). A smaller step size (in comparison to the simulation of Ga_{20}^{+} cluster where the step size was 2 fs) helped to arrest the energy increase during the microcanonical simulations.

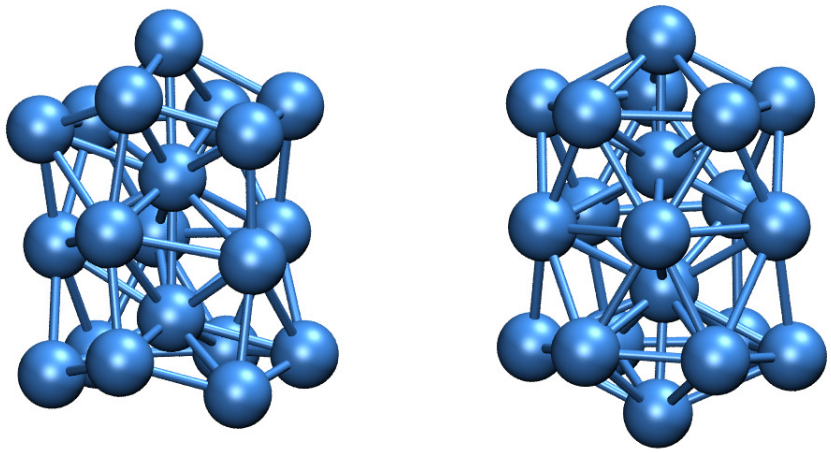

(a) Stacked plane (b) 1-5-1-5-1-6-1

Figure 4.2: Starting structure (a) and the global minimum structure (b) for Al_{20}^{+}. The binding energies for SP and 1-5-1-5-1-6-1 structure are -2.796 and -2.802 eV/atom respectively.

4.3 Thermodynamics

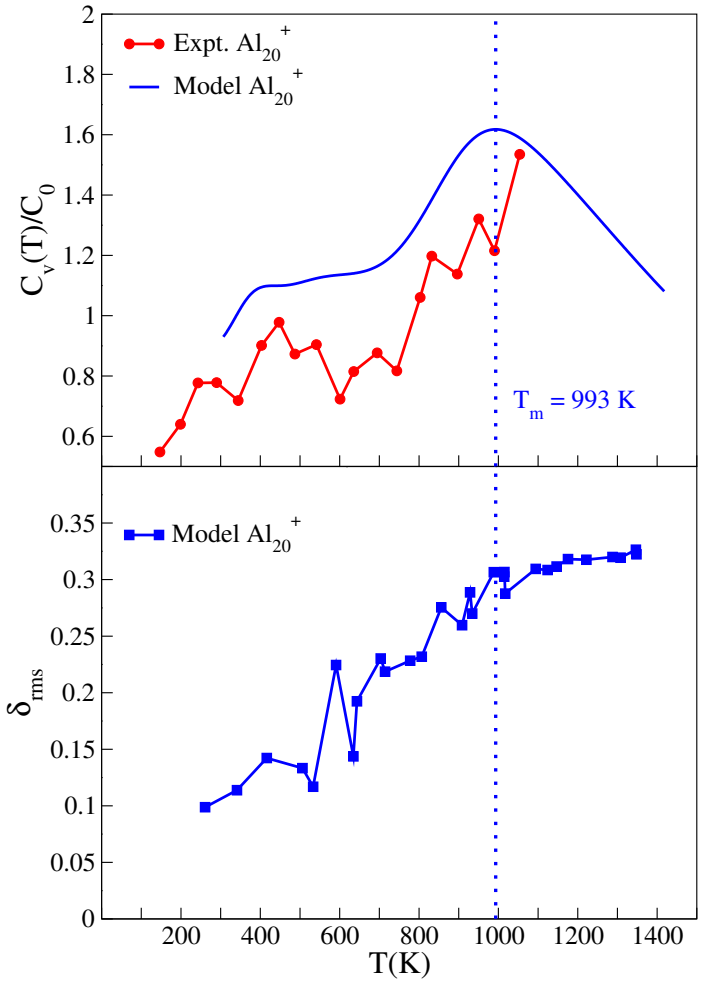

Figure 4.3: Comparison of the experimental and theoretical (multiple histogram method) canonical specific heat curves (top panel) and the corresponding root mean squared fluctuations in bond-length (bottom panel) of Al_{20}^{+} as a function of temperature.

The top panel of Fig 4.3 compares the canonical specific heat capacity plots obtained from the experiments and that calculated from the DFT based BOMD calculations. The canonical specific heat has been normalised to the classical specific heat which takes into account the rotational and vibrational degrees of freedom ($C_0 = (3N - 6 + 3/2)k_B$, where N is the number of atoms in the cluster and k_B is the Boltzmann's constant). The solid-liquid-like phase transition temperature, corresponding to the peak in Fig. 4.3, is 993 K which is higher than the bulk melting temperature of aluminium (933 °C)[188]. Although, DFT-based MD simulations has been able to capture the solid-liquid-like phase transition behaviour in different systems to a high degree of accuracy, the type of functionals used to perform DFT

calculations also affects the obtained melting temperatures. The expected accuracy is within 100 K, with a general shift observed towards higher temperatures using the PW-91 exchange correlation functional[189]. i.e. melting-like features may be observed for Al_{20}^{+} clusters at higher temperatures if explored in experiments. Chacko et al. performed Born-Oppenheimer MD calculations in the canonical ensemble using ultrasoft pseudopotentials within local density approximations on Ga_{13} and Ga_{17} clusters and reported the statistical uncertainty to be up to 15% in the position of the specific heat peaks[76].

4.4 Cluster geometry and structural dynamics

The bottom panel of Fig.4.3 shows the RMS bond-length fluctuations. Instead of exhibiting a sharp increase at the melting temperature, a characteristic of phase transitions in the bulk phase, the increase in δ_{rms} is smeared over a range of temperatures. However, the values converge above the calculated melting temperature (peak in specific heat) of 993 K, thus supporting the conclusion of a solid-liquid-like phase transition occurring in Al_{20}^{+} clusters. It must be noted that, though the actual values of δ_{rms} at low and high temperatures are consistent with parallel tempering (PT) independent simulations, they can be affected in the temperature range close to melting. Alternative measures such as the velocity autocorrelation function (VACF) and the corresponding power spectrum, unaffected by parallel tempering, have been used to confirm the phase transition in Al_{20}^{+} clusters as described in the following section.

The starting structures play a crucial role in the observed thermodynamics of the clusters. For example, the ordered* icosahedron and double icosahedron structures of Al_{13} and Al_{19} have been observed to melt exhibiting a very sharp specific heat peak among aluminium clusters between 11-20 atoms[190]. In situations (for example F-C Chuang et al.[191] found many different isomers for Al_{20} clusters) where several isomers compete to be the lowest energy structure at different energies, implementation of parallel tempering helps to enhance the ergodicity of the microcanonical simulations.

For Al_{20}^{+} clusters, though the SP (or 1-6-1-5-1-6) configuration was found to be the putative global minimum structure for Ga_{20} clusters and thus was used as the starting structure, another structure (referred to as 1-5-1-5-1-6-1, as shown in Fig. 4.2(b)) 6 meV lower in binding energy is also obtained. Chuang et al.[191] also found the same structure, similar to the Al_{19} double icosahedron but with an

*Terminology as used by Krishnamurty et al. in ref. [186].

embedded extra atom thereby giving it a prolate geometry. Thus, although the calculations did not start with the putative global minimum Al_{20}^{+} structure, it is found during the MD simulations highlighting the applicability of the computational approach.

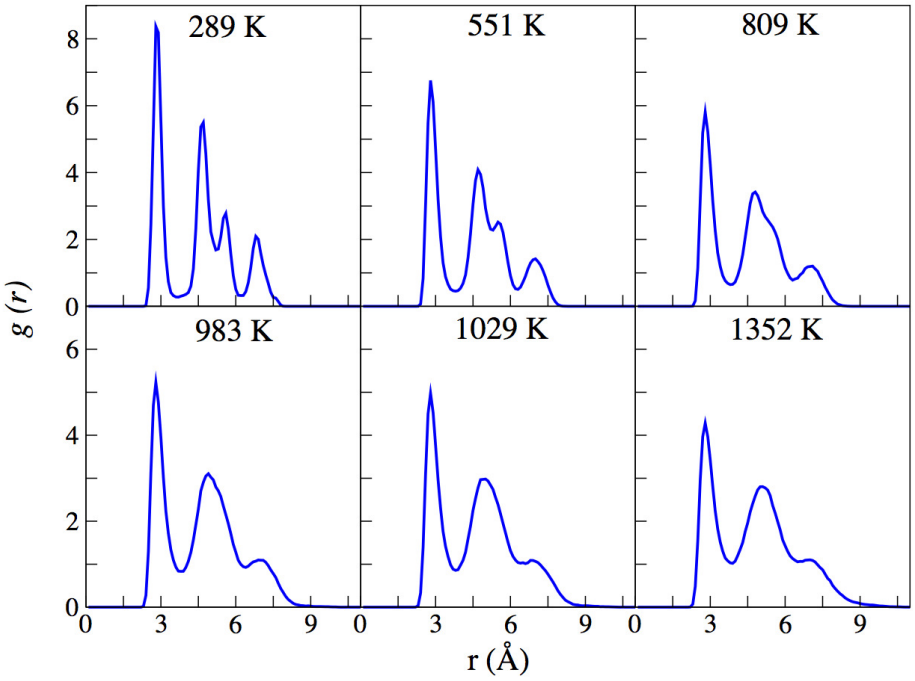

Figure 4.4: Changes in pair distribution function (PDF) of Al_{20}^{+} with average temperature during different microcanonical runs.

Fig. 4.4 shows the pair distribution function (PDF) obtained for the Al_{20}^{+} clusters for six different trajectories, with average temperatures as mentioned in each panel. At the lowest average temperature obtained in the simulations, 289 K, four distinct peaks are visible having the nearest neighbour distance of 2.8 Å. As the energy increases (reflected by the increase in the average temperatures) in the subsequent microcanonical runs, the second and third peaks start to merge and after 809 K, the PDF shows only three distinct peaks. This demonstrates the level of structural change one should expect upon going from a solid phase to a liquid phase in Al_{20}^{+} clusters.

4.5 Velocity auto-correlation function (VACF) and power spectrum

The velocity autocorrelation function plots for the lowest and highest energy simulations (289 K and 1352 K respectively) of Al_{20}^{+} clusters is shown in Fig. 4.5. Strong

correlations in atomic motion are observed at the lowest energy by the oscillatory behaviour of $C(t)$. However, at the highest energy correlations are not observed and the curve stays around zero. The VACF comparison at the lowest and the highest energies further shows that there is a solid-liquid-like phase transition occurring in Al_{20}^{+} clusters.

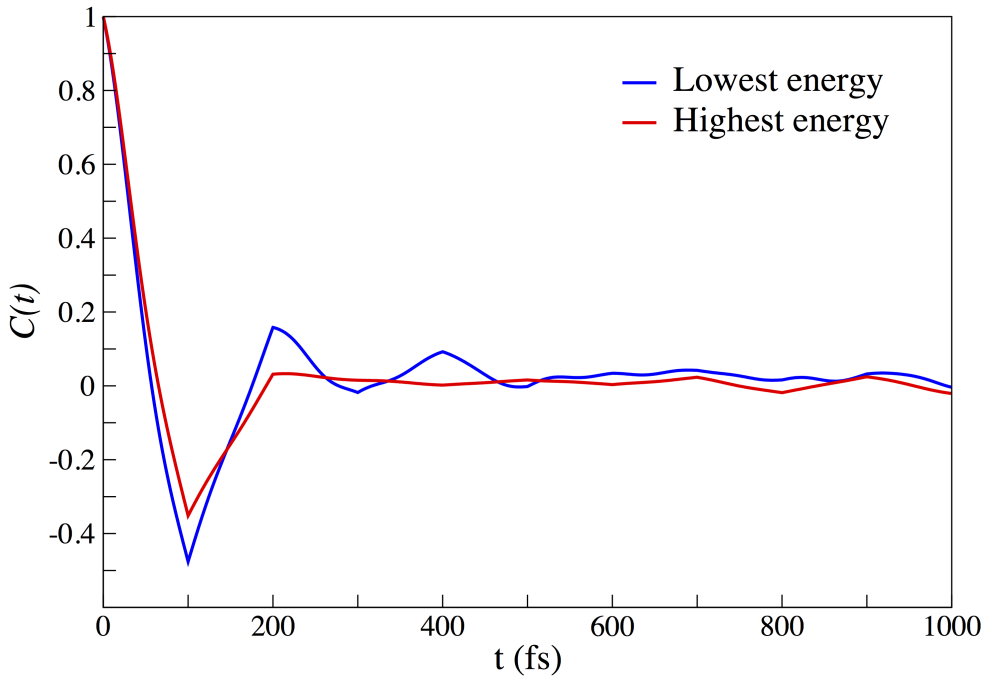

Figure 4.5: Velocity auto-correlation function of all atoms of Al_{20}^{+} cluster averaged at the lowest (blue) and highest energy (red) as a function of time.

Shown in Fig. 4.6 are the power spectra obtained for Al_{20}^{+} clusters at five different energies (average temperatures mentioned in each panel). The two internal sites are coloured red and blue and the surface atoms have been averaged (black). With increasing temperatures, the high frequencies of the two internal Al atoms start to merge with that of the surface atoms and a transition from a near-overlap to a complete overlap between 983 K and 1023 K is observed. The canonical specific heat peak, at 993 K, agrees well with the power spectra behaviour.

All the statistical tools utilised above confirm that there indeed is a solid-liquid-like phase transition occurring in Al_{20}^{+} clusters and that it can be consistently assigned to the temperature of the peak in the specific heat curve. The next step is to investigate the cause behind the *greater-than-bulk melting* behaviour in Al_{20}^{+} and Ga_{20}^{+} clusters. Although, the existence of covalent bonding between the Ga atoms has been put forth as the reason behind the *greater-than-bulk melting* behaviour of gallium clusters[76], these signatures of covalency seem to be an over

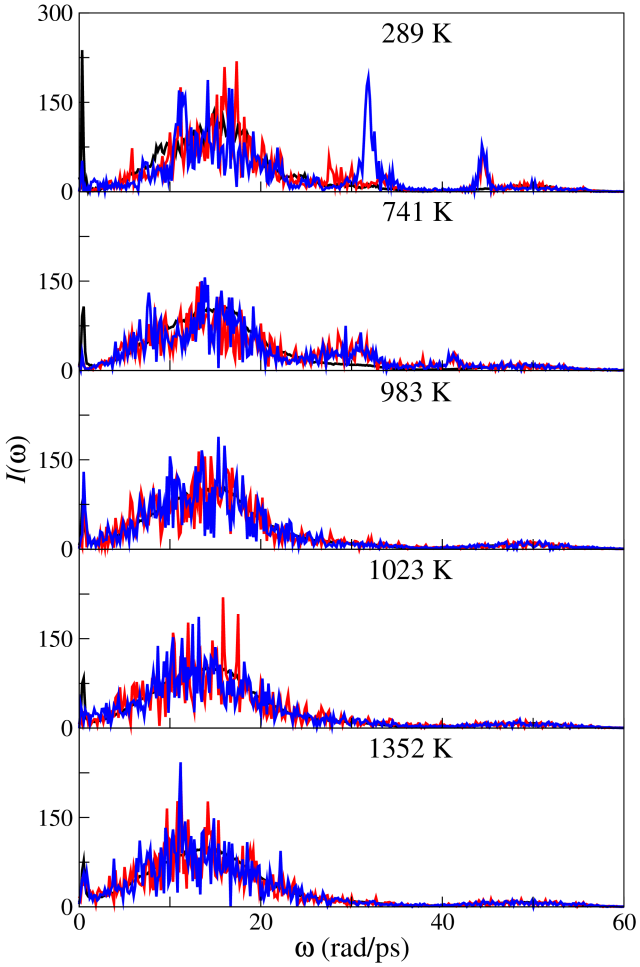

Figure 4.6: The power spectrum of the two internal atoms (blue and red) along with that averaged for all the surface atoms (black) of Al_{20}^+ cluster as a function of frequency.

interpretation of the electron localisation function (ELF). Using atoms-in-molecules analysis and various other statistical indices an attempt is made to understand the changes occurring in Al_{20}^+ clusters over time and with increasing energies (average temperatures).

4.6 Atoms-in-molecules analysis

Fig. 4.7 shows the partial charges obtained for the SP and the putative global minimum geometry (1-5-1-5-1-6-1) of Al_{20}^+ clusters. Strong charge segregation between the internal and surface Al atoms is observed, with internal atoms getting strongly negatively charged and the surface atoms either getting strongly positively charged or staying neutral. Moreover, with time, the overall charge distribution adjusts with the motion of atoms to maintain this picture in the cluster. A similar charge distri-

bution picture was obtained for the Ga_{20}^{+} cluster in its putative global minimum SP configuration. However it was only the internal and the capping atom that became strongly negatively and positively charged respectively, with the other surface atoms remaining neutral, in the CS geometry[13].

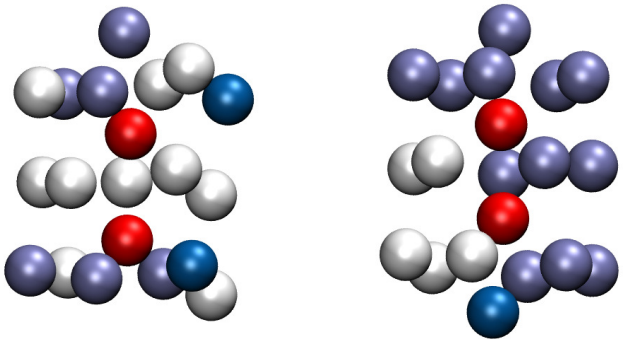

(a) Stacked plane (b) 1-5-1-5-1-6-1

Figure 4.7: Partial charges (q) obtained by atoms in molecules (AIM) analysis for Al_{20}^{+} clusters: (red) q $\leq$ -0.2e ; (pink) -0.2e $<$ q $\leq$ -0.1e ; (white) -0.1e $<$ q $\leq$ 0.1e ; (ice blue) 0.1e $<$ q $\leq$ 0.2e ; (dark blue) q $>$ 0.2e.

4.7 Mean squared displacement, average coordination number and diffusion coefficient

To study the effects of charge segregation on the relative mobilities of the internal and surface atoms, the mean squared displacements (MSD), average coordination numbers and the diffusion coefficients are used. Fig. 4.8 compares the MSDs of the surface atoms (averaged) for Al_{20}^{+} and Ga_{20}^{+} clusters at the lowest and the highest simulation energies. Relatively similar mobilities are observed for the surface atoms at both the energies in both clusters indicating that the increasing energy has a very small effect on the mobilities of the surface atoms.

The structural changes occurring in Al_{20}^{+} cluster is discerned using the average coordination number of each participating atom. Fig. 4.9(a) shows the average coordination number, calculated using the first minimum in $g(r)$ as cutoff radius, of the selected Al_{20}^{+} atoms as coloured in inset. Three distinct coordination sites at low temperatures are observed: internal atoms (black and red respectively), surface atoms located in the central ring (coloured blue) and the surface atoms located at the top and bottom ring (coloured green and violet respectively). However, after the calculated melting temperature, all the atoms end up having similar coordination numbers on average. On the other hand, only two distinct sites are observed up to

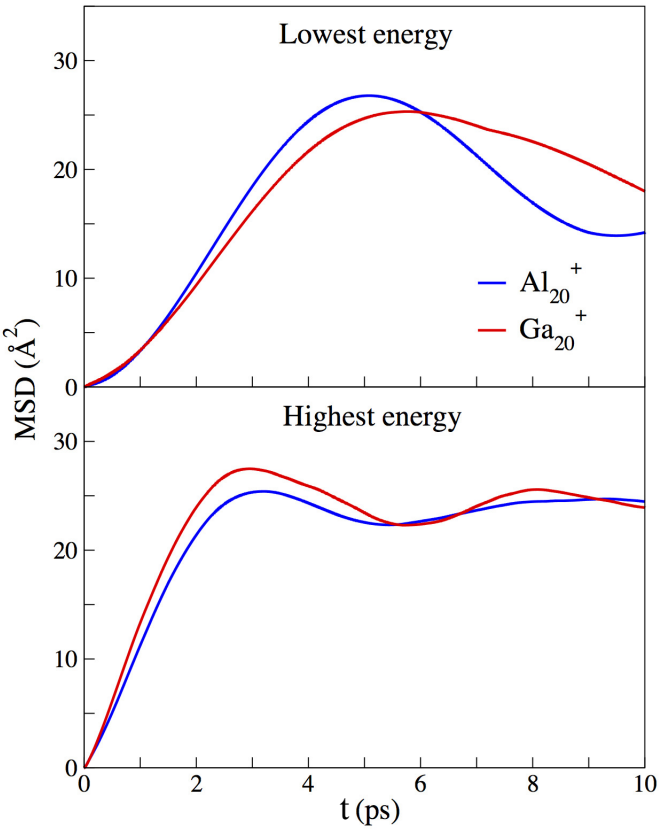

Figure 4.8: MSD comparison of the surface sites at the lowest and highest simulation energy for Al_{20}^+ (shown in blue) and Ga_{20}^+ (shown in red) respectively.

700 K, viz. the central site (red) and three representative surface atoms (coloured green, blue and violet) showing changes in the average coordination number of the surface atoms, for Ga_{20}^+ clusters (where the melting temperature was found to be 616 K) as shown in Fig. 4.9(b).

Thus far, the differences in the environments of the internal and surface atoms in these clusters have been convincingly demonstrated, and hence the internal atoms cannot be considered to be an intermediate between the bulk and surface atoms. The self-diffusion coefficient helps to probe this difference further by analysing the motion of the internal and surface atoms below and above the melting temperatures in Al_{20}^+ and Ga_{20}^+ clusters. However, in order to 'define' an internal atom at temperatures just below the melting temperature in Al_{20}^+ cluster, the *'persistent internal'* atom criterion was formulated according to which an atom is internal if (a) it has an average coordination number greater-than-or-equal-to 9.5, and (b) the time during which condition (a) is satisfied (in each MD run) is more than 1.5 ps. The need for the criteria arose because, as seen from Fig. 4.9, at 924 K, i.e. below

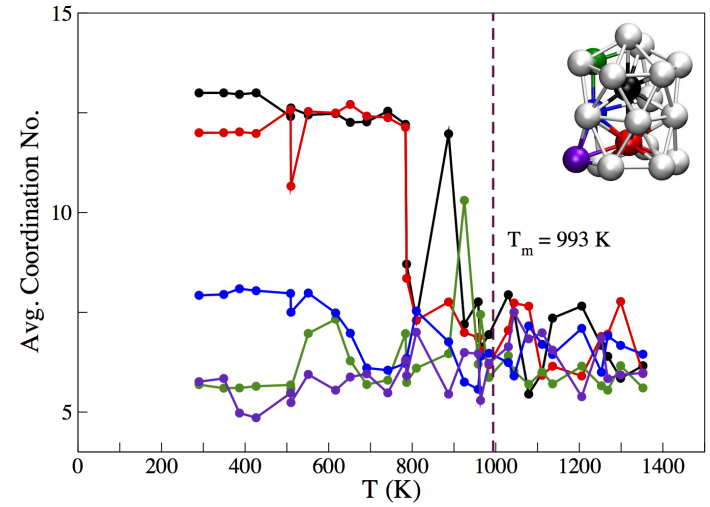

(a) Al_{20}^{+}

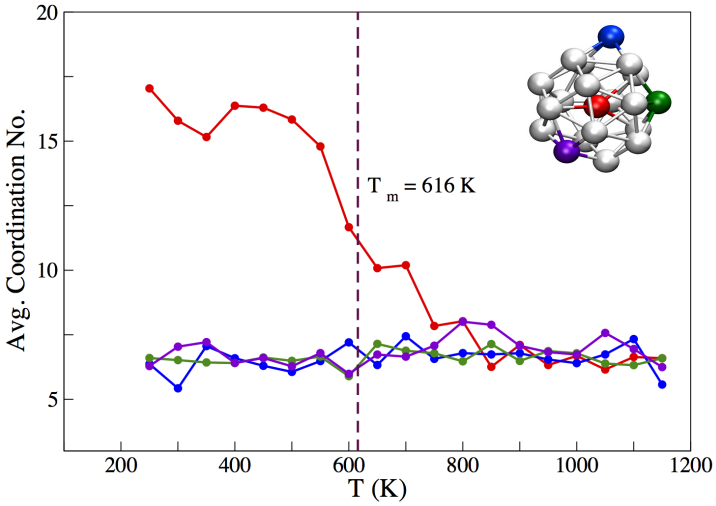

(b) Ga_{20}^{+}

Figure 4.9: (a) Average coordination number variations with temperature for aluminium atoms at positions shown in inset. (b) Average coordination number variations with temperature for gallium atoms in the capped sphere (CS) configuration of Ga_{20}^{+} cluster for atoms at positions shown in inset.

the melting temperature, the atom coloured green in the top ring has an average coordination number of an internal site in comparison to the atom (coloured red) that was occupying the internal site at low temperatures thus reflecting an exchange of the atoms. This makes it much harder to identify and tag a particular atom as internal, near the melting temperature.

The top and bottom panel of Fig. 4.10 shows the self-diffusion coefficient calculated for Al_{20}^{+} and Ga_{20}^{+} clusters respectively. The MSD values over which the self-diffusion coefficient value is calculated have been kept fixed between 1 and 2 Å^2. The surface atoms of both, Al_{20}^{+} and Ga_{20}^{+}, clusters exhibit very high self-diffusion

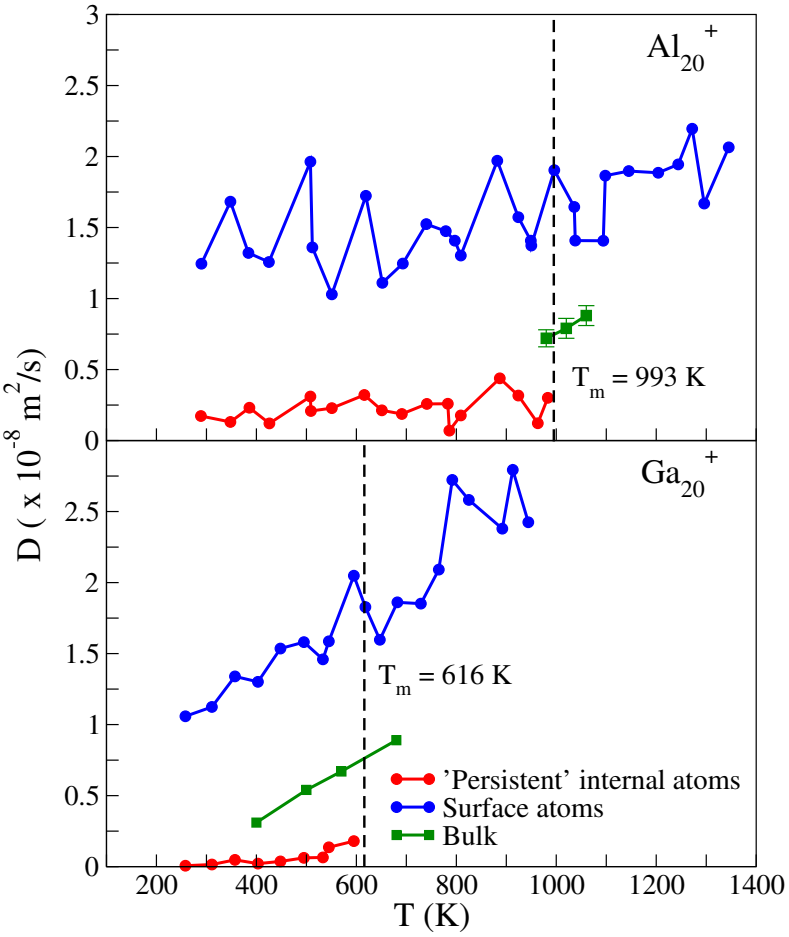

Figure 4.10: Comparison of self diffusion coefficient of internal and surface atoms Al_{20}^+ (top panel) and Ga_{20}^+ (bottom panel) along with the corresponding value in the bulk liquid phase of aluminium[192] and gallium[193] as a function of temperature.

coefficient values. In comparison, the values for the *'persistent internal'* atoms are very low until the respective melting temperatures is achieved. After the melting temperatures, none of the 20 atoms satisfied the *'persistent internal'* criteria. Individual atom self-diffusion coefficients have nearly the same values above the melting temperature reflecting a *liquid-like* phase.

The self-diffusion coefficient clearly demonstrates that it is the internal atoms whose movements correspond to the melting-like feature observed in Al_{20}^+ and Ga_{20}^+ clusters. Strong charge segregation between the internal and surface atoms reflects the electrostatic nature of the interaction between them, thereby, bringing out a picture where the internal atoms have been confined in an electrostatic cage - a step useful in describing why *greater-than-bulk melting* occurs at these cluster sizes.

Thus far we have established that the pure components of our nanoalloy sys-

tem $Ga_{(20-x)}Al_x^+$, i.e. Ga_{20}^+ and Al_{20}^+, melt above their corresponding bulk phase melting temperatures. However, the increase in the melting temperature of Ga_{20}^+ cluster is much higher (313 K) compared to that in Al_{20}^+ cluster (only 60 K). How the number of Al atoms, from 1 to 11 and finally to 17, affects the cluster structure, the thermodynamics and whether there is a similar *greater-than-bulk melting* behaviour or not in the 20 atom gallium aluminium alloy is the subject matter of the study presented in the next chapter.

Chapter 5

Mixed Phases: $Ga_{19}Al^+$, $Ga_{11}Al_9^+$ and $Ga_3Al_{17}^+$

The similarities and differences between Al_{20}^+ and Ga_{20}^+ pose the question as to how the thermodynamics of mixed Ga-Al nanoalloys change with composition. Shown in Fig. 5.1 is the calculated energy of mixing for the $Ga_{(20-x)}Al_x^+$ system. A negative value indicates that mixing is energetically favourable relative to the monoatomic clusters as expressed by

$$E_{exc} = E_{tot}^{Ga_{(20-x)}Al_x^+} - \frac{x}{20}E_{tot}^{Al_{20}^+} - \frac{20-x}{20}E_{tot}^{Ga_{20}^+}. \tag{5.1}$$

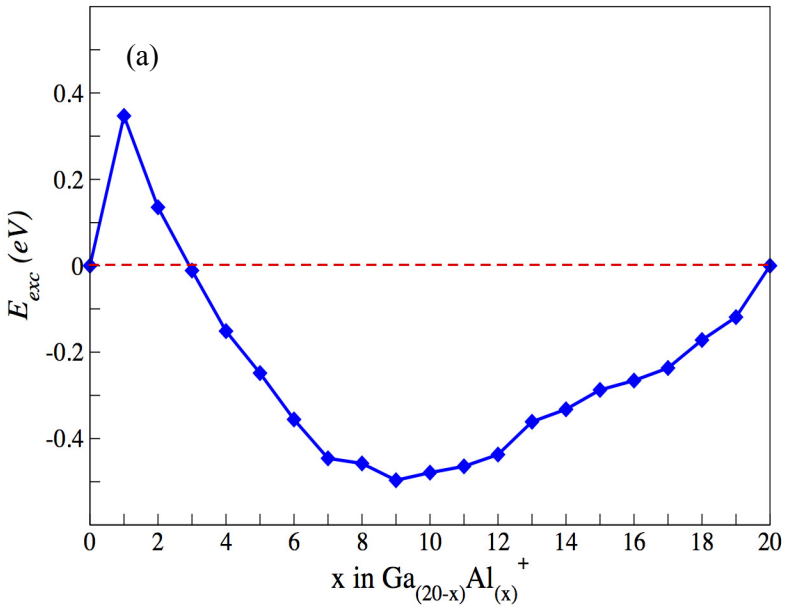

Figure 5.1: Excess energy for all the compositions in $Ga_{(20-x)}Al_x^+$.

As detailed in section 5.1.1, the stacked plane (SP) configuration had lower energy in contrast to the capped sphere (CS) configuration when one of the gallium atoms of Ga_{20}^{+} was replaced by an Al atom. Thereafter each of the 20 available sites in the SP configuration were substituted by an Al atom and the obtained free energies for each $Ga_{19}Al^{+}$ cluster were arranged in ascending order. To obtain the starting structure for a particular $Ga_{(20-x)}Al_x^{+}$ cluster, the first 'x' sites of the free energy ascending order was substituted with Al atoms.

As observed from Fig. 5.1 that the addition of an aluminium atom to the Ga_{20}^{+} cluster gives a positive value to the energy of mixing thereby indicating segregation occurring in the gallium dominated $Ga_{19}Al^{+}$. The energy of mixing remains positive for $Ga_{18}Al_2^{+}$ and starts to have negative values from $Ga_{17}Al_3^{+}$ onwards indicating mixing of the gallium and aluminium atoms. It achieves the minimum value at the most favourable composition, i.e. $Ga_{11}Al_9^{+}$. To investigate the solid-liquid-like phase transition and the underlying dynamics exhibited below and above the melting temperatures $Ga_{19}Al^{+}$, $Ga_{11}Al_9^{+}$ and $Ga_3Al_{17}^{+}$ were chosen as the representative clusters in the $Ga_{(20-x)}Al_x^{+}$ cluster series. The following sections describe the results from the DFT based BOMD calculations.

5.1 $Ga_{19}Al^{+}$

Neal et al.[194] found a similar melting behaviour of both $Ga_{(n-1)}Al^{+}$ and Ga_n^{+} clusters during experiments. Furthermore, to interpret the results two significant assumptions were made:

1. The substitution of an aluminium atom did not cause a substantial change in the overall geometry of the gallium cluster.

2. The decrease in entropy during the solid-liquid-like phase transition of $Ga_{(n-1)}Al^{+}$ in comparison to Ga_n^{+} was due to the Al occupying a surface site. This was substantiated by the calculations of relative energy of the surface and central sites of $Ga_{12}Al^{+}$ and $Ga_{12}Al^{-}$ in the icosahedral geometry.

The DFT calculations, to understand the phase transition in the $Ga_{19}Al^{+}$ cluster and thereafter comparing it with the results from the corresponding calculations[13] performed on the Ga_{20}^{+} cluster, provides a sensitive first principles treatment to not only test these assumptions, but also to understand the changes in the electronic structure* of gallium clusters, known to have a rich potential energy landscape,

*The *4s* band of Ga is shifted to a higher binding energy in comparison to the *3s* band of Al atom and hence, the overlap of the valence s and p orbitals is different for both metals[195].

brought about with the introduction of an aluminium atom.

5.1.1 Cluster Structure

As already mentioned in the previous chapter, two different structural classes[13] were observed for Ga_{20}^{+} cluster: (i) a stacked plane (SP) configuration where an assembly of alternating hexagonal and pentagonal planes are separated by a single atom, and (ii) a capped sphere (CS) where a central atom is surrounded by a near-spherical shell of atoms with a protruding asymmetric tetragonal cap. To obtain the ground state structure for $Ga_{19}Al^{+}$, each of the 20 available sites in both the structural classes was replaced by an Al atom. Fig. 5.2 compares the obtained binding energies per atom for $Ga_{19}Al^{+}$ in both the structural classes as a function of the distance of the Al atom from the centre of mass (COM) of that particular structure.

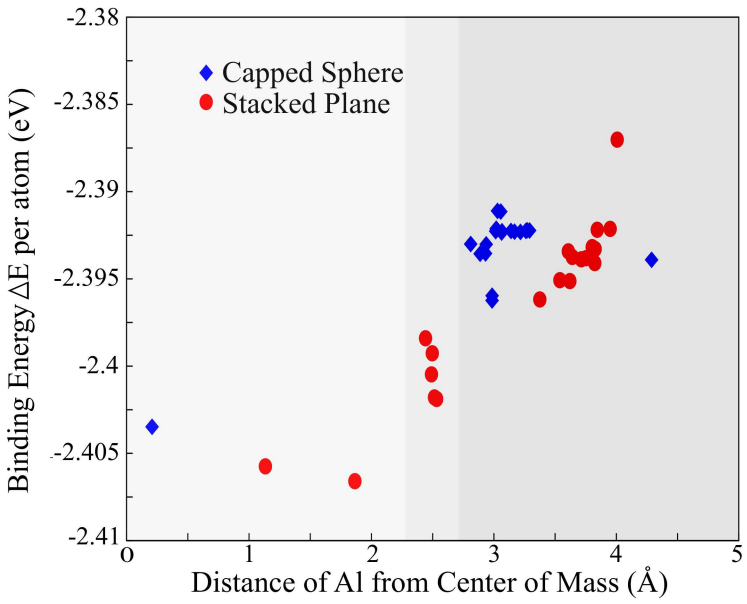

Figure 5.2: Binding energies (per atom) of $Ga_{19}Al^{+}$ clusters with the Al atom located at different sites, shown by their distance from the centre of mass of the cluster. Both the stacked-plane (SP) and the capped-sphere (CS) structures are considered.

A clear preference for the internal site (one in CS, two in SP) to be occupied by the Al atom is observed in Fig. 5.2. The middle ring having five sites in the SP configuration (darker shaded region) is the next preferred site being intermediate in nature between the internal and surface sites. The surface sites, beyond 2.7 Å,

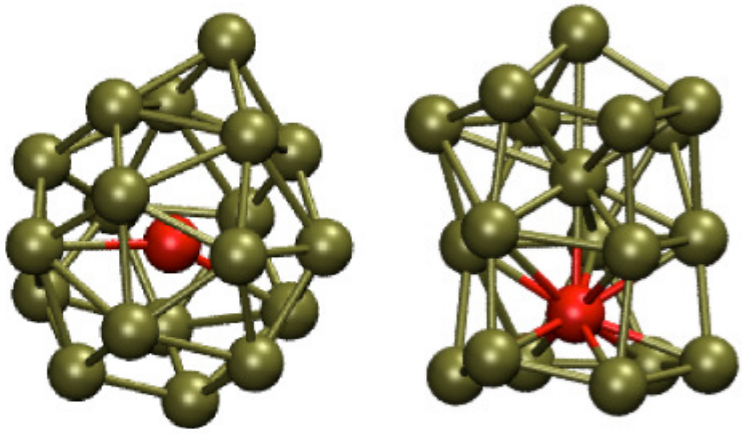

(a) Capped Sphere (CS) (b) Stacked Plane (SP)

Figure 5.3: Lowest energy structures of $Ga_{19}Al^+$ in both capped sphere and stacked plane geometries with binding energy values of -2.402, and -2.407 eV respectively. The Al atom is in red and Ga atoms in tan.

are least favourable in both the structural classes. The smaller size of the Al atom allows for greater structural relaxation when present at an internal site thereby favouring it compared to the surface. The lowest energy structure obtained in both the structural classes is shown in Fig. 5.3.

Bader charges

The presence of an Al atom in the $Ga_{19}Al^+$ cluster has a subtle effect on the structure, as both the isomers observed in $Ga_{20}{}^+$ cluster (SP and CS) have similar binding energies when the $Ga_{19}Al^+$ configurations, shown in Fig. 5.3, are compared. However, in contrast to $Ga_{20}{}^+$ where both the internal atoms in the SP configuration became negatively charged, the internal Al atom becomes strongly positively charged ($+0.36e$) and the internal Ga atom becomes strongly negatively charged($-0.46e$), thus forming a dipole, in the $Ga_{19}Al^+$ cluster. The negative charging of the internal atoms in pure gallium clusters[13] could be due to the presence of large volume of delocalised electrons at the centre of cluster. However, this does not explain the positive charge on Al atom in $Ga_{19}Al^+$ cluster. Aluminium has a slightly lower ionisation potential (IP) than gallium, by 13 meV. The effect of such a small difference being the formation of a dipole is an interesting effect. *Bader charges* calculated for the SP and CS configurations with the Al atom situated at both the internal and surface sites reveals that Al always becomes positively charged irrespective of the site occupied by it. In the CS configuration, the Al atoms occupying the internal site becomes positively charged and the capping Ga atom becomes negatively

charged while the other surface Ga atoms remain neutral. When Al occupies a surface site, in either configuration, charge segregation occurs with internal atoms becoming negatively charged and surface sites atoms becoming positively charged.

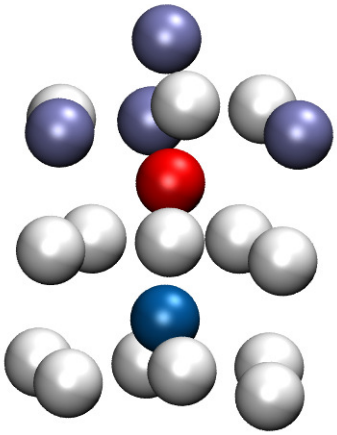

Figure 5.4: Bader analysis for the lowest energy ground state $Ga_{19}Al^+$ structure. In the order of strongly negative to strongly positive, with partial charge: (red) q $\leq$ -0.2e ; (pink) -0.2e $<$ q $\leq$ -0.1e ; (white) -0.1e $<$ q $\leq$ 0.1e ; (ice blue) 0.1e $<$ q $\leq$ 0.2e ; (dark blue) q $>$ 0.2e.

MD calculation details

Taking the lowest energy $Ga_{19}Al^+$ structure in the stacked plane configuration (Fig. 5.3(b)) to be the putative global minimum, first principles Born-Oppenheimer molecular dynamics (MD) calculation were performed in the microcanonical ensemble at 19 different temperatures between 250 K and 1150 K at every 50 K interval. MD was performed for 58 ps (step size 2 fs) after equilibration to obtain the statistics for analysis as described in the next few subsections.

5.1.2 Thermodynamics

Shown in top panel of Fig. 5.5 are the calculated and experimental[196] specific heat curves for $Ga_{20}{}^+$ and $Ga_{19}Al^+$ clusters. The canonical specific heat curves have been normalised to the classical specific heat which takes into account the rotational and vibrational degrees of freedom ($C_0 = (3N - 6 + 3/2)k_B$) of the system. The solid-liquid-like melting transition in $Ga_{19}Al^+$ cluster has been captured in excellent agreement with experiment. The melting temperature calculated for $Ga_{19}Al^+$, corresponding to the peak in specific heat curve, is 686 K which is 70 K higher than $Ga_{20}{}^+$. The introduction of Al thus causes an increase in the melting temperature of the gallium dominated cluster. Although experimental results confirm the increase

in melting temperature, the increase in the magnitude of melting temperature is only 43 K (Ga_{20}^+ at 705 K and $Ga_{19}Al^+$ at 748 K). The larger difference between the calculated melting temperatures of Ga_{20}^+ and $Ga_{19}Al^+$ is attributed to the accuracy of the functionals used during the calculation. Compared to the bulk Ga-Al alloy[95] with 95 at. % Ga and 5 at. % Al having a melting temperature of 354 K, the *greater-than-bulk melting* behaviour is also observed in the $Ga_{19}Al^+$ nanoalloy as well.

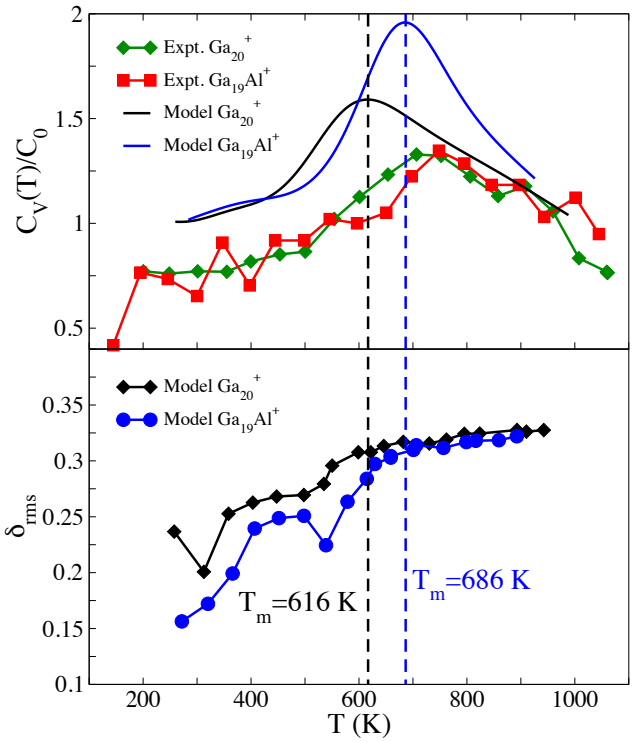

Figure 5.5: Comparison of canonical specific heat curves and root mean squared displacement in bond lengths for Ga_{20}^+ and $Ga_{19}Al^+$ as a function of temperature.

5.1.3 Structural dynamics: Lindemann index, pair distribution function (PDF), mean squared displacement and average coordination number

The bottom panel of Fig. 5.5 shows the Lindemann index calculated for $Ga_{19}Al^+$ and compared to that for Ga_{20}^+ clusters. The δ_{rms} values have been smeared over a range of temperatures as opposed to having a sharp increase at the phase transition temperature. However, the values converge above the calculated melting temperature of 686 K for $Ga_{19}Al^+$.

Fig. 5.6 shows a comparison of the time-averaged pair distribution functions

of $Ga_{19}Al^+$ (red) and Ga_{20}^+ (black). At the lowest energy the differences in the structures of $Ga_{19}Al^+$ (stacked plane) and Ga_{20}^+ (capped sphere) can be easily observed by the different positions of the peaks. With increasing energies (average temperatures), the PDFs of the clusters start to show changes, and prior to the melting temperature of Ga_{20}^+ (616 K) cluster, the third peak in the PDF vanishes. This feature, however, is not seen for $Ga_{19}Al^+$. Moreover, the overlap of PDFs of $Ga_{19}Al^+$ and Ga_{20}^+ at the highest energy indicates the indistinguishability of both the cluster structures in the *liquid-like* state.

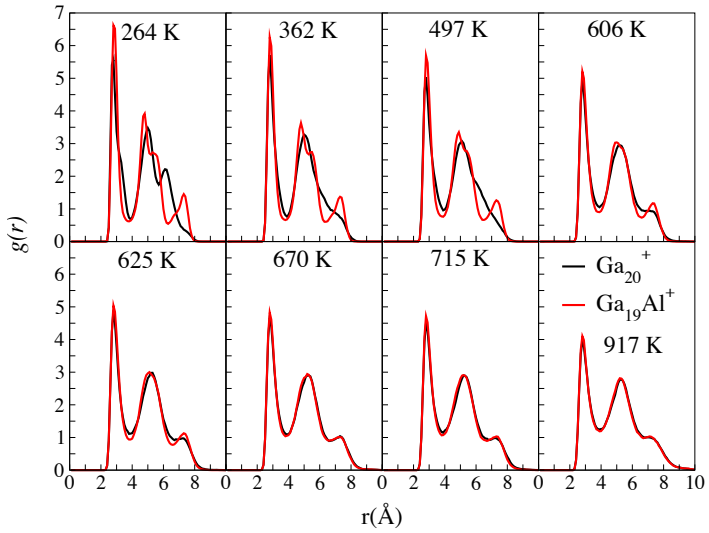

Figure 5.6: Comparison of pair distribution function of Ga_{20}^+ (black) and $Ga_{19}Al^+$ (red) at various energies (the corresponding average temperature is given.)

The mean squared displacement helps to compare the mobilities of the internal and the surface atoms in both, Ga_{20}^+ and $Ga_{19}Al^+$, clusters. Fig. 5.7 shows that the central gallium atom in the Ga_{20}^+ CS structure is largely immobile compared to the surface atoms at the lowest energy but has a mobility comparable to them at the highest simulated energy corresponding to a *liquid-like* state. In contrast, the central Ga and Al atoms in $Ga_{19}Al^+$ are largely immobile in comparison to the surface Ga atoms at the lowest energy, the mobility of the central Ga atom is similar to that of the surface atoms at the highest energy.

Fig. 5.8 compares the MSDs of the central Ga and Al atom in $Ga_{19}Al^+$ cluster at various energies. At the lowest temperature a correlated motion is seen between the atoms which is lost with increasing temperatures as the central Ga atom acquires a larger relative motion in comparison to the central Al atom. Moreover, the maximum value attained by the MSD of the central Al atom hovers around 10 $Å^2$ after 658 K, being unaffected by the increase in energy. This difference in mobility between the central Ga and Al atoms in the *liquid-like* state indicates that probably the internal

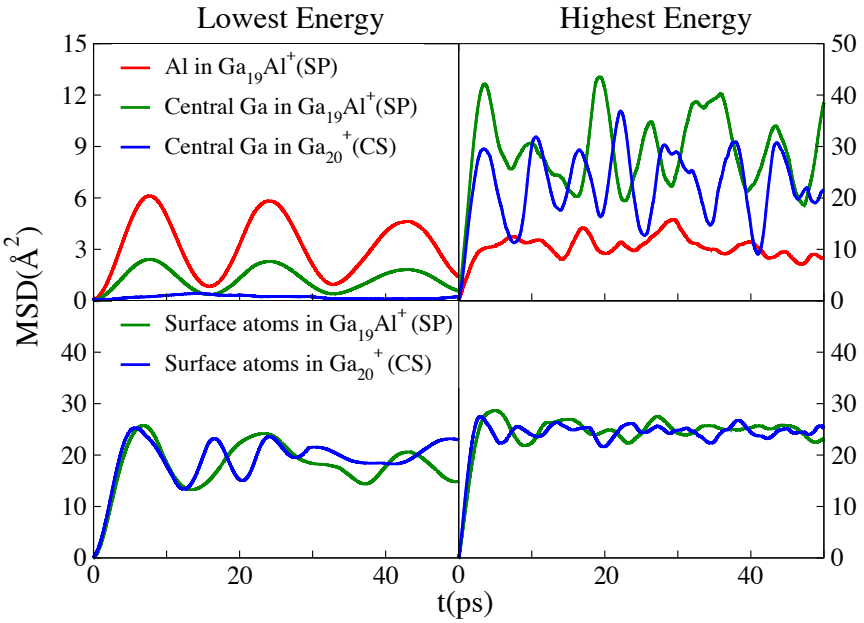

Figure 5.7: MSD comparison of central and surface atoms of stacked plane (SP) and capped sphere (CS) geometries at lowest and highest energies.

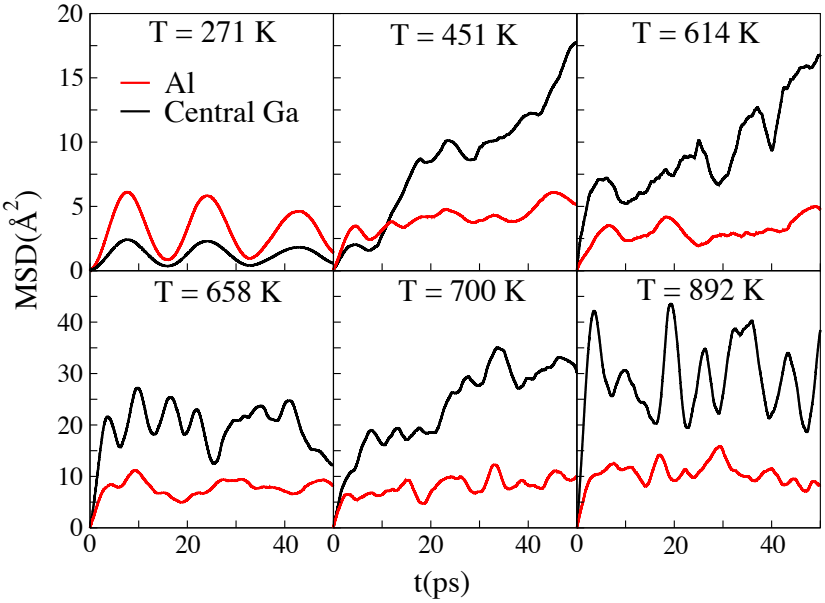

Figure 5.8: MSD of aluminium (red) and central gallium (black) atom of stacked plane $Ga_{19}Al^{+}$ geometry at various temperatures. Note that the label 'Central Ga' applies to the position of this atom in the original ground state, and ceases to be correct at high temperatures.

Ga atom moves to the surface and the Al atom prefers to occupy the internal site even after the cluster has *melted*.

The average coordination number, as shown in Fig. 5.9 for few representative

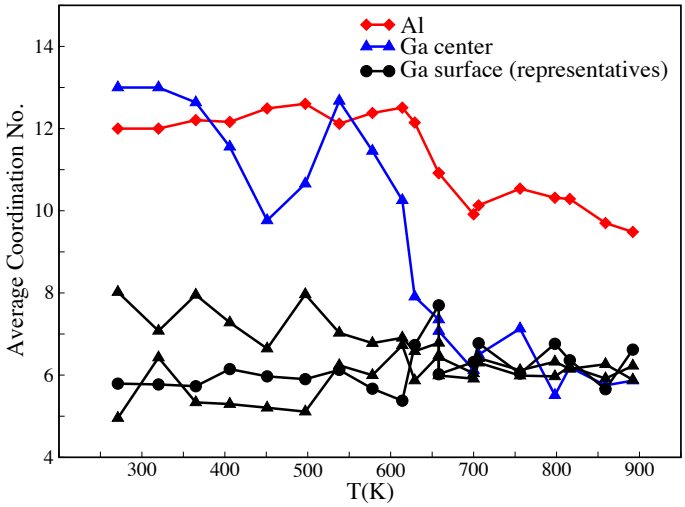

Figure 5.9: Variations in average coordination number of central Ga atom (blue), aluminum atom (red) and 3 representative surface atoms (black) of $Ga_{19}Al^{+}$ with temperature.

atoms of $Ga_{19}Al^{+}$ cluster, provides further evidence in support of the claim that the aluminium atom in $Ga_{19}Al^{+}$ cluster prefers to occupy the internal site in both, *solid-like* and *liquid-like*, phases. The cutoff distance for an atom to be considered as a neighbour in this calculation is 3.8 Å as observed from the position of first minimum in $g(r)$ at the lowest energy as shown in Fig. 5.6. The central Ga atom has a coordination number of 13 (icosahedron-like) and the Al atom 12 at the lowest energy. With increasing temperatures, changes in the average coordination of both the internal atoms is seen and prior to the melting temperature of 686 K, the central Ga atom has a coordination number similar to those of the surface atoms. However, even after the melting temperature, the Al atom still has 9 neighbouring atoms on average i.e. similar to a bulk-like environment.

5.1.4 Velocity autocorrelation function (VACF) and power spectrum

Fig. 5.10 shows the velocity autocorrelation function (VACF) and the corresponding power spectrum for $Ga_{20}{}^{+}$(left) and $Ga_{19}Al^{+}$(right) clusters respectively. To identify the phase transitions from the VACFs and the power spectrum, Yen et al.[167] set forth the criteria that the temperature at which the power spectrum $I(\omega)$ of the central atom overlaps (dissolves) into that of the surface atoms and also the low frequency ω of all individual atoms becomes indistinguishable is the phase transition temperature. For $Ga_{20}{}^{+}$, the overlap between the power spectra of the central (blue) and the surface atoms (averaged as black) goes from a near-overlap to a complete one

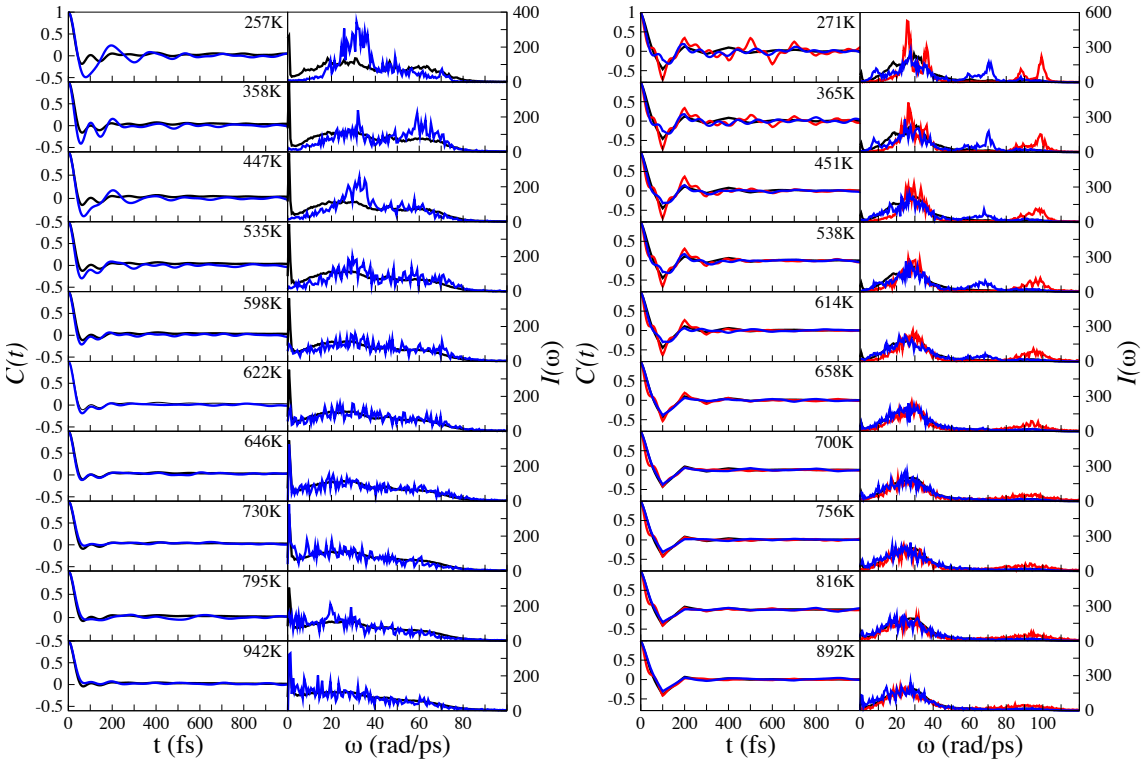

Figure 5.10: The Velocity auto-correlation function (VACF, left columns) and the corresponding power spectrum $I(\omega)$(right columns) is shown for Ga_{20}^{+}(left) and $Ga_{19}Al^{+}$(right). The central Ga atom is coloured blue, the surface Ga atoms in black; and the Al atom in $Ga_{19}Al^{+}$ is red. The average temperature during the simulation run is stated.

between 598 K and 622 K. The melting temperature as obtained from the specific heat capacity peaks being 616 K corroborates further that there indeed is a phase transition occurring in these systems.

In $Ga_{19}Al^{+}$, with increasing temperatures the peak present at the lowest energy at 70 rad/ps for the central Ga atom dissolves into that for the surface atoms (black) prior to the melting temperature of 686 K. A similar behaviour was also observed in its average coordination number indicating that it becomes a surface atom prior to the melting temperature. Also, the power spectra of the internal Ga atom in Ga_{20}^{+} and $Ga_{19}Al^{+}$ clusters can be easily differentiated. This difference can be the result of a different putative global minimum geometries assumed by both the clusters. Furthermore, using the criterion that there has to a complete overlap of the power spectra of the central Ga, Al and the surface atoms, the melting temperature should be near 700 K (the peak in the specific heat capacity being at 686 K). Thus there is a clear transition occurring in these systems from a *solid-like* state to a *liquid-like* state. In contrast to the observations for central Ga atom, the high-frequency vibrations do not disappear quickly for the Al atom in $Ga_{19}Al^{+}$ cluster indicating

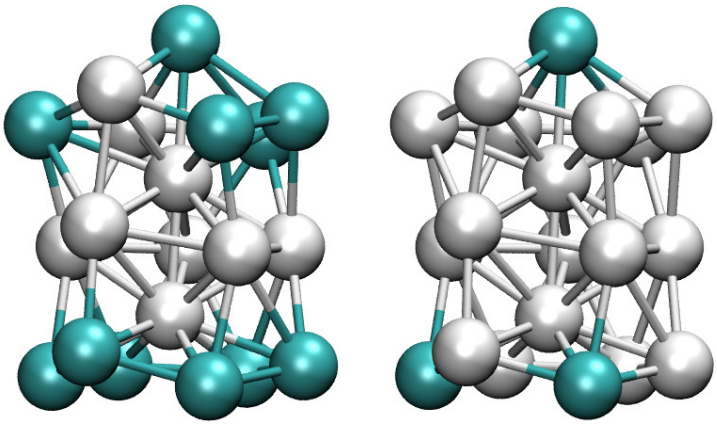

(a) $Ga_{11}Al_9^+$ (b) $Ga_3Al_{17}^+$

Figure 5.11: Starting structures in the stacked plane ($Ga_{11}Al_9^+$ and $Ga_3Al_{17}^+$) configurations with Al atoms in white and Ga atoms in cyan.

that the Al atom does not lose its distinctness even above the melting temperature as also indicated by the changes in the amplitude of its MSD in comparison to any other atom of the $Ga_{19}Al^+$ cluster.

5.2 $Ga_{11}Al_9^+$ and $Ga_3Al_{17}^+$

In order to investigate the melting behaviour of Ga-Al nanoalloy clusters with larger aluminium composition, two more cluster sizes were studied in the $Ga_{(20-x)}Al_x^+$ series: $Ga_{11}Al_9^+$ and $Ga_3Al_{17}^+$. $Ga_{11}Al_9^+$ was chosen because it was shown to be the most favourable cluster as predicted by the energy of mixing calculations (Fig. 5.2) and $Ga_3Al_{17}^+$ cluster to understand what happens, both electronically and in cluster dynamics, to an Al_{17} cluster (which as per previous DFT calculations[197] splits water more efficiently than bulk Al to produce hydrogen) when 3 extra Ga atoms are mixed and the cluster acquires a positive charge.

Calculation details

The starting structures of both the clusters, shown in Fig. 5.11, were obtained from the SP configuration as had been described earlier. Similar settings were used to achieve the relative convergences of the microcanonical and canonical specific heat curves for both clusters as previously stated. The calculations were run for 160 ps (step size 2 fs) for $Ga_{11}Al_9^+$ and 46.2 ps (step size 0.8 fs) for $Ga_3Al_{17}^+$ cluster. A smaller step size in $Ga_3Al_{17}^+$ helped to arrest the fluctuations in energy during the microcanonical simulations.

5.2.1 Thermodynamics

The top panel of Fig. 5.12 shows the normalised canonical specific heat capacity curves obtained from the multiple histogram method for $Ga_{11}Al_9^+$ and $Ga_3Al_{17}^+$ clusters. The solid-liquid-like phase transition temperature obtained is 824 K and

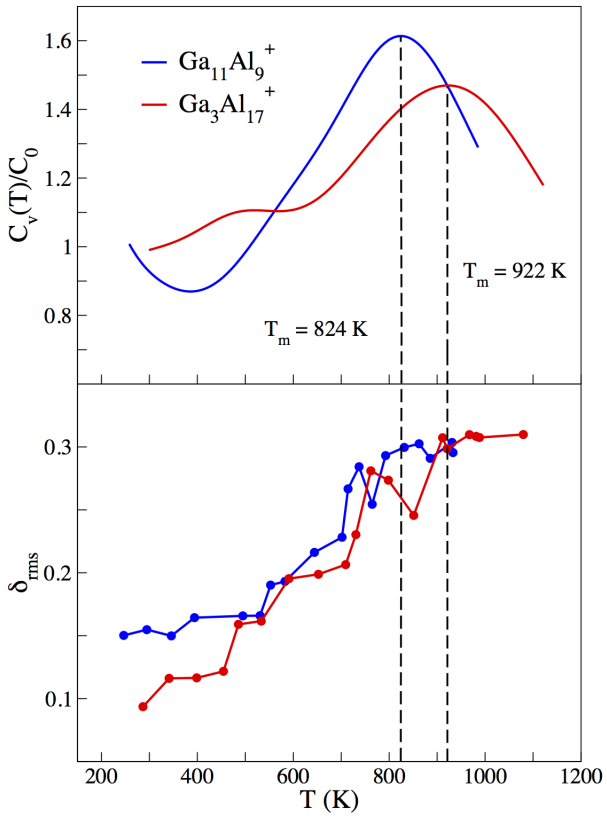

Figure 5.12: Comparison of canonical specific heat curves of $Ga_{11}Al_9^+$ and $Ga_3Al_{17}^+$ (top panel) and the root-mean-squared (RMS) bond-length fluctuations (bottom panel) as a function of temperature.

922 K for $Ga_{11}Al_9^+$ and $Ga_3Al_{17}^+$ clusters respectively. Thus, similar to the observations in Ga_{20}^+, Al_{20}^+ and $Ga_{19}Al^+$ clusters, the *greater-than-bulk melting* behaviour is observed in these two gallium aluminium bimetallic clusters as well.

5.2.2 Structural changes and atomic mobility: Lindemann index, pair distribution function (PDF), mean squared displacement, average coordination number and diffusion coefficients

The bottom panel of Fig. 5.12 shows the calculated values of the Lindemann index at various temperatures for $Ga_{11}Al_9^+$ (shown in blue) and $Ga_3Al_{17}^+$ (shown in red)

respectively. The fluctuations in the bond-lengths of both the clusters exhibit low values (∼0.1-0.15) at the lowest energy and increases with temperature, thereby, converging at ∼0.3 above the melting temperature, a characteristic signature of the phase transition.

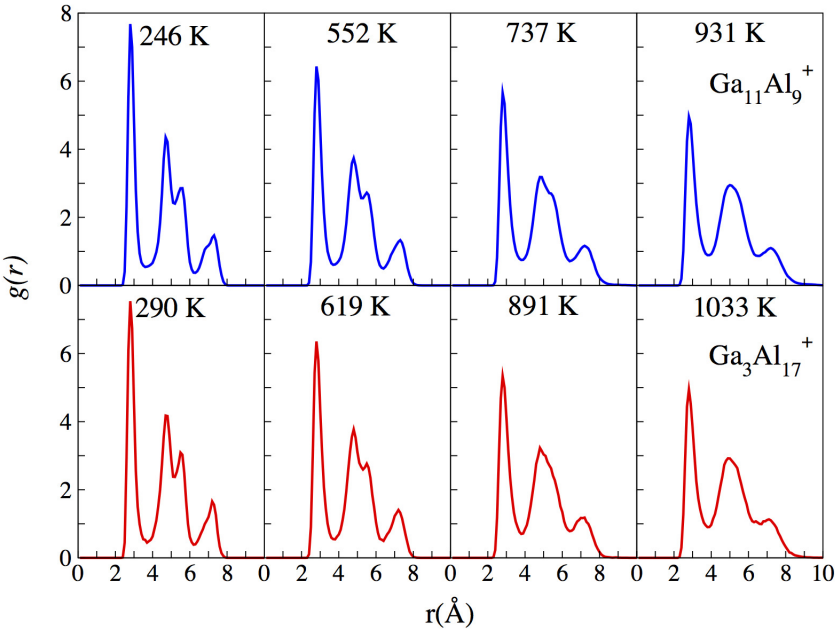

Figure 5.13: Comparison of the pair distribution function (PDF) of $Ga_{11}Al_9^+$ and $Ga_3Al_{17}^+$ clusters at different temperatures.

Fig. 5.13 shows a comparison of the pair distribution functions obtained at different simulated energies (average temperatures as mentioned in inset) for $Ga_{11}Al_9^+$ and $Ga_3Al_{17}^+$ clusters respectively. We observe similar changes in the structures of both the clusters with increasing energy below and above the respective melting temperatures reflecting the presence of similar isomeric structures at higher temperatures, as also confirmed from the MD movies.

A comparison of the mean squared displacements of the aluminium and gallium atoms in $Ga_{11}Al_9^+$ cluster at the lowest and the highest simulated energy is shown in Fig. 5.14. The MSD amplitudes of the internal Al atoms (coloured red and blue) shows a considerable change with energy whereas those of the surface gallium and aluminium atoms does not increase significantly. Similar MSD behaviour of all the Al atoms at the highest energy also corroborates to a *liquid-like* state.

The calculated MSDs for $Ga_3Al_{17}^+$ cluster is shown in Fig. 5.15. One of the three Ga atoms, coloured orange in inset, shows a behaviour (MSD values) in between the internal and the other surface atoms. This difference, however, vanishes with increase in energy and all the surface atoms have similar MSD values. Similar to the picture in $Ga_{11}Al_9^+$ cluster, it is the internal Al atoms (blue and red) which show a

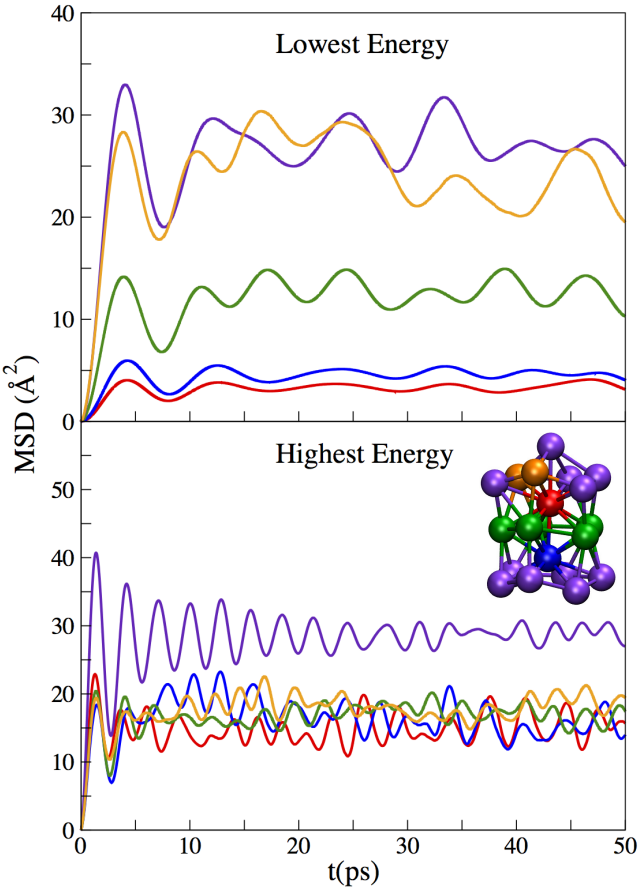

Figure 5.14: Comparison of mean squared displacement (MSD) of $Ga_{11}Al_9^+$ at lowest (246 K) and highest energy (931 K) as a function of time. Atoms in red and blue are the central Al atoms; green and orange corresponds to MSD averaged over all the Al atoms in the central and top ring respectively; indigo represents the average MSD of Ga atoms as also shown in inset. For references in the text, the more highly coordinated internal atom (red) is referred as *a* and the other (coloured blue) as *b*.

considerable change in the MSD values between the lowest and the highest energy. Also, in $Ga_3Al_{17}^+$ cluster similar MSD curves are observed for all the atoms at the highest energy reflecting a *liquid-like* state.

Fig. 5.16 shows the average coordination numbers, calculated using the first minimum in $g(r)$ as the cutoff neighbouring distance, for the representative atoms (coloured in inset) for $Ga_{11}Al_9^+$ cluster. Below the melting temperature of 824 K, the internal Al atoms are surrounded by 9 or more neighbouring atoms on average. However, in the *liquid-like* state similar coordination numbers for the Al atoms indicates that they become indistinguishable. The gallium atoms prefers to occupy the surface sites at all temperatures.

Similar to the $Ga_{11}Al_9^+$ cluster, the average coordination number of the Ga and

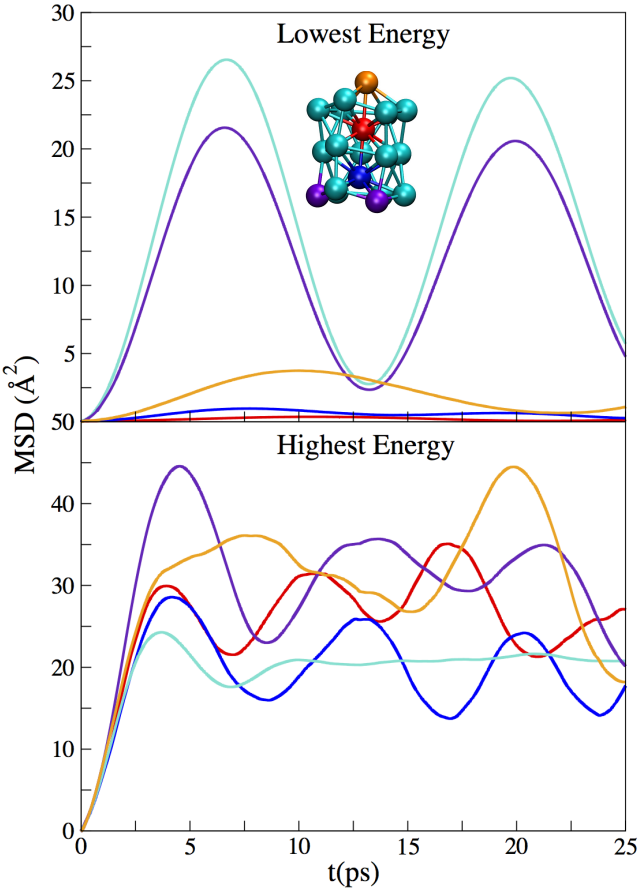

Figure 5.15: Comparison of mean squared displacement (MSD) of $Ga_3Al_{17}^+$ at lowest (286 K) and highest energy (1079 K) as a function of time. Atoms in red and blue are the central Al atoms; turquoise and indigo corresponds to MSD averaged over all the surface Al and bottom ring Ga atoms respectively. Orange represents the MSD of top Ga atom. For references in the text, the more highly coordinated internal atom (red) is referred as *a* and the other (coloured blue) as *b*.

Al atoms in the $Ga_3Al_{17}^+$ cluster shows a clear difference between the internal Al atoms and the surface Al and Ga atoms up to 850 K. However, at 778 K the more highly coordinated internal atom (coloured red) occupies a coordination site of 9 atoms on average indicating an isomeric structure with only one internal site (blue) but moves back to being an internal site at the next simulated energy (808 K), before occupying a surface site at all temperatures above 834 K. Furthermore, at 891 K both the lowest energy internal Al atoms (blue and red) are replaced by the surface atoms (magenta and green) reflecting atoms swapping sites as also observed in MD movies. At the highest simulated energy above the melting temperature, the Al atoms have 6 to 7 atoms on average and the Ga atoms prefer even lower coordination of 5 atoms.

Shown in the top and bottom panel of Fig. 5.18 are the diffusion coefficients

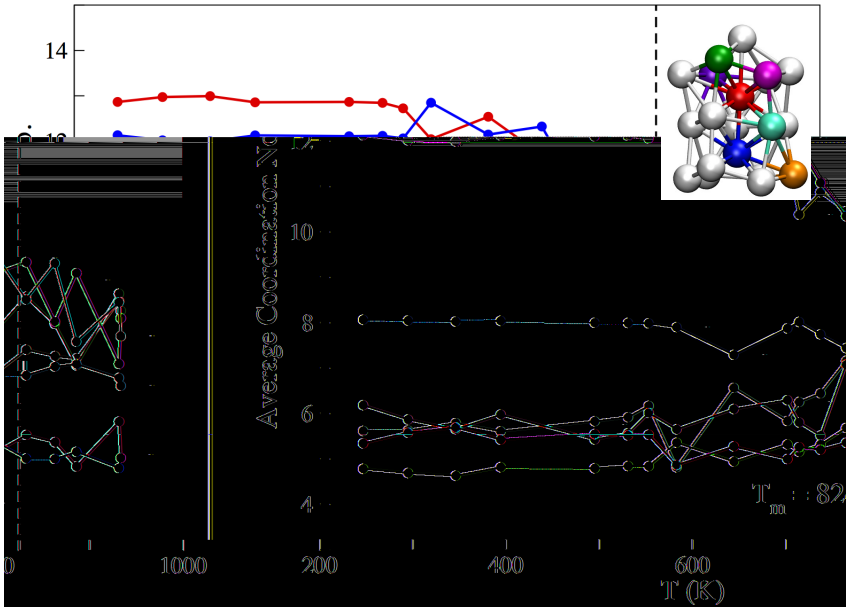

Figure 5.16: Comparison of average coordination number (ACN) of atoms (coloured in inset) of $Ga_{11}Al_9^+$ as a function of temperature. Atoms in red and blue are the central Al atoms; green, indigo and turquoise are the representative surface Al atoms; magenta and orange are the representative surface Ga atoms.

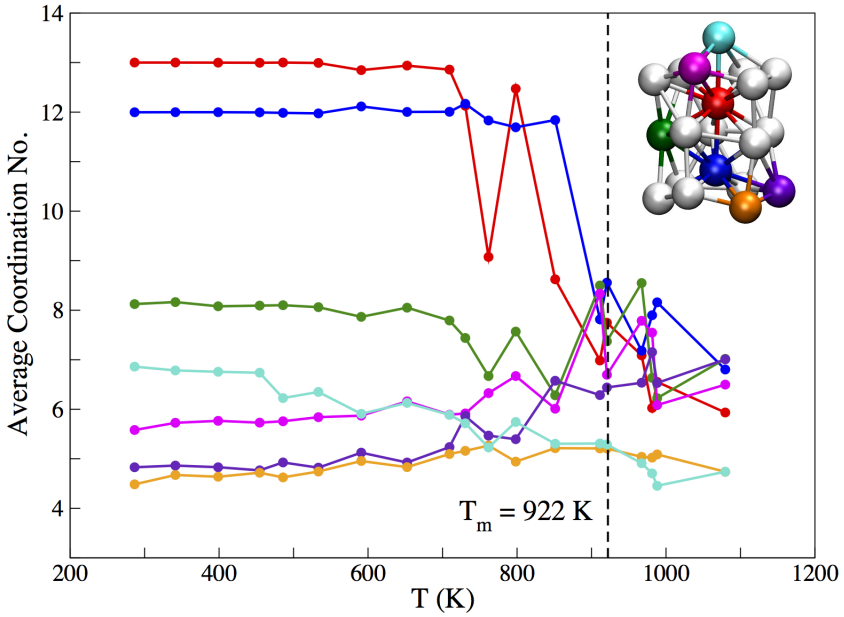

Figure 5.17: Comparison of average coordination number (ACN) of atoms (coloured in inset) of $Ga_3Al_{17}^+$ as a function of temperature. Atoms in red and blue are the central Al atoms; green, indigo and magenta are the representative surface Al atoms; turquoise and orange are the representative surface Ga atoms.

obtained for $Ga_{11}Al_9^+$ and $Ga_3Al_{17}^+$ clusters respectively. The details of the calculation is similar to those for the Al_{20}^+ clusters as described in the previous chapter.

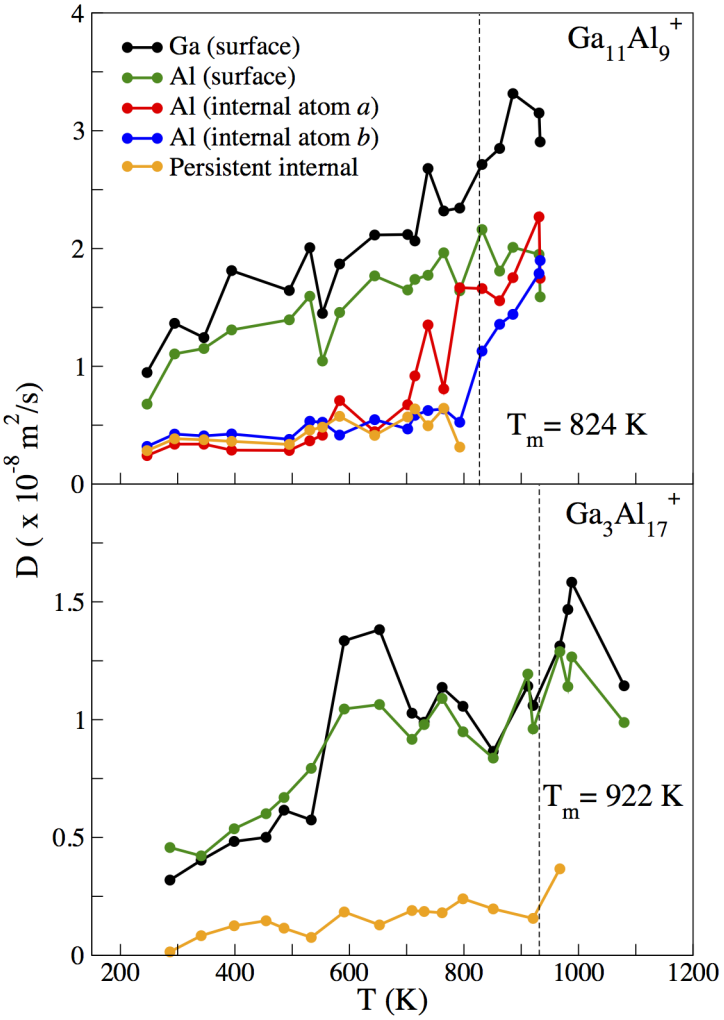

Figure 5.18: Diffusion coefficient of internal and surface atoms as a function of temperature. The vertical dotted line denotes the melting temperature.

The diffusion coefficients of the surface Ga and Al atoms are very high in comparison to the internal and the *'persistent internal'* atoms in both the clusters. Moreover, it is not until 701 K that the more highly coordinated internal atom starts to diffuse in $Ga_{11}Al_9^+$ cluster. However, it is only after the melting temperature is reached that the diffusion coefficient of the internal atoms start to increase and at the highest temperature to become comparable to the rest of the Al atoms in $Ga_{11}Al_9^+$ cluster. The diffusion coefficient of only the *'persistent internal'* atom(s) in $Ga_3Al_{17}^+$ cluster is shown in the bottom panel of Fig. 5.18 because of the constant swapping between the atoms occupying the internal and surface sites prior to the melting temperature (also clear from the average coordination number plot shown in Fig. 5.17) which made it harder to tag a particular atom as internal.

5.2.3 Atoms-in-molecules analysis

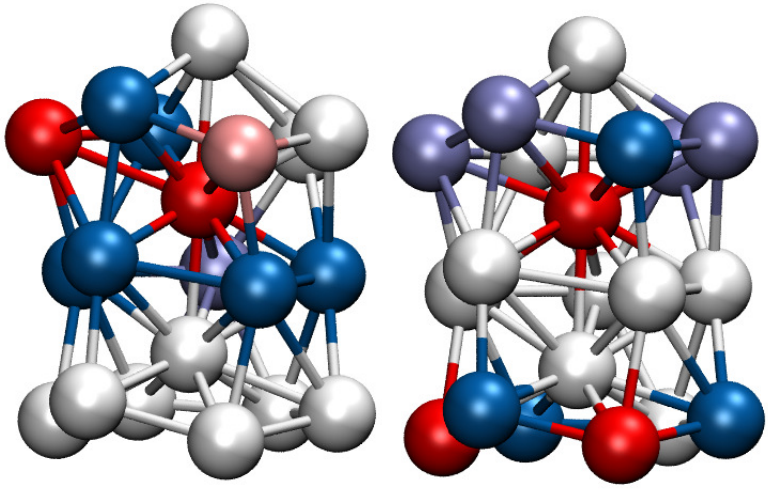

(a) $Ga_{11}Al_9^+$ (b) $Ga_3Al_{17}^+$

Figure 5.19: Partial charges (q) obtained by atoms in molecules (AIM) analysis for Al_{20}^+ clusters: (red) q $\leq$ -0.2e ; (pink) -0.2e $<$ q $\leq$ -0.1e ; (white) -0.1e $<$ q $\leq$ 0.1e ; (ice blue) 0.1e $<$ q $\leq$ 0.2e ; (dark blue) q $>$ 0.2e.

Partial charges associated with each of the aluminium and gallium atoms in $Ga_{11}Al_9^+$ and $Ga_3Al_{17}^+$ clusters as obtained by atoms-in-molecules analysis is shown in Fig. 5.19. Similar charge distribution between the internal and surface sites as seen in Al_{20}^+ cluster is observed. The more highly coordinated internal Al atom becomes negatively charged with the other staying neutral. Among the charged surface atoms, the negative charge is observed by the gallium atoms and the aluminium atoms become positively charged.

Thus, the mixed phases of $Ga_{(20-x)}Al_x^+$ clusters i.e. $Ga_{19}Al^+$, $Ga_{11}Al_9^+$ and $Ga_3Al_{17}^+$, also show the *greater-than-bulk melting* behaviour. In $Ga_{19}Al^+$ cluster the Al atom prefers to occupy the internal site in the *solidlike* and the *liquidlike* phases. Similar to the observation in the Al_{20}^+ cluster, QTAIM predicts charge segregation between the internal and surface atoms - a feature which seems to play an important role for the clusters to show the *greater-than-bulk melting* behaviour. Moreover, with increase in Al content, the difference between the cluster and the corresponding bulk alloy melting temperature decreases. In the next chapter, this information is used to construct a phase diagram for the $Ga_{(20-x)}Al_x^+$ nanoalloy system.

Chapter 6

A first attempt at a phase diagram

Phase diagrams allow us to study the dependence of the bulk metallic compositions on the alloy phase transition temperatures. Moreover, few attempts have already been made to extend the construction of phase diagrams to nanoalloys[198, 199, 200, 94]. Since models[201, 202] typically used for bulk phases are unsuitable in these size ranges, highly sensitive first-principles calculations are called for.

This chapter describes the construction of the phase diagram for $Ga_{(20-x)}Al_x^+$ bimetallic cluster system which shows the *greater-than-bulk melting* behaviour. Furthermore, we have attempted to understand the melting temperature of the gallium-aluminium nanoalloys with a simplified model where the melting temperature of the cluster is written as a sum of the melting temperature of the bulk alloy and contributions from the energy of mixing and the 'greater-than-bulk' characteristic. The latter parameter has been extracted from the molecular dynamics simulations presented in Chapter 4 and 5. The temperatures obtained from this simple intuitive picture when compared to the DFT calculated melting temperatures for the nanoalloy phases are within 2% tolerance.

6.1 The energy of mixing and atoms-in-molecules analysis

Although the changes in the energy of mixing with composition in the $Ga_{(20-x)}Al_x^+$ clusters has been already described previously in the context of the selection for the mixed clusters, this chapter describes how the changes in the energy of mixing and the calculated phase transition temperature are affected by the composition. Table 6.1 compares the calculated cluster and the corresponding bulk alloy melting temperatures and the changes in energy of mixing of the mixed clusters with respect

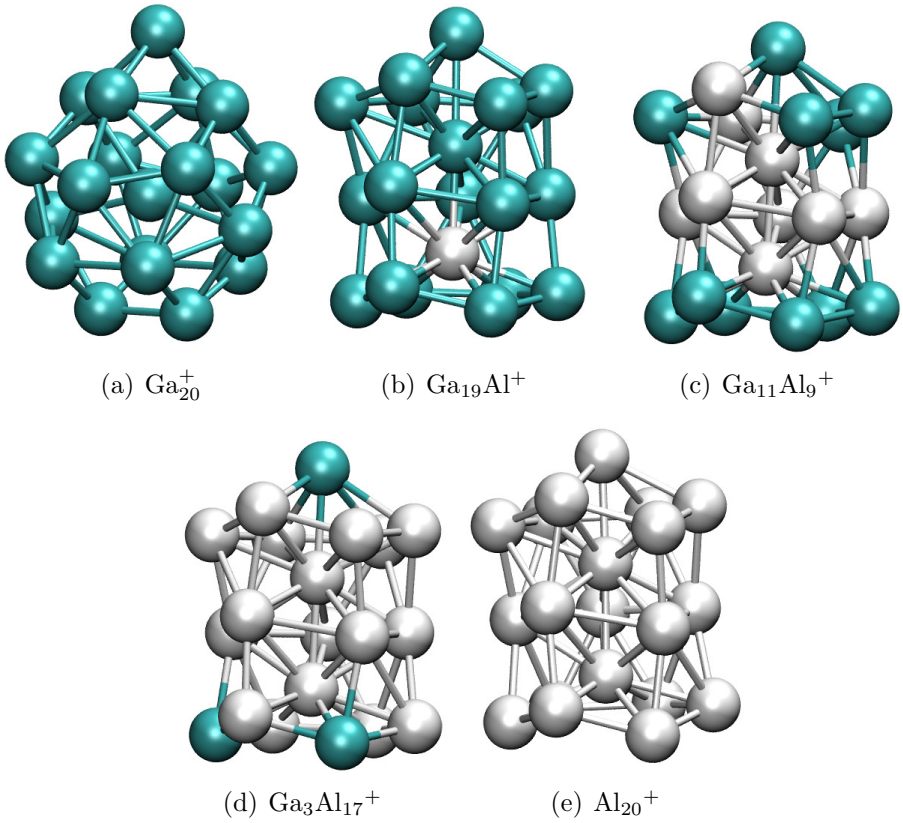

(a) Ga_{20}^{+} (b) $Ga_{19}Al^{+}$ (c) $Ga_{11}Al_9{}^{+}$

(d) $Ga_3Al_{17}{}^{+}$ (e) $Al_{20}{}^{+}$

Figure 6.1: Starting structures in the capped sphere (Ga_{20}^{+}) and stacked plane ($Ga_{19}Al^{+}$, $Ga_{11}Al_9{}^{+}$, $Ga_3Al_{17}{}^{+}$ and $Al_{20}{}^{+}$) configurations with Al atoms in white and Ga atoms in cyan.

to the pure cluster phases. The difference between the cluster and the bulk alloy melting temperature, ΔT_m, increases as one Al atom replaces a Ga atom to form $Ga_{19}Al^{+}$ cluster. However, with increasing Al composition in the cluster, as seen for $Ga_{11}Al_9{}^{+}$ and $Ga_3Al_{17}{}^{+}$ clusters, leads to a decrease in the ΔT_m value. This is similar to the change observed in the energy of mixing values where a positive value is observed for $Ga_{19}Al^{+}$ cluster but negative values for $Ga_{11}Al_9{}^{+}$ and $Ga_3Al_{17}{}^{+}$ clusters, thus, reflecting the role of the energy of mixing in the *greater-than-bulk* melting behaviour of these clusters.

To understand how the charge distribution between the internal and surface sites affects the segregation or mixing behaviour (as seen from the energy of mixing plot in the top panel of fig. 6.2) in each composition of $Ga_{(20\text{-}x)}Al_x{}^{+}$ cluster system, the atoms-in-molecules analysis for each cluster is performed. As already described in the previous chapter, the starting structures of each cluster, except $Ga_{20}{}^{+}$, were obtained from the SP geometry as shown in Fig. 6.1, the optimised geometries of the representative clusters are compared. The strategy to classify the obtained partial charges (q_i) for each atom is that an atom is considered negatively charged

Table 6.1: Comparison of the melting temperatures of Ga-Al alloys in cluster and bulk phase[95].

	Cluster T_m(K)	Bulk T_m(K)	ΔT_m(K)	E_{exc}(eV)
Ga_{20}^+	616	303	313	0
$Ga_{19}Al^+$	686	353	333	0.347
$Ga_{11}Al_9{}^+$	824	646	178	-0.497
$Ga_3Al_{17}{}^+$	922	857	65	-0.237
$Al_{20}{}^+$	993	933	60	0

if $q_i < -0.1e$, neutral if $-0.1e \leq q_i \leq 0.1e$ and positively charged if $q_i > 0.1e$.

The bottom panel of Fig. 6.2 describes the obtained charge distribution picture. The $Ga_{20}{}^+$ capped sphere structure has the internal atom as negatively charged and one surface atom as positively charged with the other surface atoms remaining neutral. As already described in the previous chapter, the internal Ga and Al atoms in $Ga_{19}Al^+$ cluster forms a strong dipole with the Al atom getting positively charged and the Ga atom as negatively charged. However, no negatively charged surface atoms are observed. Both the internal Al atoms get positively charged in $Ga_{18}Al_2{}^+$ and $Ga_{17}Al_3{}^+$ clusters and negatively charged surface atoms are also observed in $Ga_{17}Al_3{}^+$ cluster. From $Ga_{16}Al_4{}^+$ onwards, one neutral internal atom and the other as positively charged is observed up to $Ga_{14}Al_6{}^+$ cluster and as negatively charged from $Ga_{13}Al_7{}^+$ up to $Ga_3Al_{17}{}^+$ cluster. The other three remaining clusters $Ga_2Al_{18}{}^+$, $GaAl_{19}{}^+$ and $Al_{20}{}^+$ have both the internal sites as negatively charged. Thus, segregation (energy of mixing being positive) corresponds to either a strong dipole formation between the two internal atoms in SP configuration ($Ga_{19}Al^+$) or the absence of negative charge in the overall positively charged cluster($Ga_{18}Al_2{}^+$).

6.2 $Ga_{(20-x)}Al_x{}^+$ phase diagram

From the statistical analyses of the average coordination number and the diffusion coefficients for the representative clusters as described in the previous chapters and the atoms-in-molecules analysis of all the clusters in $Ga_{(20-x)}Al_x{}^+$, it can be observed that there is a difference between the internal and surface atoms in these clusters. The results corroborate a picture where the internal atoms are confined in an electrostatic cage, disruption of which leads to the solid-liquid-like phase transition in these clusters. This physical picture, bringing out the difference in the environments of the internal and surface atoms (which is unlike the bulk phase environment), can help explain the cause behind the *greater-than-bulk* (from here onwards referred to

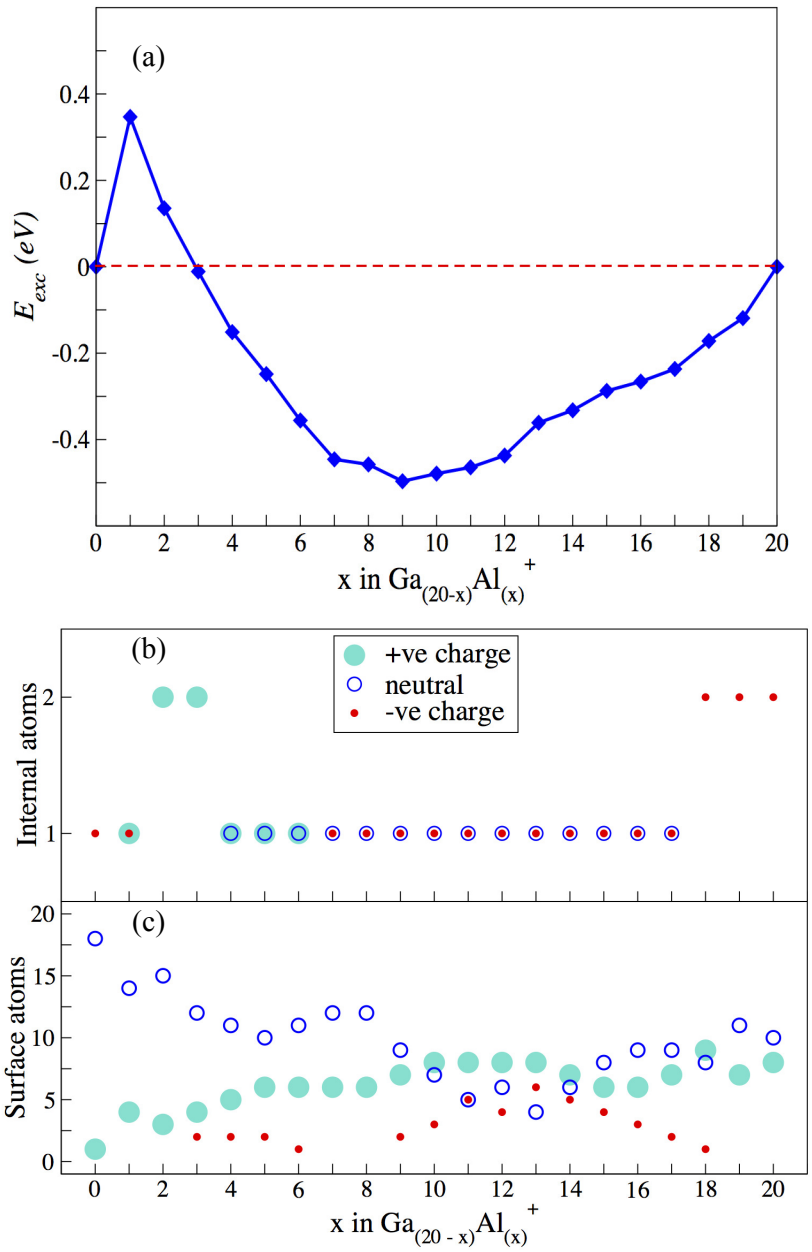

Figure 6.2: Excess energy for all the compositions in $Ga_{20-x}Al_x^+$, panel (a), and the corresponding atoms-in-molecules analysis where the red dot, blue open circle and turquoise circle represents negative, neutral and positive charges.

as the GB character) *melting* behaviour of $Ga_{(20-x)}Al_x^+$ clusters.

Taking into account the associated intrinsic elemental character of Ga and Al (to be common in the bulk and cluster phase), the GB character and the energy of mixing, a simple view of the $Ga_{(20-x)}Al_x^+$ cluster system to be a remnant of the corresponding bulk alloy phase with additional properties is proposed as also

expressed by

$$T_m(Ga_{(20-x)}Al_x^+) = T_{bulk}(Ga : Al :: (20-x) : x) + \nu_{GB} + \nu_{exc}. \tag{6.1}$$

Here ν_{GB} and ν_{exc} represent the size specific *greater-than-bulk melting* and the mixing energy contributions to $Ga_{(20-x)}Al_x^+$ cluster formed from the corresponding bulk alloy mixture, and T_m, T_{bulk} represent the cluster and the bulk alloy melting temperatures respectively. Next follows the description of a way to quantify the *greater-than-bulk melting* (ν_{GB}) parameter and a comparison between the melting temperature obtained from this picture and those calculated from the DFT simulations.

6.2.1 The *greater-than-bulk* (GB) melting character

The picture of an electrostatic cage confining the internal atoms in the $Ga_{(20-x)}Al_x^+$ clusters is considered to quantify the GB character. Furthermore, the term 'energy barrier' is attributed to the differences in the environments of the internal and the surface atoms. As the temperature increases, the internal and surface atoms tend to cross this 'energy barrier' more frequently and thus either exchange their positions or become a surface (or internal) atom itself leading to the isomeric or homotopic cluster structures. This change in the cluster structure either due to a change in the number of internal sites or the atom occupying the internal site (brought about either by parallel tempering or swapping between atoms) is, from here onwards, referred as *Change-Swap (CS)*. Characterising the *liquid-like* state as one where all the atoms have equal probability to occupy the internal or the surface sites, an Arrhenius-like description is used to understand the 'energy barrier' and how it changes with composition in the $Ga_{(20-x)}Al_x^+$ cluster system as also expressed by

$$ln\ k_{CS} = ln\ A - E_{barrier}\left(\frac{1}{T}\right). \tag{6.2}$$

Here, k_{CS} is the rate constant in ns^{-1}, T is the temperature in Kelvin, A is the pre-exponential factor and $E_{barrier}$ represents the energy barrier between the internal and surface sites. k_{CS} is the ratio of the total number of times a CS occurs to the MD trajectory length (in ns^{-1}). Thus, computing $E_{barrier}$ provides a way to quantify the existing 'environmental difference' between the internal and the surface sites and correlate it with the *greater-than-bulk melting* parameter ν_{GB}.

Shown in the inset of Fig. 6.4 are the data points and the corresponding linear least squares fit when k_{CS} is obtained using the *'persistent internal'* atom criterion (a). The data points below the melting temperature show stronger fluctuations, and

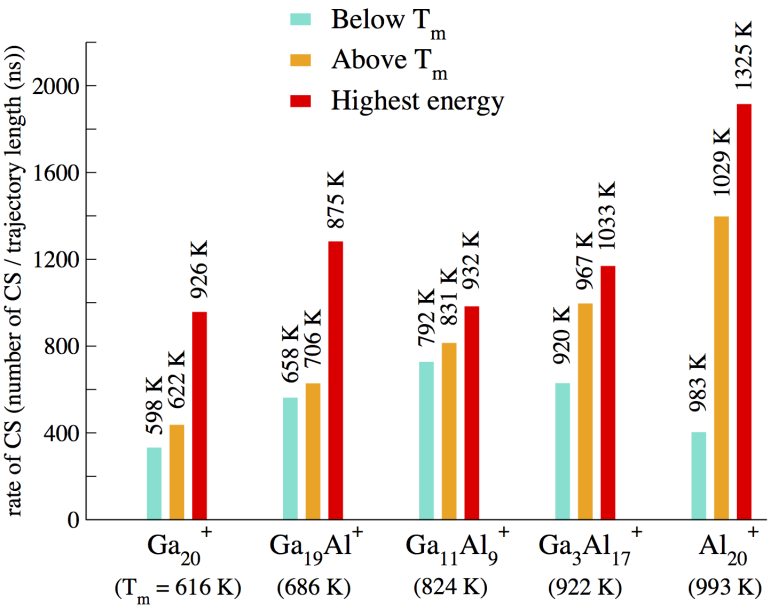

Figure 6.3: Rate of change-swap (CS) between the internal and external atoms in the representative $Ga_{(20-x)}Al_x^+$ clusters. The temperatures at which the rate of CS was calculated is written above the bars.

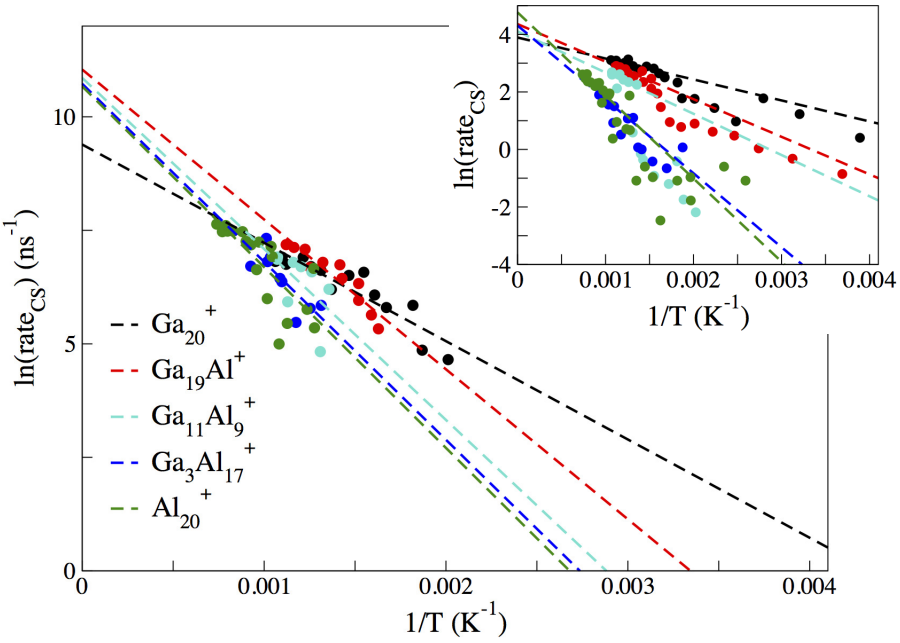

Figure 6.4: Arrhenius plot showing the dependence of natural logarithm of the rate of CS between the internal and surface sites to the inverse of temperature. The dashed lines are the least-square straight line fits to the data points obtained from the convex hull method. The inset shows the corresponding data points obtained from the *persistent internal* atom criterion (a). The line fit has been done only for temperatures above the melting point for each cluster.

Table 6.2: Comparison of the $E_{barrier}$ values obtained using the two methods described above.

	'Persistent internal' atom criterion *(a)*	Convex hull method
Ga_{20}^{+}	729.5	2165.6
$Ga_{19}Al^{+}$	1306.5	3301.4
$Ga_{11}Al_9{}^{+}$	1433.9	3767.3
$Ga_3Al_{17}{}^{+}$	2570.2	3921.3
$Al_{20}{}^{+}$	2889.5	3982.3

thus the line-fit is performed only for the data points above the melting temperatures. Table 6.2 shows the obtained $E_{barrier}$ values from the slopes of the line-fit. It can be observed that with increasing Al composition in the $Ga_{(20-x)}Al_x{}^{+}$ cluster system, the $E_{barrier}$ value increases thus indicating ν_{GB} to be a monotonically increasing function of the composition of Al atoms. Although, one could use the obtained $E_{barrier}$ values to construct the phase diagram, the 'persistent internal' atom criterion (a) was found to be quite loose to tag a particular atom as *internal* below the melting temperatures.

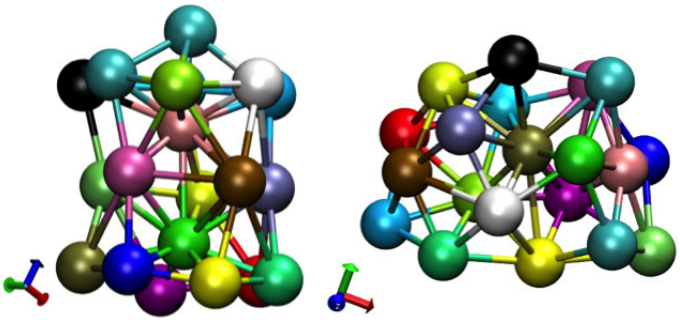

(a) (b)

Figure 6.5: Changes in the structure and the number of internal atoms and the atom-type occupying the internal site due to parallel tempering as observed in the movie.

From the MD movies, two ways are found in which a CS occurred: (i) stage-wise where a surface atom becomes internal with subsequent MD steps, as shown in Fig. 6.6, and (ii) due to parallel tempering as shown in Fig. 6.5 for $Al_{20}{}^{+}$ clusters at 809 K.

The convex hull technique[203] is used to accurately tag an atom as *internal* at each MD step. For a finite set of points, the convex hull is the union of all possible convex combinations. The convex hull of the 20 cartesian coordinates (atomic sites) at each MD step in both two and three dimensions is created. The hull vertices in the three dimensions are disregarded and the non-hull vertices are considered as the

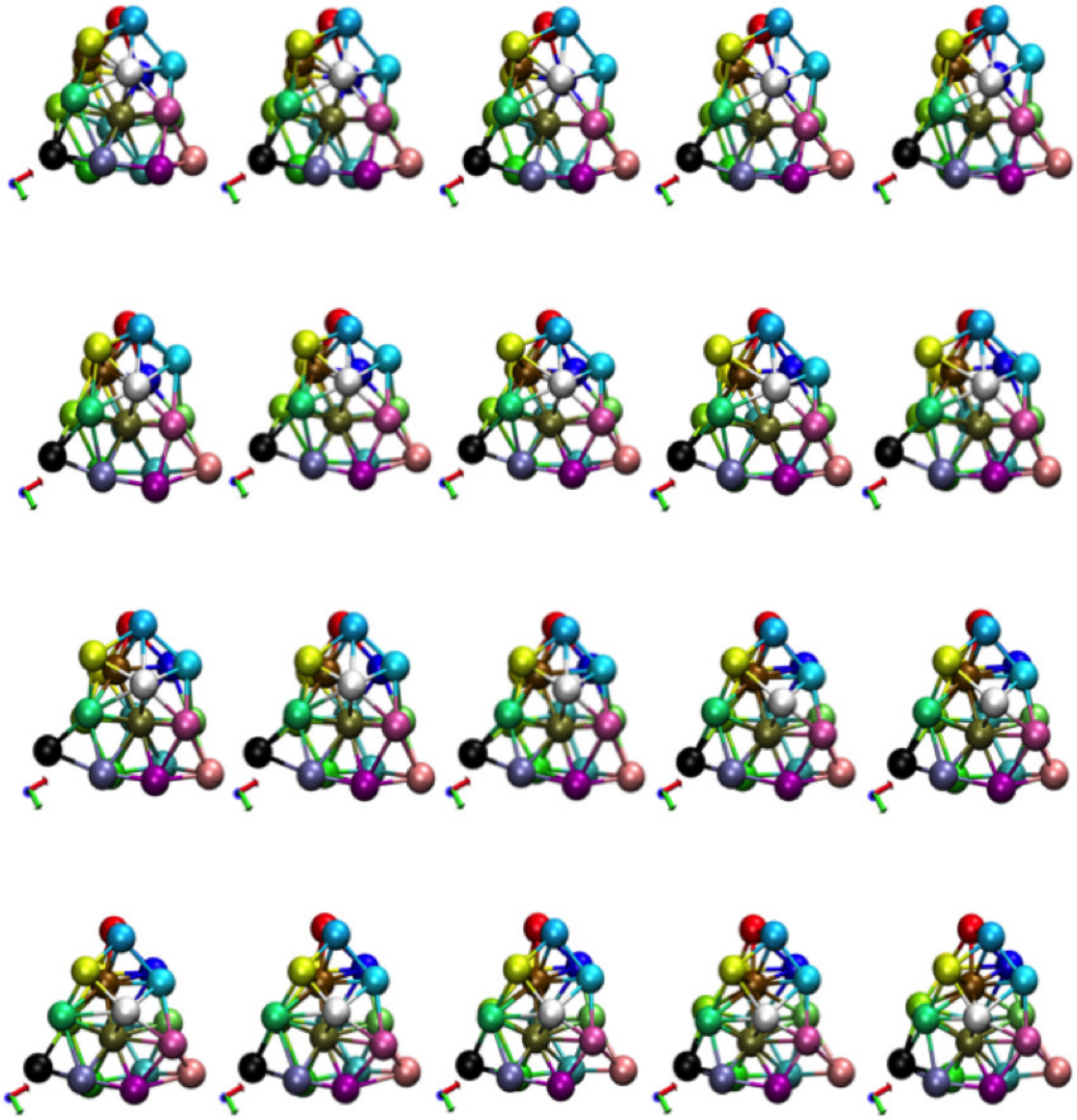

Figure 6.6: Twenty consecutive movie steps showing how the surface atom (circled, brown) becomes an internal atom and thus the number of internal atoms changes from one (colored as tan) to two (tan and brown). Note that the overall shape of the cluster does not undergo a significant change.

prospective internal atoms. In the two dimensions, the convex hull for the top, front and side view is created. A cartesian coordinate (atomic site) is considered *internal* if it is a non-hull vertex in all the three two-dimensional convex hulls and also a member of the non-hull vertices set in the corresponding three-dimensional convex hull. Furthermore, the vertex has to satisfy the *'persistent internal'* atom criterion (a).

Shown in Fig. 6.3 is the rate of CS calculated using the convex hull technique for the five representative clusters at temperatures below the melting temperature, above the melting temperature and at the highest simulated energy where the clusters are fully *liquid-like*. Those parallel tempering swaps where there is a change only in the number of internal atoms (isomeric) in contrast to those where there is a change of the atom occupying the internal site as well (homotopic) have been ignored. For all the clusters there is an increase in the rate of CS with temperature. Furthermore, below the melting temperature the rate of CS is dependent on the amount of mixing, which for $Ga_{11}Al_9^+$ is the highest.

The natural logarithm of the calculated CS rate at different temperatures for all the representative clusters is shown in Fig. 6.4. The temperatures for which the total CS count was less than ten discrete instances during the simulated MD trajectory or the contribution of PT to the CS count was more than 15% have been discarded, leaving a minimum of eight data points for each cluster. The dashed lines represent the linear least squares fit to the data points. The importance of the new technique to gauge a CS situation is reflected by the significant decrease in the spread of the data points below the melting temperature when compared to that obtained from *'persistent internal'* atom criterion (a) alone as shown in the inset of Fig. 6.4. The $E_{barrier}$ values obtained from the slopes of the line-fit have been tabulated in Table. 6.2. Again there is an increase in the energy barrier for a CS situation as the Al content increases in the $Ga_{(20-x)}Al_x^+$ clusters. Moreover, the choice of method to tag a particular atom as *internal* and the number of data points also affects the $E_{barrier}$ value.

6.2.2 Creating the phase diagram

Correlating the ΔT_m values with the $E_{barrier}$ values as tabulated in Table 6.2, one can find that there is an inverse relationship between ΔT_m and the GB character. ν_{GB} is expressed as a function of $E_{barrier}$ as

$$\nu_{GB} = \alpha f(E_{barrier}), \tag{6.3}$$

where α is a parameter to be optimised. A linear least squares fit is performed to the obtained $E_{barrier}$ values for the pure cluster phases, i.e. Ga_{20}^+ and Al_{20}^+, which gives the function $f(E_{barrier})^*$ in Eq. 6.3 and optimise α. The obtained ν_{GB} values are added to the bulk melting temperatures for the representative mixed cluster phases as represented by the green triangles in Fig. 6.7. To add the energy

*Note that $f(E_{barrier})$ is a function of composition.

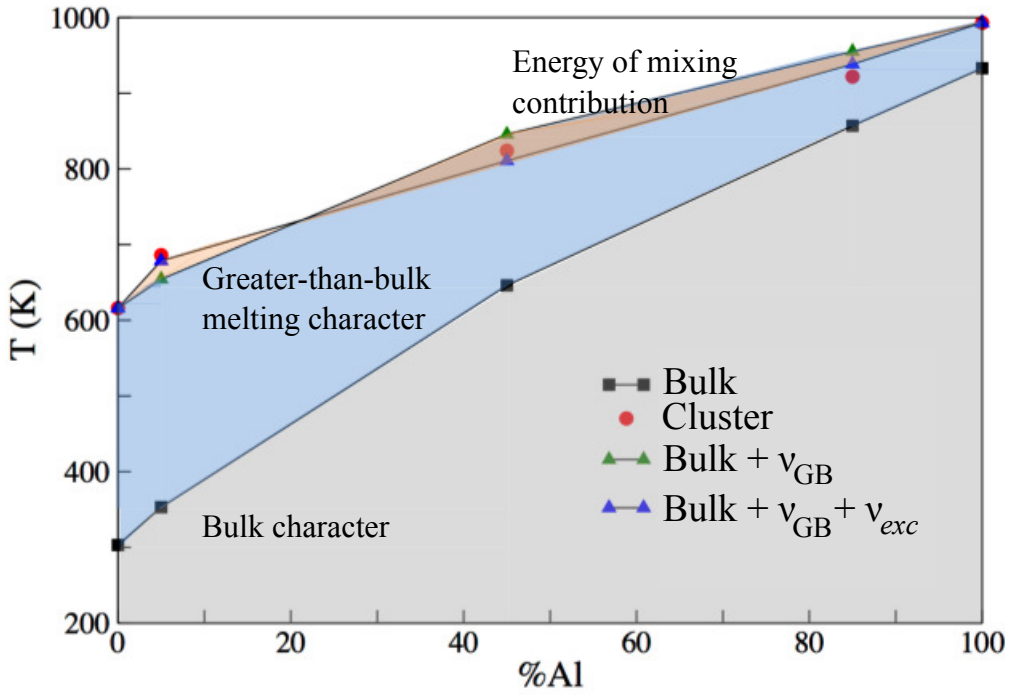

Figure 6.7: Comparison of the DFT calculated cluster melting temperature (red) of the five representative compositions of $Ga_{(20-x)}Al_x^+$ cluster system to that obtained considering the picture described in Eq. 6.1.

of mixing contribution to the obtained cluster melting temperatures, ν_{exc} is first expressed as

$$\nu_{exc} = \beta(E_{exc}), \tag{6.4}$$

where β is another parameter to be optimised and then, added to the calculated melting temperatures in the previous step. The corrected values (represented as blue triangles in Fig. 6.7) are within 2% error from the DFT calculated melting temperatures of the mixed clusters (red circles in Fig. 6.7).

Thus, the view of a $Ga_{(20-x)}Al_x^+$ cluster being a remnant of the corresponding bulk alloy with additional size and composition specific characteristics holds with excellent agreement in the melting temperatures when compared to those obtained from the DFT calculations. Employing an Arrhenius-like description provides a way to quantify the size and composition dependent factors in these systems. However, to generalise this description of clusters, one also needs to address the situation as to how the size and composition dependent contributions change when the melting temperature of the cluster is less than the corresponding bulk phase melting temperature. One also needs to consider the methods which could be employed to quantify those contributions. It must also be noted that the entropic effects[160, 204] also play a part in the observed thermodynamic behaviour of the clusters. How they feature

in the description of nanoalloys is also a subject requiring further investigation.

Chapter 7

Conclusions and future work

The underlying cause behind the *greater-than-bulk melting* behaviour of gallium clusters has been a matter of persistent interest since Jarrold and coworkers first reported [72] in 2003, disproving the generality of the depression in melting point with size paradigm of Pawlow [36]. To fully understand gallium, one must answer how the metallic and covalent bonding can coexist, and do so in a manner that changes non-monotonically with size. For aluminium clusters, the results showed peak in the heat capacity plots for cluster sizes comprising 28 or more atoms [86]. Furthermore, when an Al atom was doped in the gallium clusters ($Ga_{n-1}Al^+$), the melting temperatures and latent heats were found to be similar to the corresponding pure gallium cluster analogs ($Ga_n{}^+$) [196].

Solid-liquid phase transition is a phenomenon which goes to the heart of our physical understanding of matter. At very small sizes comprising few tens of atoms, the meaning of the occurrence of a peak in the measured heat capacity of a system becomes questionable and needs to be addressed to fully understand the matter at nanoscale. For a cluster comprising 20 atoms the experimental results reported show: *greater-than-bulk melting* behaviour in gallium, no distinguishable peak in the specific heat can be observed in aluminium and, $Ga_{19}Al^+$ has thermodynamical behaviour similar to that of $Ga_{20}{}^+$ [196, 86].

Pertinent questions arise concerning what exactly happens in $Al_{20}{}^+$ clusters: does it melt over a range of temperatures resulting in the non-existence of a sharp peak in the heat capacity plot or can it show the *greater-than-bulk melting* behaviour as well and hence the peak position in the heat capacity plot could be above the maximum temperature scanned during the experiments (1060 K) considering that the melting temperature of bulk aluminium is 933 K. Furthermore, how does the melting temperature of the mixed nanoalloy phase change with the composition? Does it also show the *greater-than-bulk melting* behaviour or is the *greater-than-bulk*

melting behaviour restricted to compositions dominated by the gallium atoms?

This thesis is an attempt to answer these questions. First principles Born-Oppenheimer based molecular dynamics have been used to understand the solid-liquid-like phase transitions in the 20 atom gallium aluminium nanoalloy system. Following are the results obtained from this study:

(a) Greater-than-bulk melting behaviour is not restricted to only gallium clusters in the Group 13 elements of the periodic table but can also be observed in aluminium clusters (Al_{20}^+) as well. Thus, in the size limit of 20 atoms, there is an enhanced similarity between the gallium and the aluminium clusters which gets lost as the cluster size increases*.

(b) An Aluminium atom prefers to occupy the internal sites in comparison to the surface sites of the $Ga_{19}Al^+$ cluster.

(c) A systematic increase in the melting temperature of the nanoalloy occurs with increasing aluminium content in the $Ga_{(20-x)}Al_x^+$ cluster series as demonstrated by the first principles based Born-Oppenheimer molecular dynamics (BOMD) calculations on two representative clusters, $Ga_{11}Al_9^+$ and $Ga_3Al_{17}^+$. This suggests that all the clusters, whether pure or mixed i.e. $Ga_{(20-x)}Al_x^+$, in the 20 atom size limit exhibit the *greater-than-bulk melting* behaviour. This also suggests that the size range of the clusters is the first prerequisite for the *greater-than-bulk melting* behaviour, and that composition is secondary (i.e. necessary but not a sufficient condition).

(d) The charge segregation between the internal and surface atoms seems to play an important role in the greater-than-bulk melting behaviour in these clusters. A prominent picture among all the $Ga_{(20-x)}Al_x^+$ clusters is the 'electrostatic caging' of the internal atoms whose disruption is necessary for the phase transition to occur. This picture can be used to, also, view these clusters (or clusters in general) to be components of bulk with additional size specific properties.

These results are a useful step in our efforts to understand the peculiarities in gallium-aluminium nanoalloy clusters. However, few open questions still remain about the occurrence of the greater-than-bulk melting behaviour. Some of them have been mentioned below.

*The first size in Al_n^+ for which a peak in the heat capacity plot is observed is 28. Moreover, the melting temperature corresponding to the peak in the plot is below the bulk melting temperature of aluminium.

(a) Analysing the experimental specific heat curves reported[86] for Al_n^+, as also shown in Fig. 7.1, we do find the data points for the cluster sizes less than 28 atoms to increase at the last observed temperature similar to the case of Al_{20}^+ cluster. Thus, there is a strong chance that these small clusters may melt above the bulk melting temperature of aluminium as well. Moreover, since the first clear peak in specific heat is observed for Al_{28}^+ which is less than the bulk melting temperature of aluminium, there may be a critical size present (between 21 to 27 atoms in Al_n^+) where the element aborts this anomalous, i.e. greater-than-bulk-melting, behaviour and starts showing an agreement with Pawlow's law[36]. The changes in electronic structure below and above this critical size may bring out the exact reason as to why these small size clusters melt above the bulk melting temperature.

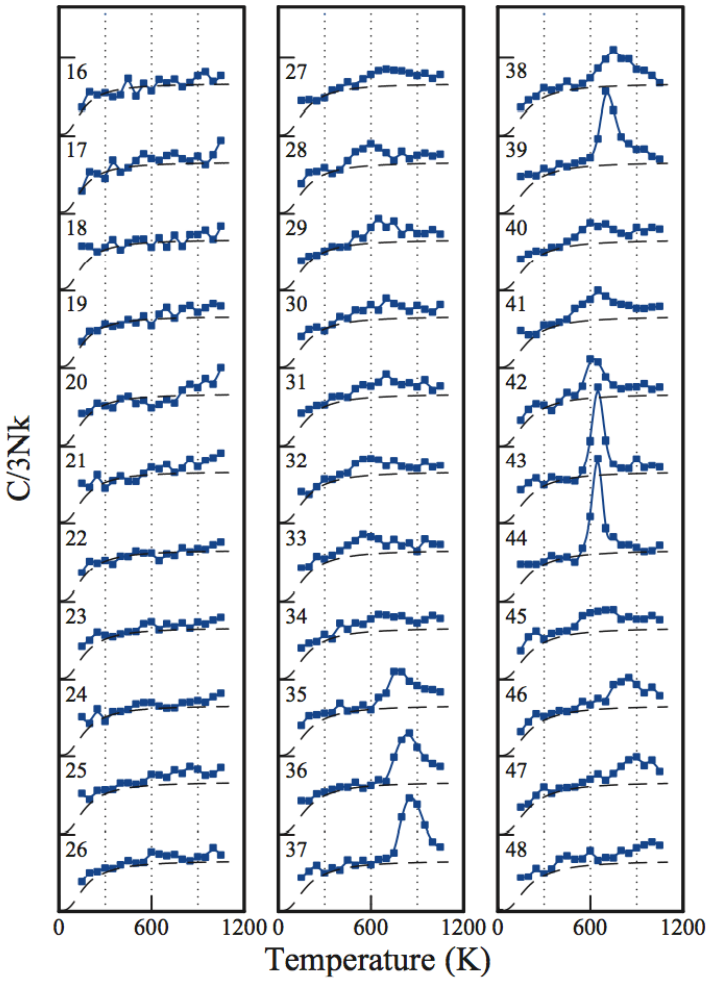

Figure 7.1: Heat capacities measured for different cationic aluminium clusters as a function of temperature. (With permission from Ref.[86])

(b) In the 20 atom size limit, both the pure phases, i.e. gallium and aluminium clusters, demonstrate a *greater-than-bulk melting* behaviour and the melting temperature of aluminium clusters is higher than the corresponding gallium clusters. Thus, it is not a surprise that the mixed nanoalloy clusters of gallium and aluminium clusters ($Ga_{(20-x)}Al_x^+$) also show greater-than-bulk melting behaviour. However, one must not expect a similar behaviour for a size where the gallium clusters show greater-than-bulk melting behaviour and the aluminium clusters melt below the bulk melting temperature of aluminium. Jarrold and co-workers[74] recently found in their experiments that the first size in the gallium clusters which melts below the bulk melting temperature of gallium is 95 atoms. It is curious as to how the melting behaviour of the nanoalloy clusters would be for a size between 28 to 94 atoms (since the experiments on cationic Al clusters[86] show a peak in the specific heat curves only for clusters comprising 28 or more atoms). Pertinent questions to ask would be whether there is a particular composition for a given size where the gallium-aluminium nanoalloy changes its behaviour from showing greater-than-bulk melting behaviour to melting below the corresponding alloy melting temperatures and, how the electronic structure of the nanoalloy cluster changes with the composition in that case.

These questions have to be answered in order to have a complete understanding as to what drives the *greater-than-bulk melting* behaviour in systems comprising few tens of atoms in gallium, tin and also aluminium. This brings us back to Faraday's statement about atoms that indeed, " it is very difficult to form a clear idea of their nature, especially when compounded bodies are under consideration".

Bibliography

[1] Richard P. Feynman. There's plenty of room at the bottom an invitation to enter a new field of physics. *Engineering and Science*, XXIII(5), 1960.

[2] A. W. Castleman and K. H. Bowen. *J. Phys. Chem.*, 100:12911, 1996.

[3] R. L. Johnston. *Atomic and Molecular Clusters*. Taylor and Francis, London, 2002.

[4] D. J. Wales. *Energy Landscape with Applications to Clusters, Biomolecules and Glasses*. Cambridge University, Cambridge, U.K., 2003.

[5] F. Baletto and R. Ferrando. Structural properties of nanoclusters: Energetic, thermodynamic, and kinetic effects. *Rev. Mod. Phys.*, 77:371, 2005.

[6] S. K. Ghosh and T. Pal. *Chem. Rev.*, 107:4797–4862, 2007.

[7] S. Eustis and M. A. El-Sayed. *Chem. Soc. Rev.*, 35:209–217, 2006.

[8] R. Ferrando, J. Jellinek, and R. L. Johnston. *Chem. Rev.*, 108:845, 2008.

[9] D. Alloyeau, C. Mottet, and C. Ricolleau. *Nanoalloys:synthesis, structure and properties*. Engineering Materials, Springer, London, 2012.

[10] R. L. Johnston and J. P. Wilcoxon. *Metal nanoparticles and nanoalloys*, volume 3 of *Frontiers of Nanoscience*. Elsevier, Oxford, U.K., 2012.

[11] F. Calvo. *Nanoalloys: from fundamentals to emergent applications*. Elsevier, Oxford, U.K., 2013.

[12] M. M. Mariscal, O. Oviedo, and E. P. M. Lieva. *Metal Clusters and Nanoalloys*. Nanostructure Science and Technology. Springer, New York, 2013.

[13] K. G. Steenbergen, D. Schebarchov, and N. Gaston. Electronic effects on the melting of small gallium clusters. *J. Chem. Phys.*, 137:144307, 2012.

[14] G. A. Breaux, D. A. Hillman, C. M. Neal, R. C. Benirschke, and M. F. Jarrold. Gallium cluster "magic melters". *J. Am. Chem. Soc.*, 126:8628–8629, 2004.

[15] W. A. de Heer. *Rev. Mod. Phys.*, 65:611, 1993.

[16] W. D. Knight, K. Clemenger, W. A. de Heer, W. A. S. M. Y. Chou, and M. L. Cohen. *Phys. Rev. Lett.*, 52:2141, 1984.

[17] D. G. Kanhere and S. Chacko. *Melting of finite-sized systems*, volume Handbook of Nanophysics: Principles and Methods. CRC Press, Hoboken, 2010.

[18] H. Haberland, editor. *Clusters of atoms and molecules: theory, experiment and clusters of atoms*, volume I and II of *Springer series in chemical physics*. Springer-Verlag, Berlin, 1994.

[19] Nanoalloys: from theory to applications. *Faraday Discuss.*, 138:1–441, 2008.

[20] G. Jaeger. *Arch. Hist. Exact Sci.*, 53:51–81, 1998.

[21] M. W. Zemansky. *Heat and thermodynamics*. McGraw-Hill, fifth edition, 1968.

[22] F. Reif. *Fundamentals of statistical and thermal physics*. McGraw-Hill, 1965.

[23] F. Calvo. Thermodynamics of nanoalloys. *Phys. Chem. Chem. Phys.*, DOI: 10.1039/C5CP00274E.

[24] T. L. Hill. *Thermodynamics of small systems*. Dover, N.Y., 1994.

[25] A. Aguado and M. F. Jarrold. Melting and freezing of metal clusters. *Annu. Rev. Phys. Chem.*, 62:151–172, 2011.

[26] G. M. Wang, E. M. Sevick, E. Mittag, D. J. Searles, and D. J. Evans. *Phys. Rev. Lett.*, 89:050601, 2002.

[27] P. Labastie and R. L. Whetten. Statistical thermodynamics of the cluster solid-liquid transition. *Phys. Rev. Lett.*, 65:1567, 1990.

[28] M. Bixon and J. Jortner. *J. Chem. Phys.*, 91:1631, 1989.

[29] M. Schmidt, R. Kusche, B. von Issendorff, and H. Haberland. *Nature*, 393:238, 1998.

[30] C. Hock, C. Bartels, S. Strassburg, M. Schmidt, H. Haberland, B. von Issendorff, and A. Aguado. *Phys. Rev. Lett.*, 102:043401, 2009.

[31] G. A. Breaux, C. M. Neal, B. Cao, and M. F. Jarrold. *Phys. Rev. Lett.*, 94:173401, 2005.

[32] Z. L. Wang, J. M. Petroski, T. C. Green, and M. A. El-Sayed. *J. Phys. Chem. B*, 102:6145–6151, 1998.

[33] M. Maier-Borst, D. B. Cameron, M. Rokni, and J. H. Parks. *Phys. Rev. A*, 59:R3162–R3165, 1999.

[34] M. Schmidt and H. Haberland. *C. R. Phys.*, 3:327, 2002.

[35] M. Schmidt, R. Kusche, W. Kronmuller, B. von Issendorff, and H. Haberland. *Phys. Rev. Lett.*, 79:99, 1997.

[36] P. Pawlow. *Z. Phys. Chem.*, 65:545, 1909.

[37] Ph. Buffat and J. P. Borel. Size effect on the melting temperature of gold particles. *Phys. Rev. A*, 13:2287–2298, 1976.

[38] S. Zorriasatein, K. Joshi, and D. G. Kanhere. *Phys. Rev. B*, 75:045117, 2007.

[39] A. A. Shvartsburg and M. F. Jarrold. Solid clusters above the bulk melting point. *Phys. Rev. Lett.*, 85:2530, 2000.

[40] S. Darby, T. V. Mortimer-Jones, R. L. Johnston, and C. Roberts. *J. Chem. Phys.*, 116:1536, 2002.

[41] C. Massen, T. V. Mortimer-Jones, and R. L. Johnston. *J. Chem. Soc. Dalton Trans.*, page 4375, 2002.

[42] L. D. Lloyd, R. L. Johnston, S. Salhi, and N. T. Wilson. *J. Mater. Chem.*, 14:1691, 2004.

[43] L. D. Lloyd, R. L. Johnston, and S. Salhi. *J. Comp. Chem.*, 26:1069, 2005.

[44] L. O. Paz-Borbon, R. L. Johnston, G. Barcaro, and A. Fortunelli. *J. Phys. Chem. C*, 111:2936, 2007.

[45] L. O. Paz-Borbon, R. L. Johnston, G. Barcaro, and A. Fortunelli. *J. Chem. Phys.*, 128:134517, 2008.

[46] L. O. Paz-Borbon, A. Gupta, and R. L. Johnston. *J. Mater. Chem.*, 18:4154, 2008.

[47] R. Ferrando, A. Fortunelli, and R. L. Johnston. *Phys. Chem. Chem. Phys.*, 10:640, 2008.

[48] L. Rubinovich, M. I. Haftel, N. Bernstein, and M. Polak. *Phys. Rev. B*, 74:035405, 2006.

[49] J. Jellinek, editor. *Theory of Atomic and Molecular Clusters*. Springer, Berlin, 1999.

[50] E. B. Krissinel and J. Jellinek. *Int. J. Quant. Chem.*, 62:185, 1997.

[51] J. P. Butler. *Proc. Roy. Soc. London A*, 135:348–375, 1932.

[52] K. Sato, B. Bian, and Y. Hirotsu. *J. Appl. Phys.*, 91:8516–8518, 2002.

[53] M. Muller and K. Albe. *Phys. Rev. B*, 72:094203, 2005.

[54] R. V. Chepulskii and W. H. Butler. *Phys. Rev. B*, 72:134205, 2005.

[55] B. Yang, M. Asta, O. N. Mryasov, T. J. Klemmer, and R. W. Chantrell. *Acta Mater.*, 54:4201–4211, 2006.

[56] D. Alloyeau, C. Ricolleau, C. Mottet, T. Oikawa, C. Langlois, Y. LeBouar, N. Braidy, and A. Loiseau. *Nature Mat.*, 8:940–946, 2009.

[57] F. Calvo and C. Mottet. *Phys. Rev. B*, 84:035409, 2011.

[58] P. R. Couchman and W. A. Jesser. Thermodynamic theory of size dependence of melting temperature in metals. *Nature*, 269:481–483, 1977.

[59] B. Cao, A. K. Starace, C. M. Neal, M. F. Jarrold, S. Nunez, J. M. Lopez, and A. Aguado. *J. Chem. Phys.*, 129:124709, 2008.

[60] Colleen M. Neal, Anne K. Starace, and Martin F. Jarrold. Melting of alloy clusters: Effects of aluminum doping on gallium cluster melting. *J. Phys. Chem. A*, 111:8056–8061, 2007.

[61] C. Mottet, G. Rossi, F. Baletto, and R. Ferrando. *Phys. Rev. Lett.*, 95:035501, 2005.

[62] P. Chandrachud, K. Joshi, and D. G. Kanhere. *Phys. Rev. B*, 76:235423, 2007.

[63] L. Fiermans, R. D. Gryse, G. D. Doncker, P. A. Jacobs, and A. J. Martens. *J. Catal.*, 193:108–114, 2000.

[64] U. Kolb, S. A. Quaiser, M. Winter, and M. T. Reetz. *Chem. Mater.*, 8:1889–1894, 1996.

[65] F. Calvo. *Faraday Discuss.*, 138:75–88, 2008.

[66] F. Calvo, E. Cottancin, and M. Broyer. *Phys. Rev. B*, 77:121406(R), 2008.

[67] A. Aguado and J. M. Lopez. *Phys. Rev. B*, 72:205420, 2005.

[68] K. Albe, K. Nordlund, J. Nord, and A. Kuronen. *Phys. Rev. B*, 66:035205, 2002.

[69] A. Schnepf and H. Schnockel. *Angew. Chem. Int. Ed.*, 41:3532, 2002.

[70] X. G. Gong, G. L. Chiarotti, M. Parrinello, and E. Tosatti. *Phys. Rev. B*, 43:14277, 1991.

[71] E. Voloshina, K. Rosciszewski, and B. Paulus. *Phys. Rev. B*, 79:045113, 2009.

[72] G. A. Breaux, R. C. Benirschke, T. Sugai, B. S. Kinnear, and M. F. Jarrold. Hot and solid gallium clusters: too small to melt. *Phys. Rev. Lett.*, 91:215508, 2003.

[73] G. A. Breaux, B. Cao, and M. F. Jarrold. Second-order phase transition in amorphous gallium clusters. *J. Phys. Chem. B. Lett.*, 109:16575–16578, 2005.

[74] K. L. Pyfer, J. O. Kafader, A. Yalamanchali, and M. F. Jarrold. Melting of size-selected gallium clusters with 60183 atoms. *J. Phys. Chem. A*, 118:4900–4906, 2014.

[75] S. Krishnamurty, S. Chacko, and D. G. Kanhere. *Phys. Rev. B*, 73:045406, 2006.

[76] S. Chacko, K. Joshi, D. G. Kanhere, and S. A. Blundell. Why do gallium clusters have a higher melting point than the bulk? *Phys. Rev. Lett.*, 92(13):135506, 2004.

[77] S. Nunez, J. Lopez, and A. Aguado. *Nanoscale*, 4:6481, 2012.

[78] A. Cottrell. *Introduction to the modern theory of metals*. Institute of metals, London, 1988.

[79] J. Sprosser-Prou, A. vom Felde, and J. Fink. *Phys. Rev. B*, 40:5799, 1989.

[80] P. N. H. Nakashima, A. E. Smith, J. Etheridge, and B. C. Muddle. Supporting information. *Science*, 331:1583, 2011.

[81] S. Ogata, J. Li, and S. Yip. *Science*, 298:807, 2002.

[82] N. Kioussis, M. Herbranson, E. Collins, and M. E. Eberhart. *Phys. Rev. Lett.*, 88:125501, 2002.

[83] P. D. Desai. *Int. J. Thermophys.*, 8:621, 1987.

[84] G. K. Straub, J. B. Aidun, J. M. Wills, C. R. Sanchez-Castro, and D. C. Wallace. *Phys. Rev. B*, 50:5055, 1994.

[85] P. Puri and V. Yang. *J. Phys. Chem. C*, 111:11776–11783, 2007.

[86] C. M. Neal, A. K. Starace, and M. F. Jarrold. Melting transitions in aluminum clusters: The role of partially melted intermediates. *Phys. Rev. B*, 76:054113, 2007.

[87] M. F. Jarrold, B. Cao, A. K. Starace, C. M. Neal, and O. H. Judd. *J. Chem. Phys.*, 129:014503, 2008.

[88] B. Cao, A. K. Starace, O. H. Judd, I. Bhattacharyya, and M. F. Jarrold. Metal clusters with hidden ground states: Melting and structural transitions in al115+, al116+, and al117+. *J. Chem. Phys.*, 131:124305, 2009.

[89] J. Pohl, C. Stahl, and K. Albe. *Beilstein J. Nanotech.*, 3:1–11, 2012.

[90] H. B. Liu, U. Pal, and J. A. Asciencio. *J. Phys. Chem. C*, 112:19173–19177, 2008.

[91] A. Shirinyan, M. Wautelet, and Y. Belogorodsky. *J. Phys.: Condens. Matter*, 18:2537, 2006.

[92] J. Sopousek, J. Vrestal, J. Pinkas, P. Broz, J. Bursik, A. Styskalik, D. Skoda, O. Zobac, and J. Lee. *CALPHAD*, 45:33–39, 2014.

[93] G. Guisbiers, S. Mejia-Rosales, S. Khanal, F. Ruiz-Zepeda, R. L. Whetten, and M. Jose-Yacaman. *Nano Lett.*, 14:6718–6726, 2014.

[94] D. H. Kim, H. Y. Kim, J. H. Ryu, and H. M. Lee. *Phys. Chem. Chem. Phys.*, 11:5079, 2009.

[95] J. L. Murray. *Bulletin of Alloy Phase Diagrams*, 4:183, 1983.

[96] J. Shealy and J. Woodall. *App. Phys. Lett.*, 41(88), 1982.

[97] F. Shimojo, S. Ohmura, R. K. Kalia, A. Nakano, and P. Vashishta. *Phys. Rev. Lett.*, 104:126102, 2010.

[98] P. J. Roach, W. H. Woodward, A. W. Castleman Jr., A. C. Reber, and S. N. Khanna. *Science*, 323:492–495, 2009.

[99] S. Ohmura, F. Shimojo, R. K. Kalia, M. Kunaseth, A. Nakano, and P. Vashishta. *J. Chem. Phys.*, 134:244702, 2011.

[100] R. M. Dreizler and E. K. U. Gross. *Density Functional Theory.* Springer, Berlin, 1990.

[101] R. G. Parr and W. Yang. *Density-Functional Theory of Atoms and Molecules.* Oxford University Press, Oxford, 1989.

[102] W. Koch and M. C. Holthausen. *A Chemist's Guide to Density Functional Theory.* John Wiley and Sons, New York, 2001.

[103] R. O. Jones and O. Gunnarsson. *Rev. Mod. Phys.*, 61:689, 1989.

[104] J. M. Seminario, editor. *Recent Developments and Applications of Modern DFT.* Elsevier, Amsterdam, 1996.

[105] R. F. Nalewajski (Ed.), editor. *Density Functional Theory I -IV*, volume Topics in Current Chemistry Vols. 180-183. Springer, 1996.

[106] N. H. March. *Electron Density Theory of Atoms and Molecules.* Academic Pressdemic Press, London, 1992.

[107] B. B. Laird, R. B. Ross, and T. Ziegler (Eds.), editors. *Chemical Applications of Density Functional Theory.* American Chemical Society, 1996.

[108] D. P. Chong (Ed.). *Recent Advances in Density Functional Methods.* World Scientific, Singapore, 1995.

[109] M. Born and K. Huang. *Dynamical theory of crystal lattice.* Oxford Univ. Press, 1954.

[110] P. Hohenberg and W. Kohn. *Phys. Rev.*, 136:B864, 1964.

[111] W. Kohn and L. J. Sham. *Phys. Rev.*, 140:A1133, 1965.

[112] D. M. Ceperley and B. J. Alder. *Phys. Rev. Lett.*, 45:566, 1980.

[113] Y. Wang and J. P. Perdew. *Phys. Rev. B*, 44:13298, 1991.

[114] J. P. Perdew, K. Burke, and M. Ernzerhof. *Phys. Rev. Lett.*, 78:1396, 1997.

[115] Y. Zhang and W. Yang. *Phys. Rev. Lett.*, 80:890, 1998.

[116] J. Perdew, S. Kurth, A. Zupan, and P. Blaha. *Phys. Rev. Lett.*, 82:2544, 1999.

[117] A. D. Becke. *J. Chem. Phys.*, 98:5648, 1993.

[118] P. J. Stephens, F. J. Devlin, C. F. Chabalowski, and M. J. Frisch. *J. Phys. Chem.*, 98:11623, 1994.

[119] M. Dion, H. Rydberg, E. Schroder, D. C. Langreth, and B. I. Lundqvist. *Phys. Rev. Lett.*, 92:246401, 2004.

[120] M. C. Payne, M. P. Teter, D. C. Allan, T. A. Arias, and J. D. Joannopoulos. *Rev. Mod. Phys.*, 64:1045, 1992.

[121] N. W. Ashcroft and N. D. Mermin. *Solid State Physics*. Cengage Learning, 1976.

[122] S. Yip. *Handbook of materials modelling*. Springer, 2005.

[123] W. A. Harrison. *Pseudopotentials in the theory of metals*. Benjamin Inc. Publishers, 1966.

[124] J. C. Phillips. *Phys. Rev.*, 112:685, 1958.

[125] J. C. Phillips and L. Kleinman. *Phys. Rev.*, 116:287, 1959.

[126] V. Heine. *The Pseudopotential Concept, vol. 24 of Solid State Physics*. Academic Press, New York, 1970.

[127] J. Ihm. *Rep. Prog. Phys.*, 51:105, 1988.

[128] W. E. Pickett. *Comp. Phys. Rep.*, 9:115, 1989.

[129] A. D. Corso, A. Pasquarello, A. Baldereschi, and R. Car. *Phys. Rev. B*, 53:1180, 1996.

[130] A. D. Becke. *Phys. Rev. A*, 38:3098, 1988.

[131] J. P. Perdew. *Phys. Rev. B*, 33:8822, 1986.

[132] D. Frenkel and B. Smit. *Understanding Molecular Simulation: From Algorithms to Applications*. Academic Press, San Diego, CA, 1996.

[133] G. Kresse and J. Hafner. *Phys. Rev. B*, 47:558, 1993.

[134] G. Kresse and J. Hafner. *Phys. Rev. B*, 49:14251, 1994.

[135] G. Kresse and J. Furthmüller. *Comput. Mater. Sci.*, 6:15, 1996.

[136] G. Kresse and J. Furthmüller. *Phys. Rev. B*, 54:11169, 1996.

[137] H. Hellman. *Einfuhrung in die Quantenchemie*. Deuticke, Wien, 1937.

[138] R. Feynman. *Phys. Rev.*, 56:340, 1939.

[139] A description of the Störmer-Verlet method can be found at http://www.fisica.uniud.it/ ercolessi/md/md/node21.html.

[140] L. Verlet. *Phys. Rev.*, 165:201, 1968.

[141] W. C. Swope, H. C. Andersen, P. H. Berens, and K. R. Wilson. *J. Chem. Phys.*, 76:637, 1982.

[142] M. P. Allen and D. J. Tildesley. *Computer Simulation of Liquids*. Clarendon Press, Oxford, U.K., 1987.

[143] D. C. Rapaport. *The Art of Molecular Dynamics Simulation*. Cambridge University Press, Cambridge, U.K., 1998.

[144] K. G. Steenbergen. *Modelling the Melting of Gallium Clusters: A Path to Understanding Molecular Solids*. PhD thesis, Victoria University of Wellington, Wellington, New Zealand, 2013.

[145] J. Tersoff. *Phys. Rev. B*, 39:5566, 1989.

[146] http://lammps.sandia.gov.

[147] S. Plimpton. *J. Comp. Phys.*, 117:1, 1995.

[148] F. Calvo, J. P. Neirotti, D. L. Freeman, and J. D. Doll. *J. Chem. Phys.*, 112:10350, 2000.

[149] J. P. Neirotti, F. Calvo, D. L. Freeman, and J. D. Doll. *J. Chem. Phys.*, 112(23):10340, 2000.

[150] P. Blöchl. *Phys. Rev. B*, 50:17953, 1994.

[151] G. Kresse and D. Joubert. *Phys. Rev. B*, 59:1758, 1999.

[152] J. Perdew, J. Chevary, S. Vosko, K. Jackson, M. Pederson, D. Singh, and C. Fiolhais. *Phys. Rev. B*, 46:6671, 1992.

[153] J. Perdew, J. Chevary, S. Vosko, K. Jackson, M. Pederson, D. Singh, and C. Fiolhais. *Phys. Rev. B*, 48:4978, 1993.

[154] J. Jellinek and A. Goldberg. *J. Chem. Phys.*, 113:2570, 2000.

[155] C. Bichara, J. Gaspard, and J. Mathieu. *Phys. Lett. A*, 119:462, 1987.

[156] A. Ferrenberg and R. Swendsen. *Phys. Rev. Lett.*, 61:2635, 1988.

[157] F. Calvo and P. Labastie. *Chem. Phys. Lett.*, 247:395, 1995.

[158] P. Blaise and S. Blundell. *Phys. Rev. B*, 63:235409, 2001.

[159] Y. Zhou, M. Karplus, K. D. Ball, and R. S. Berry. *J. Chem. Phys.*, 116:2323, 2002.

[160] K. G. Steenbergen and N. Gaston. *Phys. Chem. Chem. Phys.*, 15:15325–15332, 2013.

[161] F. Calvo and F. Spiegelmann. *Phys. Rev. Lett.*, 82:2270, 1999.

[162] W. Curtin and N. Ashcroft. *Phys. Rev. Lett.*, 56:2775, 1986.

[163] T. Egami and S. J. L. Billinge. *Underneath the Bragg Peaks. Structural analysis of complex material*. Elsevier, Amsterdam, 2003.

[164] Leonid V. Zhigilei. http://people.virginia.edu/ lz2n/mse627/notes/correlations.pdf.

[165] R. S. Berry. *The Chemical Physics of Atomic and Molecular Clusters*, chapter Structure and dynamics of clusters: An introduction. Elsevier: Amsterdam, 1990.

[166] Aleksandra Radenovic. Brownian motion and single particle tracking, http://lben.epfl.ch/files/content/sites/lben/files/users/179705/brownian

[167] T. W. Yen, P. J. Hsu, and S. K. Lai. *e-J. Surf. Sci. Nanotechnology*, 7:149, 2009.

[168] R. Bader. *Atoms in Molecules: a quantum theory, International series of monographs on chemistry*, volume 22. Clarendon Press, Oxford, UK, 1990.

[169] A. Arnaldsen, W. Tang, and G. Henkelman. http://theory.cm.utexas.edu/henkelman/code/bader/.

[170] A. D. Becke and K. E. A. Edgecombe. A simple measure of electron localization in atomic and molecular systems. *J. Chem. Phys.*, 92:5397, 1990.

[171] B. Silvi and A. Savin. *Nature*, 371:683, 1994.

[172] P. Fuentealba, E. Chamorro, and J. C. Santos. *Understanding and using the electron localization function*, volume 19 Theoretical and Computational Chemistry: Theoretical aspects of chemical reactivity. Elsevier B. V., 2007.

[173] M. J. Frisch, G. W. Trucks, and H. B. Schlegel et al. Gaussian 09, revision b.01. pages Gaussian, Inc.. Wallingford, CT, 2009.

[174] N. Gaston and A. J. Parker. *Chem. Phys. Lett.*, 501:375–378, 2011.

[175] K. Joshi, S. Krishnamurty, and D. G. Kanhere. *Phys. Rev. Lett.*, 96:135703, 2006.

[176] J. P. Perdew. *Electronic structure of solids*, volume 11. Akademie Verlag, Berlin, 1991.

[177] J. P. Perdew, K. Burke, and Y. Wang. Generalized gradient approximation for the exchange-correlation hole of a many-electron system. *Phys. Rev. B*, 54:16533, 1996.

[178] K. Burke, J. P. Perdew, and Y. Wang. *Electronic Density Functional Theory: Recent Progress and New Directions*. Plenum, 1998.

[179] D. E. Woon and T. H. Dunning Jr. *J. Chem. Phys.*, 98:1358–71, 1993.

[180] S. Noury, X. Krokidis, F. Fuster, and B. Silvi. *TopMoD package*, page Universite Pierre et Marie Curie, 1997.

[181] K. Momma and F. Izumi. *J. Appl. Cryst.*, 44:1272–1276, 2011.

[182] W. Humphrey, A. Dalke, and K. Schulten. *J. Molec. Graphics*, 14:33–38, 1996.

[183] X. Tan and P. J. Dagdigian. *J. Phys. Chem. A*, 107:2642, 2003.

[184] R. Tonner and N. Gaston. *Phys. Chem. Chem. Phys.*, 16:24224, 2014.

[185] N. Drebov, F. Weigend, and R. Ahlrichs. *J. Chem. Phys.*, 123:144312, 2005.

[186] S. Krishnamurty, S. Chacko, D. G. Kanhere, G. A. Breaux, C. M. Neal, and M. F. Jarrold. *Phys. Rev. B*, 73:045406, 2006.

[187] U. Ojha, K. G. Steenbergen, and N. Gaston. How a single aluminum atom makes a difference to gallium: First-principles simulations of bimetallic cluster melting. *J. Chem. Phys.*, 139:094309, 2013.

[188] P. J. Linstrom and W. G. Mallard, editors. *"Aluminium - Phase change data"*. NIST Chemistry WebBook, NIST Standard Reference Database Number 69, National Institute of Standards and Technology, Gaithersburg MD, 20899, http://webbook.nist.gov, (retrieved June 20, 2014).

[189] K. G. Steenbergen and N. Gaston. Geometrically induced melting variation in gallium clusters from first principles. *Phys. Rev. B*, 88:161402(R), 2013.

[190] W. Zhang, F-S Zhang, and Z-Y Zhu. Melting transition of small aluminium clusters al11-20. *Chin. Phys. Lett.*, 24(7):1915, 2007.

[191] F-C Chuang, C. Z. Wang, and K. H. Ho. Structure of neutral aluminum clusters aln (2¡=n¡=23): genetic algorithm tight-binding calculations. *Phys. Rev. B*, 73:125431, 2006.

[192] F. Kargl, H. Weis, T. Unruh, and A. Meyer. Self diffusion in liquid aluminium. *J. Phys: Conf. Series*, 340:012077, 2012.

[193] J. Petit and N. H. Nachtrieb. Self-diffusion in liquid gallium. *J. Chem. Phys.*, 24:1027, 1956.

[194] C. M. Neal, A. K. Starace, and M. F. Jarrold. *J. Phys. Chem. A*, 111:8056, 2007.

[195] C-Y Cha, G. Gantefor, and W. Eberhardt. The development of the 3p and 4p valence band of small aluminum and gallium clusters. *J. Chem. Phys.*, 100(2):995, 1994.

[196] C. M. Neal, A. K. Starace, and M. F. Jarrold. *J. Phys. Chem. A*, 111:8056, 2007.

[197] F. Shimojo, S. Ohmura, R. K. Kalia, A. Nakano, and P. Vashishta. Molecular dynamics simulations of rapid hydrogen production from water using aluminum clusters as catalyzers. *Phys. Rev. Lett.*, 104:126102, 2010.

[198] L. H. Liang, D. Liu, and Q. Jiang. *Nanotechnology*, 14:438, 2003.

[199] M. Wautelet, J. P. Dauchot, and M. Hecq. *Mater. Sci. Eng. C*, 23:187, 2003.

[200] J. Park and J. Lee. *Calphad*, 32:135, 2008.

[201] Ph. Buffat and J.-P. Borel. *Phys. Rev. A*, 13:2287, 1976.

[202] L. J. Lewis, P. Jensen, and J. L. Barrat. *Phys. Rev. B*, 56:2248, 1997.

[203] C. B. Barber, D. P. Dobkin, and H. Huhdanpaa. The quickhull algorithm for convex hulls. *ACM Trans. on Mathematical Software*, 22:469–483, 1996.

[204] M. Schmidt, J. Donges, Th. Hippler, and H. Haberland. *Phys. Rev. Lett.*, 90:103401, 2003.